Technische Universität München

Lehrstuhl für Angewandte Mechanik

Design and Control of Compact High Dynamic Camera Orientation Systems

Thomas Villgrattner

Vollständiger Abdruck der von der Fakultät für Maschinenwesen der Technischen Universität München zur Erlangung des akademischen Grades eines

Doktor-Ingenieurs

genehmigten Dissertation.

Vorsitzender:

Univ.–Prof. Dr. phil. Klaus Bengler

Prüfer der Dissertation:

1. Univ.–Prof. Dr.–Ing. habil Heinz Ulbrich
2. Univ.–Prof. Dr.–Ing. Frank Schiller

Die Dissertation wurde am 06.07.2010 bei der Technischen Universität München eingereicht und durch die Fakultät für Maschinenwesen am 21.10.2010 angenommen.

Acknowledgments

This thesis summarizes three and a half years of the research I carried out at the Institute of Applied Mechanics (AM) of the Technische Universität München (TUM). The work was supported in part by the German Research Foundation (DFG) excellence initiative research cluster "Cognition for Technical Systems – CoTeSys".

First of all, my gratitude goes to my advisor Univ.–Prof. Dr.–Ing. Dr.–Ing. habil. Heinz Ulbrich, who gave me the opportunity to conduct research in a pleasant and international environment. He always supported me with his immense experience and invaluable advice and allowed me enough freedom for my own creativity.

I would like to pass on my sincere gratitude to Univ.–Prof. Dr.–Ing. Frank Schiller as well as to Univ.–Prof. Dr. phil. Klaus Bengler for their interest in my work and for serving as second advisor and chairman of the examination board respectively.

Special thanks also goes to Dr.–Ing. Thomas Thümmel for the fruitful discussions and his support in administrative matters as well as to the institute's secretaries, Ms. Rita Schneider and Ms. Manuela Müller–Philipp.

Further, I would like to thank all my colleagues at the institute for the invaluable debates and immense assistance they provided me within all the phases of my work. Special thanks go to Philipp Wagner, Daniel Wiedemann, Markus Schneider, Markus Schwienbacher, Valerio Favot, Daniela Förg, Thomas Buschmann, Sebastian Lohmeier, and Roland Zander. For extending my horizon to new research fields I would moreover like to expand my gratitude to all my colleagues from the CoTeSys cluster. Special mention is due to my project partners Dr. hum. biol. Erich Schneider, Stefan Kohlbecher, Klaus Bartl, Stanislavs Bardins, Johannes Vockeroth, and Prof. Dr. med. Dr. h.c. Thomas Brandt, FRCP from the Chair for Clinical Neurosciences, Ludwigs–Maximilian–University of Munich, Dr.–Ing. Frank Wallhoff, Tony Poitschke, and Prof. Dr.–Ing. habil. Gerhard Rigoll from the Institute for Human–Machine Communication, TUM as well as Prof. Dr. Gordon Cheng, Brennand Pierce, Andreas Holzbach, and Ewald Lutscher from the Institute for Cognitive Systems, TUM. Furthermore, I would like to thank Dr. rer. nat. Felix von Hundelshausen and Gerhard Rohe from the Institute of Autonomous Systems Technology, Universität der Bundeswehr München, for the profitable "active vision" talks.

Without the inestimable technical knowledge and the active support of our mechanical and electrical workshop staff the hardware development would not have been possible. Special thanks goes to Wilhelm Miller, Georg Mayr, Simon Gerer, Walter Wöß, Philip Schneider, and Tobias Schmid for dealing so excellently with all my "remarkable" wishes.

I am grateful to all students who contributed to the success of this thesis. Particularly I would like to thank Tomas Szabo and Philipp Andersch for the implementation of different control architectures on the camera orientation systems, Alejandro Cárdenas Miranda for his manipulator design considerations, and Sergio Delgado Londono for his observations to solve the direct kinematic solution. For their assistance in different hard– and software issues I thank my working students Robert Wesenjak, Michael Überbacher, and Hans von Rottkay.

Finally, I would like to thank also my family and my girlfriend Angelika who always stood behind my decisions and offered gentle counsel in critical phases. Without their understanding and love this thesis would never have been possible.

Munich, July 2010 *Thomas Villgrattner*

to Angelika

Abstract

Images acquired from a first person's perspective can be used to estimate the user's intention. Required high quality images can be retrieved when continuously aligning a camera with the human gaze. The human vestibulo–ocular and optokinetic reflexes automatically stabilize the human eye, even under dynamic conditions. Such an approach, however, requires camera orientation systems which are able to reproduce the high dynamic movements of the human oculomotor system, while at the same time providing a small and lightweight design. In this thesis, parallel kinematic manipulators, driven by ultrasonic piezo–actuators, with two and three rotational degrees–of–freedom are developed. Besides kinematic, also dynamic models are calculated and used to optimize the workspace/package ratio and to estimate force and velocity output capabilities. A series of control strategies are depicted and investigated. Prototypes of the designed camera orientation systems are presented and their integration into different application scenarios is demonstrated.

Kurzfassung

Aus einer Ich-Perspektive aufgenommene Bilder können dazu herangezogen werden Absichten einer Person zu schätzen. Die dazu notwendigen qualitativ hochwertigen Bilder können durch kontinuierliches Ausrichten einer Kamera an der Blickrichtung des Benutzers erzeugt werden. Die menschlichen vestibulären- und optokinetischen Reflexe stabilisieren nämlich das menschliche Auge auch im Falle hochdynamischer Bewegungen. Solch ein Ansatz verlangt jedoch Kameraorientierungssysteme, die in der Lage sind die hochdynamischen Bewegungen des menschlichen Auges bei gleichzeitig kompakter und leichter Bauweise abzubilden. In der vorliegenden Dissertationsschrift werden parallel kinematische Manipulatoren, angetrieben durch Ultraschall–Piezomotoren, mit zwei und drei Freiheitsgraden entwickelt. Neben kinematischen Modellen werden dynamische Modelle hergeleitet, die zur Optimierung des Arbeits–/Bauraumverhältnisses und zur Schätzung der Kraft– und Geschwindigkeitsausgabekapazitäten herangezogen werden. Eine Reihe von Regelungsarchitekturen wird vorgestellt und untersucht. Prototypen der entwickelten Kameraorientierungssysteme werden eingeführt und deren Integration in verschiedene Anwendungsszenarien demonstriert.

Contents

Notations

Conventions

In this thesis scalars are denoted by lower and upper case letters in italic type face (x, X). Vectors are labeled by bold lower case letters ($\boldsymbol{x}$). The vector $\boldsymbol{x}$ is composed of elements $\boldsymbol{x}_i$. Matrices are denoted by bold upper case letters ($\boldsymbol{X}$) and the matrix $\boldsymbol{X}$ is composed of elements $\boldsymbol{X}_{ij}$ (i–th row and j–th column). Desired set values are marked with an asterisk superscript (x^*) and estimated values are described with a hat ($\hat{x}$). The upper dot denotes time derivative ($\dot{x}$). Coordinate systems related to the body x are depicted with $\boldsymbol{S}_x$. A vector $\boldsymbol{x}$ represented in the coordinate system $\boldsymbol{S}_y$ is depicted with ${}_y\boldsymbol{x}$. Homogeneous rotation matrices, which are used to transform vectors from $\boldsymbol{S}_x$ to $\boldsymbol{S}_y$ are denoted with ${}^y\boldsymbol{R}_x$.

Symbols in alphabetical order

$\boldsymbol{A}$	control state matrix
α	camera orientation around the pan axis
$\boldsymbol{B}$	control input matrix
β	camera orientation around the tilt axis
c	stiffness coefficient
$\boldsymbol{C}$	control output matrix
γ	camera orientation around the roll axis
d	damping coefficient
$\boldsymbol{D}$	control feed through matrix
δ	amount of differentiations
e_{calc}	calculation error
e_q	quantization error
F	force
$\boldsymbol{F}$	control pre–filter matrix
$\boldsymbol{g}$	inverse kinematics
θ_i	position of the linear actuators/prismatic joints (i = 1,2,3;)
θ_{max}	maximum deflection of the prismatic joints
$\boldsymbol{I}$	moment of inertia
$\boldsymbol{J}$	Jacobian
l	push rod length
$\boldsymbol{L}$	observer gain
m	mass

M	torque
μ	friction coefficient
ξ	elevation angle
$O_{GJ_{max}}$	maximum deflection of the gimbal joints
$O_{M_{max}}$	maximum deflection of the main spherical joints
$O_{PR_{max}}$	maximum deflection of the push rod spherical joints
$\boldsymbol{q}$	joint space coordinates
$\boldsymbol{Q}_{nc}$	non conservative forces
r_1	minimum distance between push rod end points and z–axis on actuator side
r_2	minimum distance between push rod end points and z–axis on camera side
$\boldsymbol{R}$	state space control matrix
$\boldsymbol{S}_i$	coordinate system with origin in point i
t	time
t_{calc}	calculation time
T	kinetic energy
$\boldsymbol{u}$	input vector
U	voltage
v	actuator velocities
$\boldsymbol{w}$	workspace coordinates
x, y, z	coordinates
$\boldsymbol{x}$	state vector
V	potential energy
χ	deflection of the push rod spherical joints around the pan axis
ψ	deflection of the push rod spherical joints around the tilt axis
φ	deflection of the push rod spherical joints around the roll axis
$\boldsymbol{y}$	output vector
$\boldsymbol{z}$	disturbance vector

Abbreviations

CAD	computer–aided–design
CoG	center–of–gravity
DoF	degree–of–freedom
DIS	digital image stabilization
IMU	inertial measurement unit
IR	infrared
LQR	linear quadratic regulator
MBSim	multi body simulation tool
$\mathcal{NL}^{-1}$	inverse nonlinearity
OKR	optokinetic reflex
PID	proportional integral differential
PWM	pulse with modulated
VOG	video oculography
VOR	vestibulo–ocular reflex
WS	workspace

1. Introduction

While in the past robots were limited to industrial applications only, nowadays robots also enter domestic environments and assist people in performing everyday activities. Robots are e.g. employed in household applications, training scenarios, elderly care, autonomous transportation systems, and interactive industry applications sharing their working space with human beings. Pre–programmed robots, as employed in industrial settings, are doomed to failure as they cannot cope with highly dynamic and unknown environmental conditions. In contrast, cognitive technical systems, as introduced e.g. in [10] and [110] can overcome these limitations by estimating human intentions, by deciding on their own actions, and by adapting and executing them in a reliable and safe manner.

Reliable estimation of human intentions is a crucial element of a cognitive technical system. An often adopted approach for human intention estimation evaluates the human gaze direction, which highly correlates with spatial and social attention. As illustrated in [57] and [62] the human gaze direction can be used to deduce the user's intention, her/his grade of experience as well as her/his physiological state.

Different eye–tracking principles are proposed in the literature, see e.g. [29] and [32] for an overview. To allow humans to move freely in space, portable head–mounted systems are often favored, which provide a video stream of the human field of view including the actual viewing direction. The latter is typically estimated by a video oculography (VOG) device. Often both, the scene camera (which acquires the surroundings) and the eye–tracker, are directly fixed on the user's head. This leads to simple and compact devices, which however, provide only a poor image quality and resolution when no supplementary stabilization techniques are employed.

To avoid these drawbacks, Schneider et al. introduced a so called head–mounted gaze–driven camera system [93], which is composed of two major parts: a VOG device and a camera orientation device. This mobile system continuously aligns a camera with the user's line of sight. If the camera orientation device is able to reproduce human eye movements with small latency, stabilized images are acquired without any supplementary post–processing.

1.1. Problem Definitions and Challenges

A head–mounted gaze–driven camera system principally consists of two parts: an eye–tracker and a camera orientation device. While different eye-tracking systems

are available on the market, no camera orientation system is known which is suitable for the above mentioned application.

A technical system which should reproduce the human eye movements must cope with the capabilities of the human oculomotor system in terms of accessible workspace, accuracy, velocity, and acceleration. In addition it must deal with the wide spectrum of human eye movements, which range from nearly statically (fixation), over slow phases (smooth pursuit), to high dynamic changes (saccades). Furthermore, "natural" camera stabilization is required, which calls for small latencies between eye and camera movements. Since the entire system is intended to be mounted on a human head, a lightweight and compact design is needed to minimize irritation of the user.

This thesis aims to cope with the posed requirements by developing and controlling new compact and high–dynamic camera orientation systems. Approaches based on parallel kinematic manipulators are investigated. Offline optimization of the device configuration and numerical simulations of kinematic and dynamic parameters are employed. Finally, alignment of the camera with the human line of sight is achieved by implementing appropriate control algorithms.

The camera orientation devices are also integrated into several complex robotic systems. Although the main design purpose is a head–mounted gaze–driven camera system, the developed systems can be applied in any scenario that requires cameras to be oriented with the same dynamic properties of the human oculomotor system and where low weight and small overall dimensions are required. Thus, an artificial eye for humanoid robots, the usage in an eye–related Wizard–of–Oz scenario and a camera orientation device for active remote eye–trackers are discussed as additional applications.

1.2. Main Contributions and Outline of the Dissertation

The main goal of this thesis is the design and control of compact high–dynamic camera orientation systems. The developed devices are intended to cope with the capabilities of the human oculomotor system in terms of reachable workspace, velocity, and accelerations while at the same time guaranteeing a compact overall size as well as a lightweight design. Two versions of camera orientation systems, implementing two or all three orientations of the human eye are realized.

The present work is organized in seven chapters. In Chapter 2 the capabilities of a human eye are described and subsequently the requirements on the technical systems are formulated. Furthermore, the state of the art and different design concepts are introduced. Chapter 3 and Chapter 4 deal with the design and optimization of the camera orientation systems respectively. In Chapter 5 different control approaches are discussed. The integration of the developed camera orientation systems into different application scenarios is described in Chapter 6. Finally, Chapter 7 concludes

the work by summarizing the most important results and by highlighting directions of future research.

Main reflexes and movements of the human oculomotor system are introduced in Chapter 2 to establish requirements on the technical systems. The state–of–the–art of active camera orientation systems is reviewed and an overview of digital image stabilization is given. Since, to the author's knowledge, none of the current systems are able to meet the formulated requirements, possible solutions are introduced and compared with each other.

Chapter 3 deals with the development and optimization of two camera orientation systems with two degrees–of–freedom (DoFs). Both implement the same parallel kinematics, while the kinematic parameters are varied slightly to adapt the systems to different mounting positions. To allow for an appropriate actuator and sensors selection, requirements on the dynamics are determined using a simple point mass model. In the first step, different actuator and sensor concepts are introduced and compared. To determine and optimize the workspace, the inverse and the direct kinematic solution of the camera orientation devices are calculated. Dimensions and masses of the single mechanical components are optimized and resulting parameters are used to parameterize kinematic and dynamic simulation models. The simulation results clearly reveal that the developed systems are able to replicate human eye movements.

To reproduce all three possible human eye rotations, a camera orientation device with three DoF is introduced in Chapter 4. Based on the experience gained with the two DoF camera orientation systems, requirements on the new device are defined. Besides a third rotational DoF, a higher resolution of the measurement system and a more compact design are desired, while requirements on the workspace are reduced. This system is also based on a parallel kinematics and a similar approach for the development as for the devices with two DoF was used. Again, requirements for actuators and sensors are estimated first using a simple point mass model. Then, different concepts are introduced and compared with each other. The manipulators' inverse and direct kinematic solution are acertained, allowing the workspace determination. Using an implicit filtering algorithm (IFFCO), parameter variation studies are conducted to optimize the workspace/package dimension ratio. Once the masses and the dimensions of the single mechanical components are determined, these parameters are used in the respective kinematic and dynamic simulation models. The simulations confirmed that the investigated system can cope with the high dynamic orientation changes of the human oculomotor system. Finally, the setup of the camera orientation system and the specifications are introduced.

The selected actuator system is investigated in Chapter 5. Possibilities of dealing with the dead zone are presented. Subsequently, different linear and nonlinear control strategies used to align the camera orientation systems are discussed. The introduced approaches are sub–divided into two categories: joint space and workspace controllers. To implement a Falb and Wolovich decoupling controller, the equations of motion for a simplified mechanic model are derived and validated with

a dynamic simulation model which accounts for the entire manipulator. Experiments evaluating step response and tracking behavior are performed to compare the different control approaches. For the most promising approach additional measurements, including also the entire head–mounted gaze–driven camera system and the subjective evaluation of the pictures acquired with the camera during motion, are introduced. The developed camera orientation systems are able to outreach the high dynamic movement capabilities of the human oculomotor system.

Chapter 6 deals with the integration of the presented systems into different application scenarios. Besides applications for head–mounted gaze–driven camera systems, also a remote eye tracker, first steps towards equipping a humanoid robot head with "eyes" and eye–related Wizard–of–Oz platforms are reviewed. All scenarios profit from the feature of the developed camera orientation systems which combine high dynamic orientation output capabilities with a small and lightweight design.

The thesis concludes with Chapter 7 where the main results of the work are summarized and directions for future research are outlined.

1.3. Role of the Thesis within the Project Consortium

The research presented in this thesis is embedded in the Cluster of Excellence "Cognition for Technical Systems – CoTeSys" founded by the German Research Foundation (Deutsche Forschungsgemeinschaft, DFG). The Technische Universität München coordinates the cluster, which was founded to enable close interdisciplinary collaboration between scientists from various disciplines connecting neurocognitive and neuro–biological foundations to engineering sciences at leading research institutions in Munich.

The aim of the thesis is to develop and control compact high dynamic camera orientation systems which are specifically designed for the needs of the projects "Action recognition from look–ahead fixations of objects in space with self–calibrating gaze control of head–mounted stereo cameras" (project #106) and "EyeSeeCam: Natural Visual Exploration and Interaction in Humans and Robots" (project #414). Furthermore, the camera orientation systems are also adapted to other application scenarios (remote eye tracker, active vision system for humanoid robots as well as eye–related Wizard–of–Oz scenarios) within the CoTeSys cluster.

2. Conception

In this work mechatronic devices are designed and controlled, which are able to reproduce movements of the human oculomotor system. To provide a better insight into this topic, the most relevant human eye capabilities are introduced in Section 2.1. Based on these facts, the requirements posed to the technical system are formulated, see Section 2.2. The state–of–the–art concerning small and high dynamic camera orientation systems is given in Section 2.3. Different approaches for the development of novel systems are introduced and compared. The most appropriate approach is detailed in Section 2.4. Finally, Section 2.5 summarizes this chapter.

2.1. Human Oculomotor System

The visual system is one of the most important parts of the central nervous system and allows humans to build a model of the environment evaluating visible light. Three dimensional representations are produced by the human brain from monocular pictures acquired with the eyes, even under dynamic conditions and varying light intensity. Interested readers can find an extensive introduction to eye–related neurology topics in Leigh and Zee [60], while the whole human neurology is reviewed in Kandel et al. [54].
The human eye can be depicted as the sensor of the visual system. Through the *Cornea* the light passes into the *Bulbus oculi* (the eyeball) stimulating the retina. In doing so, the visual signals are converted to electrical signals and transmitted by the *N. opticus* (the optic nerve) to the central nervous system, see Figure 2.1.

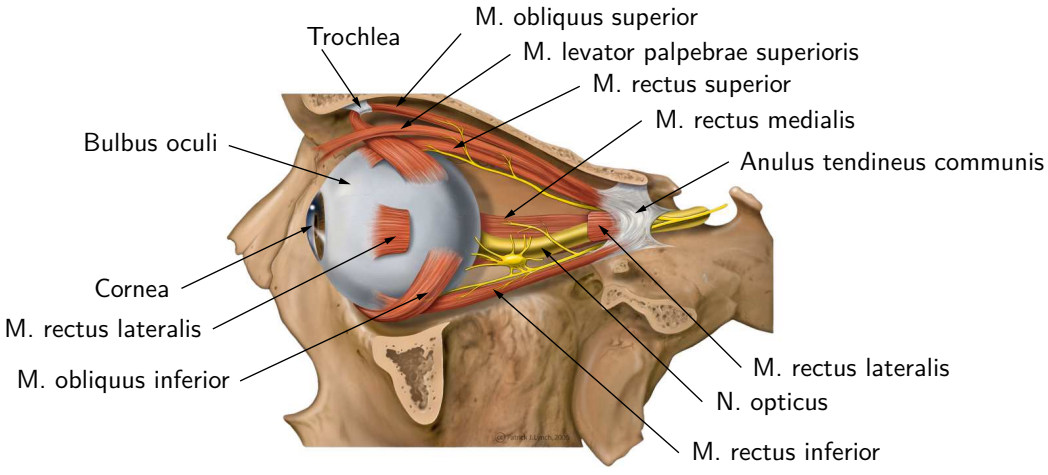

Figure 2.1.: Human oculomotor system (left lateral), modified from [67].

The eyeball is an approximate sphere which is able to rotate freely. To steer the eye, the extra–ocular muscles (*musculi bulbi*) are used. In doing so, the muscles *M. rectus lateralis* and *M. rectus medialis* orient the eye around an approximately vertical axis. The muscles *M. rectus superior* and *M. rectus inferior* are used to orient the eye around an almost horizontal axis. Finally, a third pair of muscles *M. obliquus inferior* and *M. obliquus superior* is deployed to rotate the eye around a nearly longitudinal axis. The latter muscle is deflected using the so called *Trochlea*. Since the three axes are not orthogonal to each other, the center of rotation moves slightly during rotation. In Figure 2.1 also the *Anulus tendineus communis* (also called *Anulus of Zinn*) is depicted. This ring of fibrous tissue surrounding the optic nerve (*N. opticus*) is the origin for five of the six extra–ocular muscles. The *M. levator palpebrae superioris* is deployed to elevate and retract the upper eyelid.

Using the three pairs of extra–ocular muscles humans are able to orient their eyes around three axes[1]. However, only two orientations, namely the rotations around the vertical and around the horizontal axes, can be voluntarily controlled by humans. The eye deflections around the longitudinal axis are adjusted automatically by the human brain. This relation is known in the literature as Donders' law. Based on this statement Listing's law is formulated to calculate the longitudinal deflection by a given vertical and horizontal orientation. For more information about these laws refer to [112].
Mathematical approaches to characterize Listing's law are introduced e.g. by Cannata and Maggiali [17], by Haslwanter [49], and by Polpitiya et al. [87]. However, as Haslwanter states Listing's law is valid only for an erected and stationary head, with the eyes looking at targets in infinity. Studies reported that Listing's law fails if the human head orientation is changed, the eyes are performing movements, or the gravity is changed, see e.g. [20, 40, 103]. So far, no complete relation that regards all these factors, is known in the literature.

Controlled by the human brain the eyes fulfill different kinds of movements. In the following the most important eye movements and reflexes are described. For a more detailed introduction refer to [19] and [60].

- *Fixation:* To investigate objects, or to read words, people fix their eyes on them. However, to compensate unwanted eye drifts small corrective movements are fulfilled. Thus, also during fixation the human eyes do not stay completely still.

- *Vergence:* In case of vergence movements both eyes rotate simultaneously with the same velocity but in the opposite direction. By doing so, near and far targets can be focused.

- *Smooth pursuit:* The human ability to follow slow moving objects with the eyes is called smooth pursuit. During these phases the human eye moves with velocities of up to 100 deg/s.

1 Besides rotation the human eye is also subject to translations, see [35]. Since these translations are very small they are neglected in most investigations.

- *Saccades:* Humans continuously explore their surrounding area with saccadic eye movements. Such an abrupt change of gaze direction occurs with velocities of up to 500 deg/s and with accelerations of up to 25000 deg/s^2, depending on the amplitude of the saccade. The larger the saccade, the higher the velocity and the acceleration.
- *Vestibulo–ocular reflex* (VOR): This reflex detects human head movements by means of the organ of equilibrium and causes the eye to move in the opposite direction at the same speed. In doing so, the line of sight remains constant and humans are able to acquire sharp images, even under dynamic conditions. This compensation process has a latency of about 12 ms.
- *Optokinetic reflex* (OKR): The optokinetic reflex is used to stabilize the human eye as well. To estimate the required compensation this reflex evaluates the acquired image. While the faster VOR compensates brief movements, the OKR is mainly used to deal with sustained movements.

The maximum working range of the human oculomotor system is about ±55 deg. However, according to Guitton and Volle [47] the amplitude is limited neurologically to about ±45 deg. They call it the *effective oculomotor range* (EOMR). However, humans typically rotate their heads together with the eyes, so the full EOMR is used only rarely, see [105].
Experiments reveal that humans normally align their eyes with an accuracy of about 1 to 2 deg to targets. This can be explained by the fact that the human fovea (the part of the human eye which allows one to acquire pictures with the highest resolution) has an aperture of about 2 deg, see e.g. [60]. However, Brunstetter et al. illustrated that humans are able to track objects with an accuracy of up to 0.16 deg under extreme gaze fixation [14].
As mentioned before the fastest human eye movements are the so called saccades. According to Carpenter and Leigh and Zee, depending on the amplitude, they can reach velocities of up to 500 deg/s and accelerations of up to 25000 deg/s^2, see [19] and [60].
Investigations concerning the frequency transfer characteristics of the human eye confirmed that the eye can be roughly modeled as a first–order low–pass system. The characteristic frequency is about 1 to 2 Hz, see [19] and [42].

2.2. Requirements

One possibility of gaining "natural" stabilized images even under dynamic conditions is to track the human eye movements and to continuously reproduce them with a technical system.
To reduce complexity we decided to first develop a system which is able to orient a camera around the two most important axes of the human eye, vertical (left/right) and horizontal (up/down), where a workspace of about ±30 deg must be covered. The camera orientation must be detected with a resolution of 0.1 deg, which is better than the resolution of the human oculomotor system. To preserve the natural

stabilization effect eye velocities up to 500 deg/s, accelerations up to 25000 deg/s^2, and a characteristic frequency of more than 2 Hz should be provided by the technical system. Furthermore, small latencies between human and artificial eye movements in the range of the human vestibulo–ocular reflex (around 12 ms) are required. Since the system is worn by a human it is important to achieve a small and lightweight design. To guarantee high orientation accuracy, moreover, a design with small backlash is desired.
Based on the results achieved by the two DoF camera orientation systems, a system which is able to orient a camera around all three axes is developed. Basically, this system must cope with all requirements already posed to the previous system. However, taking into account experiences gained with the predecessor requirements are refined. Since in normal conditions humans orient their eyes only in a small range [105], the needs of the accessible workspace are reduced to about ± 20 to ± 30 deg for all three orientations. Demands on the resolution of the camera orientation system, however, are increased and should preferably be greater than 0.02 deg. In doing so, the evaluation of the acquired images is simplified. Experiments with the previously developed systems have revealed that they are small and light enough to be head worn. However, to affect users as little as possible the package dimensions must be further reduced.

2.3. State of the Art

In this section the state–of–the–art of digital image stabilization (DIS) and active camera orientation systems is introduced.

During DIS images are stabilized by software algorithms without needing supplementary mechatronic systems. In the literature several investigations on customer electronic devices, such as hand–held cameras, see [12] and [76], are known. Compared to human eye movements, such cameras are subject to slow orientation changes only. Furthermore, usually only a restricted field of view is acquired.
One of the most important steps during DIS is the detection of corresponding points in consecutive image frames. According to Szeliski [104] algorithms can be classified into two categories: feature tracking approaches (e.g. KLT tracker [66]) and feature matching approaches (e.g. SIFT matcher [65]). Usually, feature-tracking-based approaches are faster than feature-matching approaches, but they are not useful if features with a large motion must be tracked. However, the main drawback of DIS approaches is the required high computational cost if a large field of view must be covered and at the same time fast motions must be stabilized. Since the computational amount is not manageable with portable systems, these approaches do not suit the application.
To reduce the computational amount Ryu et al. introduced an approach where a KLT tracker is combined with an inertial measurement unit (IMU), see [90]. Using the IMU movements in images are roughly estimated and used as starting points for the tracker. By doing so, the speed and the accuracy of the tracking process is enhanced. But the computation amount is still too high for portable computers.

An artificial eye implant is presented by Gu et al. [45]. This device is very small and intended to be used as an ocular prosthesis. However, only one DoF is reproduced by the system. Wolfe et al. introduced an artificial eye replacement with two active DoF [119]. To create a compact design shape–memory alloy actuators were used. Hence, only small velocities can be achieved. Biologically inspired humanoid robot eyes are presented by Lenz et al. and Wang et al.. Both use the same actuator principle: pneumatic muscles. Like human muscles this technical analogue is able to provide tractive forces only. Thus, always two actuators are used to ensure one DoF. While in [61] four pneumatic muscles orient a camera around two DoF, in [117] six muscles are utilized to provide three DoF. Due to the driving principle, the actuators need compressed air. Thus, a supplementary transformation of operating energy is needed. This will result in a higher overall mass and size. To overcome this drawback, Cannata and Maggiali replaced the pneumatic muscles by four tendons which are driven by DC motors [16]. This system is able to orient a camera around three axes with the required high velocities and accelerations. However, the system is too bulky to be mounted on a human head.

Besides these biologically inspired systems, a vast amount of technical inspired camera orientation systems are known in the literature. Such systems are frequently denoted as "Active Vision Systems". Applying diverse computer vision algorithms on the acquired images, the autonomy of (humanoid) robots as well as vehicles is increased. Often active vision systems are equipped with a stereo camera pair. Devices where the entire stereo camera pair is oriented around its vertical (pan) axis and its horizontal (tilt) axis are wildly spread. Also systems where the cameras are oriented around a common horizontal axis and two separated vertical axis, one for each camera, are common. Thus, it is not possible to list all of them. A short extract can be found in [3, 24, 27, 107]. These camera orientation systems are able to provide the required high velocity and acceleration output capabilities. However, they do not meet the requirements of compactness and lightweight. Small and lightweight active vision systems are also known in the literature, see e.g. [46]. But this device does not meet the velocity requirements.
A subsection of the active vision systems are the so called "Emotion Displays", see e.g. Kismet [13] and Eddie [101]. As the name implies, these devices are used to present emotions to users and to determine the emotions of users. Therefore, these systems are equipped with integrated camera "eyes". However, the camera orientation systems are not able to provide the desired high velocities and accelerations, while at the same time being small in size and weight.

Another very popular technical inspired camera orientation system is the "Agile Eye" introduced in [44]. The spherical manipulator is based on a parallel kinematic structure and is able to orient a single camera around three axes. The system exceeds the human eye velocity and acceleration capabilities. However, the device has a large size and high weight. Bang et al. used the kinematic structure of the "Agile Eye" to develop their "Anthropomorphic Oculomotor Simulator", see [6]. This system is able to orient a camera around three axes with velocities and accelerations superior than those of the human eye too. The authors revised the original design with particular focus on compactness. Thus, the device is able to

orient eyes in human-sized robotic heads. But the camera orientation system is still too heavy and bulky to be mounted on a human head.

Bederson et al. introduced a small and compact two dimensional magnetic actuator [9]. Again this device is used to steer a camera. Due to the reduced driving power and the friction in the device the camera can not be oriented with velocities comparable to the human eye. Based on a similar actuation principle Bassett et al. introduced an "Animatronic Eye" [8]. This compact and lightweight device is able to orient an artificial eyeball around three axes faster than humans orient their eyes. Using this approach, the technical system benefits from the low friction and low mass. In fact, only the eyeball is oriented while the camera is mounted statically behind the steering system. Thus, the system is able to simulate natural eye movements e.g. in dolls, while an active camera stabilization is not possible. Another very compact camera orientation system is presented by Hoshina et al. [52]. A spherical ultrasonic actuator is used to orient a camera around three axes with velocities comparable to the ones of the human eye. Because of the compact size only small torque output capabilities are achieved. A further drawback of the system is the relative high orientation accuracy error.

A camera orientation system is used by Park to improve the capabilities of a remote eye tracker [77]. The device is based on a serial kinematics and is able to orient a camera around two axes. However, the required high velocities and accelerations can not be reached. On the market pan/tilt web or surveillance cameras are available which are based on a similar configuration. Especially web cameras provide small overall dimensions, but they are not able to deal with the needed velocities.

A "Wearable Visual Robot" is introduced by Mayol et al. [69]. This small system is based on a serial kinematics driven by three model aircraft servo actuators. A camera mounted on the end-effector can be oriented around three axes. Using the built–in inertial measurement unit and evaluating the acquired images the camera is stabilized. Such a system finds its application in autonomous 3D map building, ego–localization, and in remote collaboration scenarios. However, due to the selected kinematic design and the chosen actuators the system provides only a limited stiffness. Therefore, the same authors present a parallel–plus–serial hybrid kinematic design approach [70]. However, no prototype based on such a kinematics is introduced. The system presented by Kurata et al. is inspired by the work of Mayol et al.. Thus, a similar approach is chosen [56]. As its predecessor, this system is shoulder-worn and based on a serial kinematics. However, the new device orients a camera and laser unit around two axes. The aim of the approach is to improve remote collaboration scenarios.

Schneider et al. used a small parallel kinematics to orient a camera around two axes [93]. The device is integrated into a head–mounted gaze–driven camera system. To drive the camera orientation device, model aircraft servo actuators are used. These very compact actuators have two major drawbacks: the non backlash–free gear boxes and the unidirectional pulse width modulated (PWM) interface. The latter introduces an additional time delay of 20 ms. By overclocking the PWM interface the authors reduced the delay. However, this implies a faster wear and

tear as well as higher energy consumption of the actuators. The design presented by WAGNER ET AL. is also based on a small parallel kinematics driven by model aircraft servo actuators [113]. Compared to [93] the mechanical design is improved and thus it is possible to orient a camera around three axes. This device finds its application in a head–mounted gaze–driven camera system, too.
A further small parallel kinematic camera orientation device is introduced by SCHNEIDER ET AL. [94]. This device is able to orient a camera around two axes with the required high velocities and accelerations. The design is based on the experiences gained with our camera orientation systems introduced in Chapter 3. In fact the same kinematic structure and actuators are used. Using an off–the–shelf gimbal joint (without ball bearings) and a different sensor concept (the same as we utilized for our three DoF camera orientation system, see Chapter 4) a compact and lightweight design is gained.

2.4. Approaches

Since the human eye is able to acquire high resolution images only in a very small field of view, humans continuously explore their neighborhood acquiring images from different gaze directions. These single pictures are then composed to an overall map by the human brain. To allow for this subconscious process, high dynamic eye movements are used to change the human gaze direction all the time. Besides these scanning movements, the human eye fulfills further high speed stabilization movements. In doing so, high quality images are acquired even under dynamic conditions like locomotion, see [60]. However, humans do not only use their eye movements to acquire image information, but also to communicate interpersonally, see [68].
In the following subsections different possible approaches to reproduce high dynamic changes in gaze direction are listed and evaluated.

2.4.1. Static Cameras

Early approaches that can be found in the literature are very simple from a mechatronic point of view. A static mounted high resolution camera is used to acquire the entire scene. To be comparable to the human eye such a camera must provide a resolution of about $130 \cdot 10^6$ pixels. Besides this high optical resolution, a high temporal resolution is also required. Only then sharp images can be acquired even under dynamic conditions, see [71]. As a matter of fact the required camera resolution would produce a high amount of data. This information can not be handled with a wearable evaluation system. VON HUNDELSHAUSEN presented an approach to reduce the amount of data, see [15]. Thereby a static camera system is used, where the acquired images resolution is adapted according to the gaze direction. Only those image parts that the user looks at are recorded with high resolution. The rest of the image is acquired with a lower resolution. Although the amount of

data can be reduced, it still exceeds the capabilities of wearable evaluation systems. A biologically inspired sensing system is presented in [99]. As for the human retina, the image resolution of this sensor is the highest in the central field of view and becomes lower rapidly towards the periphery. The systems are also known as fish–eye lenses. Using such sensors the amount of image data is reduced, while at the same time an overview image is acquired. However, without moving the camera, high resolution images can only be acquired for a straight gaze direction.
Furthermore, static mounted cameras allow only for little interaction with users. To enable eye–related nonverbal communication Bassett et al. put an "Animatronic Eye" in front of a static mounted camera [8], so that eye movements are imitated while the system's complexity increases.

2.4.2. Active Camera Orientation

A second line considers biologically inspired approaches. High speed saccades and stabilization movements of the human eye are reproduced by a technical system. Hence, a small camera is actively aligned to a different line of sight. With active stabilized cameras, the human central field of view is acquired. Thus, high quality images are acquired, while the amount of data is kept low. Selected camera orientation systems are introduced in Section 2.3 and their drawbacks are discussed. Principally, these approaches can be classified into three different groups: serial kinematics, parallel kinematics, and spherical actuators, see Figure 2.2. Of course combinations of these basic groups are also possible.

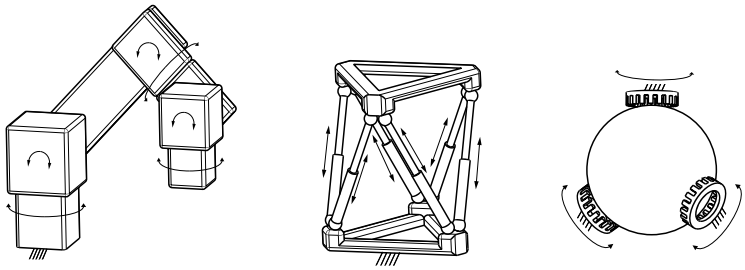

Figure 2.2.: Schematic concepts: serial kinematics (left), parallel kinematics (middle), spherical actuator (right).

The advantages and disadvantages of the different types of kinematics are extensively discussed in the literature, see e.g. [22, 72, 89, 100] for serial vs. parallel manipulators and [78, 106, 120] for spherical actuators. Therefore, here only the main differences and advantages of the single devices are presented.
Because of their simple design, serial kinematics, see Figure 2.2 (left), have been widely used. Since one DoF is arranged after the other, a large workspace can be realized. However, only the first actuator is mounted statically, such that besides the payload, the mass of remaining actuators must also be supported. This results in different force/torque requirements for the single actuators. Furthermore, particular attention must be paid to the system's stiffness.

A parallel kinematic system is characterized by a closed–loop mechanism, where a moving platform is connected to a base by at least two serial kinematic chains, see Figure 2.2 (middle). Compared to a serial kinematics, a parallel kinematics has the desirable characteristics of high payload and rigidity. However, the drawback is a limited working space and a more complex design. Since in a parallel kinematics all actuators are mounted statically, only minor inertial masses must be driven. Thus, it is possible to orient a camera with high velocities and accelerations also with small and compact actuators.
In recent years spherical (multi–DoF) actuators have been becoming more and more popular. They have the advantage that a serial or parallel mechanism is replaced by a single actuated spherical joint. Since only small masses must be oriented, high dynamic motion can be produced. A drawback of these actuators is their complexity. If high output torques and a large workspace is required, the actuators become bulky. Furthermore, the joint orientation measurement becomes more costly compared to a system based on a serial or parallel kinematics.

2.4.3. Active Optical Path Variation

A third approach combines ideas of the two previously mentioned ones. Thereby, a static mounted camera is used to acquire images. One or more active oriented mirrors or prisms are inserted into the optical path. In doing so, it is possible to acquire images from different gaze directions, see Figure 2.3. Active vision systems, which are based on such a principle, are described in [27] and [115].

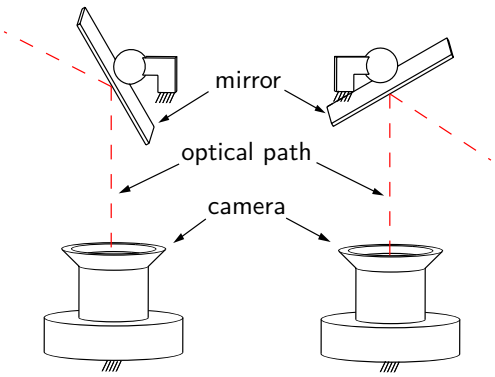

Figure 2.3.: Static camera with an active optical path variation.

The advantage of such an approach is that only very small masses must be oriented. The drawback is that the images acquired with the camera are distorted, depending on the mirror orientation. This causes supplementary effort during image processing. For the implementation additional components are needed and a certain distance between mirror and camera must be maintained. Therefore, the design becomes more bulky compared to a design where a camera is directly oriented.
Furthermore, systems are known were the mirror is replaced by optical fibers. As before, the camera is mounted statically. The fibers are oriented to different locations

and so the line of sight is varied. The most popular application of this approach are endoscopes, see [21] for an overview. Theoretically very compact systems can be developed. Since for the fibers minimum bending radii must be guaranteed, the overall size of the device increases. Moreover, due to the fibers' brittleness only limited dynamics can be achieved.

2.4.4. Comparison

To reproduce high dynamic human eye movements different approaches were presented. All of them are able to acquire high quality images from varying gaze directions. In Table 2.1 the different approaches are compared with each other. With the evaluation criterion "reachable dynamics" we describe the velocity and acceleration output capability. With the criterion "accuracy" both the absolute and repetitive accuracy are denoted.
Due to the principle, static mounted cameras have to record the entire scene. Neither the camera orientation, nor the optical path is varied actively. For this reason, criteria relevant for active systems like covered workspace, reachable dynamics, and accuracy are not evaluated.

Table 2.1.: Comparison of different approaches to reproduce high dynamic eye movements.

		Complexity	Amount of image post–processing	Package dimension, overall weight	Covered workspace	Reachable dynamics	Accuracy
Static cameras:	Entire scene	++	- -	- -			
	Adapted resolution	++	- -	- -			
	Fish–eye	+	- -	- -			
Active camera orientation:	Serial kinematics	0	++	0	++	0	0
	Parallel kinematics	-	++	+	+	++	++
	Spherical actuators	- -	++	0	+	+	+
Active optical path variation:	Mirror/prism	-	0	-	+	++	+
	Optical fibres	-	++	-	+	-	+

++ excellent, + good, 0 average, - weak, - - poor.

From a mechatronic point of view, the complexity of static mounted cameras is quite low. Only a rigid fixation is required. However, the amount of recorded image data is very high. Therefore, high performance computer systems are needed to evaluate acquired images. A further drawback of static mounted cameras is that they allow only little interaction with users.

A large workspace is covered by serial kinematics, with the drawback of strong actuators and a heavy construction. Using a parallel kinematics only minor inertial masses must be moved. So a small and lightweight design is achieved at the cost of a more complex mechanism and a reduced workspace. An elaborate actuator and sensor system is required to develop a spherical actuator. The complexity and weight increases when besides high dynamic movements also a large workspace is desired.
By just varying the optical path, the moved inertial masses are further reduced. However, the complexity of the overall design and the evaluation of the acquired images increases.

For these reasons we decided to design new camera orientation systems based on small parallel kinematic manipulators. A detailed description of the developed systems with two and three DoF is given in Chapter 3 and in Chapter 4, respectively.

2.5. Discussion

To develop technical systems which are able to cope with the human eye movements, it is important to know the human eye properties. Therefore, the most important eye reflexes and movements and the output capabilities of the human oculomotor system were introduced in this chapter. Based on this information we formulated the requirements for technical systems which would be able to orient a camera around two axes. With the experience gained from these systems, requirements for the mechatronic system, which reproduces all rotational human eye movements, were refined. Subsequently, the state–of–the–art of technical systems was discussed. Since, to the author's knowledge, no system was able to fulfill all requirements, different concepts were introduced and compared with each other. The investigations illustrated that the most appropriate approach were camera orientation systems based on small parallel kinematic manipulators.

3. Camera Orientation Systems with two Degrees–of–Freedom

Information about a user and his intentions can be gained evaluating images acquired from the user's perspective. One possible solution to yield high quality images, even under dynamic conditions, is to align a camera with the human gaze direction. Therefore, human eye movements must be measured and reproduced using a technical system. If the latencies between human eye and camera movements are small enough, the camera orientation device is stabilized by the human vestibulo–ocular and optokinetic reflexes only. In this case the camera orientation system must cope with possible high dynamic human eye movements. Furthermore, the devices must provide a similar large workspace and provide a high resolution orientation measurement system. To allow for free user mobility the camera orientation system can be fixed on the human body. A compact and lightweight design is required to affect users as little as possible. Since human beings stabilize their heads, cameras mounted on it are subject to fewer motions than cameras fixed to other body parts. Hence, two mounting positions which are both situated on the human head are selected, see Figure 3.1. Furthermore, the arrangement of the eye trackers, which are used to determine the human gaze direction, is depicted.

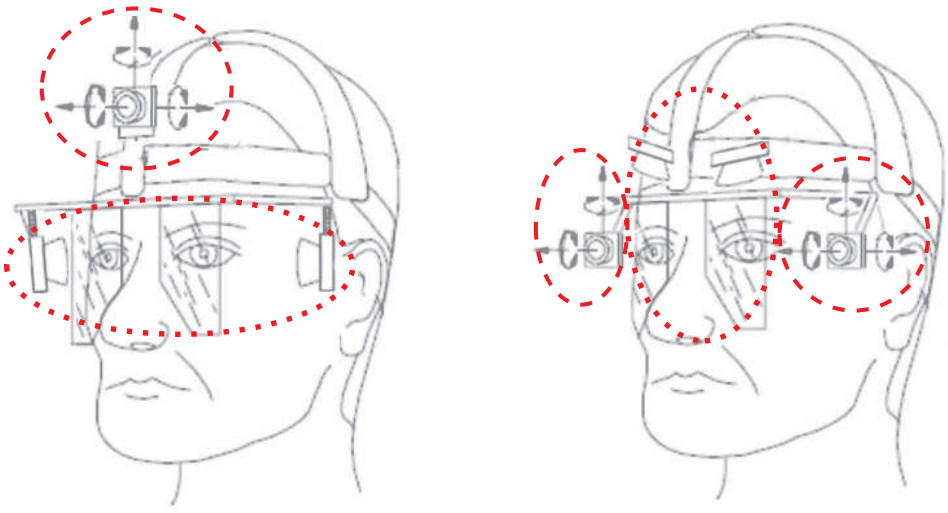

Figure 3.1.: Mounting position of the camera orientation devices [– –] and the eye trackers [· · ·]: mono camera system (left), stereo camera system (right), modified from [93].

In the first setup the camera orientation device is mounted on top of the human head, see Figure 3.1 (left). This configuration is called "mono camera system". For

the second setup two camera orientation devices are mounted at eye level, on the left and the right side of the human head, see Figure 3.1 (right). The second kinematic configuration is called “stereo camera system”.

In this chapter we present two camera orientation devices with two DoFs, which are intended to be mounted on the positions illustrated above. Although they have different mounting positions, the same kinematic structure is chosen for both. Only the kinematic parameters are varied. The selected kinematic structure is introduced in Section 3.1. In Section 3.2 the requirements on the actuators are formulated using a simple point mass model. Furthermore, requirements on the sensors are described. For both, actuators and sensors, different concepts are presented. Suitable evaluation criteria are formulated and the most appropriate approach is chosen. Subsequently, actuators and sensors available on the market are investigated. To compare the devices with each other the evaluation criteria are defined and then the selected actuators and sensors are introduced. In Section 3.3 the mechanical design is described. To reduce the mechanical design effort, identical parts are used as far as possible for both systems. Besides the nonlinear inverse kinematics, which account for the travel range limitations of the joints, also design parameters are introduced in Section 3.4. Furthermore, two different direct kinematic solutions are compared. The design is optimized conducting parameter variation studies. After that, the final kinematic parameters and the masses of the single components are determined. These data are used to parameterize kinematic and dynamic simulation models which are introduced in Section 3.5. According to the parameters gained from the simulations and the optimization process, prototypes were built. They are introduced in Section 3.6. A discussion in Section 3.7 concludes the chapter.

3.1. Kinematic Structure

To save weight and reduce complexity, a system reproducing only the two most important orientations of the human eye is designed first. Thus, a camera can be actively oriented around its vertical (pan) and its horizontal axis (tilt), see Figure 3.2.

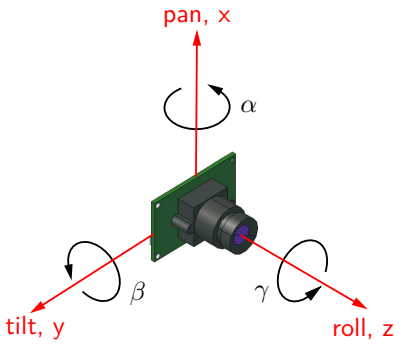

Figure 3.2.: Overview of the camera axes.

For the development of the camera orientation system a design based on parallel kinematics is chosen which is inspired by AGRAWAL ET AL. [1] and by WAGNER ET AL. [114]. We revised the original structure with particular focus on compactness and required high velocity and acceleration output capabilities. Only the two most important DoFs are provided. We further used completely different actuator and sensor concepts. Note that the chosen kinematic structure is popular and is also used for other robotic applications, e.g., to realize the ankle joints in the humanoid robots JOHNNIE [79] and LOLA [64].

In Figure 3.3 the selected parallel kinematic scheme is illustrated. The nomenclature is adapted from MERLET [72].

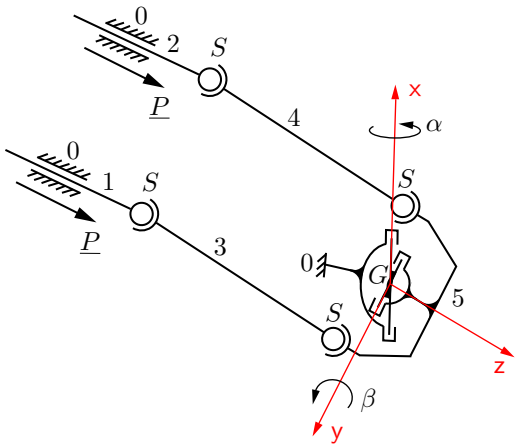

Figure 3.3.: Kinematic scheme of the system with two DoF.

The system is driven by two actuated prismatic joints $\underline{P}$. These joints are mounted on the base 0. The driving part of the joints is described as 1 and 2, respectively. Push rods 3 and 4 are coupled via spherical joints to the actuators and the camera frame 5, forming two so–called $\underline{P}SS$ chains. The joints are arranged in such a way, that lever arms around both camera axes are gained. Via a gimbal joint G the camera frame is connected to the base. This introduces an additional passive chain. A FICK configuration is chosen for the gimbal joint. Thus, in contrast to a HELMHOLTZ arrangement no rotation around the camera's optical axis occurs, when the camera is oriented around the pan and tilt axes [73].
To compute the mobility M of the designed mechanisms, the GRÜBLER formula can be applied, see e.g. [116].

$$M = 6(n - j - 1) + \sum_{i=1}^{j} f_i, \tag{3.1}$$

where n is the quantity of the used links and j the number of used joints. The connectivity of the single joints (DoF) is specified by f_i. The parameters are ascertained from the kinematic scheme, see Figure 3.3, and are listed in Table 3.1.

Table 3.1.: Mobility parameters.

Parameter	Value
Links, n	7
Joints, j	8
DoF prismatic joint, f_i	1
DoF gimbal joint, f_i	2
DoF spherical joint, f_i	3

The prismatic joints must be counted twice and four spherical joints are considered. For the calculations the gimbal joint is treated as two rotational joints connected to each other. Thus, the element consists of two DoF, two joints, and one link. Using (3.1), the mobility of the devices presented is calculated to four. However, only two DoF, the pan and the tilt orientation of the camera, can be directly controlled. As mentioned before, the push rods are equipped on both sides with spherical joints. Thus, they are able to rotate around their longitudinal (roll) axis which results in two supplementary DoFs. The rotations can not be controlled, but they do not influence the orientation of the camera. To eliminate the additional push rod rotations, however, the kinematic structure of the system must be modified. Then a spherical joint is attached only at one end of the push rods, while on the other end a gimbal joint is placed. Gimbal joints with a quality comparable in terms of backlash to the one of the used spherical joints demand more space. Because of the more compact design, and taking into account that the push rod rotations do not influence the camera orientation, we decided to equip the push rods on both ends with spherical joints.

3.2. Actuators and Sensors

In the following subsections the main requirements on the actuators and the sensors are formulated. Possible candidates are listed and their characteristics are described. Finally, the selected actuators and sensors are introduced.

3.2.1. Actuators

Orienting a camera with dynamics comparable to the human oculomotor system requires high velocities and accelerations. Rough estimations conducted with simple point mass models and more sophisticated multi body simulation studies suggested a velocity capacity up to 300 mm/s and desired forces up to 1 N, see Section 3.5. To suit the application, the actuators must be small, lightweight and have a high accuracy. Due to the special application scenarios, see Chapter 6, it can not be

avoided that users touch the camera orientation device[1]. Nevertheless, users must not get harmed and the system must not be damaged by such interactions.
Model aircraft servo actuators are used in [69], [93], and [114] to drive small camera orientation devices. These actuators are compact and able to provide the desired high velocities. Besides the disadvantage that the gear boxes have backlash, these actuators have only an unidirectional PWM interface [84]. The latter introduces an additional time delay of 20 ms. Theoretically the communication delay can be reduced by overclocking the PWM interface up to 500 Hz. However, this will result in faster wearing and higher energy consumption of the servo actuators. Using rotational DC or step motors necessitates the use of gears or spindles. In [115] DC motors with backlash–free gears are used to drive a mirror with human eye like movements. In the required small size the actuators are very fragile and therefore they will be damaged if a user interacts with the device. In recent years, linear electrical motors have become popular [11]. However, to the knowledge of the author there is no system available which meets the requirements in terms of needed forces and velocities and which at the same time is small in size and weight. Due to the driving principle, hydraulic and pneumatic pistons or muscles [23] need a supplementary transformation of operating energy, resulting in a higher overall mass and size. To guarantee high position accuracy in addition to position also pressure sensors are needed. Shape memory alloy actuators (SMA) [30] are light in weight and small in size, while providing high output capabilities. However, they are not able to provide the required velocities and accelerations. Electro–active polymers (EAP) [7] furnish high velocities and accelerations, but provide only small forces. The use of more actuators in parallel increases the output forces and the size. A further drawback of EAP's is their driving voltages. Voice coil actuators [43] are able to provide high forces and velocities. However, such systems do not meet the specifications because of their large overall size and mass. Another possibility to drive a camera orientation system is to use ultrasonic piezo–actuators, see [88] and [92]. These actuators are able to provide the required high velocities and accelerations as well as the needed forces. Because of their property to provide high force at low speed, no reduction gear is necessary.
In Table 3.2 the different actuator concepts are compared with each other. With the evaluation criterion *Reachable dynamics* we evaluate the velocity and acceleration output capability. With the criterion *Control* the accuracy and the complexity of possible position controllers are described.

Due to the additional time delay introduced by the PWM interface of model aircraft servo actuators the control criterion evaluates negative. In the literature a high amount of different control strategies for rotational motors can be found, which is positive. To assure high positional accuracy, sensors for position and pressure are needed to control hydraulic and pneumatic actuators, which rises the complexity.
According to Table 3.2 linear actuators based on rotational motors with spindles and linear ultrasonic piezo–actuators are the most suitable devices for this application.

1 The mounting position of the device is chosen such that no collision with the environment (e.g. the human head) occurs during normal operation. However, tests have confirmed that most users interact with the device during experiments.

Table 3.2.: Comparison of different actuator concepts.

Design Concept	Reachable dynamics	Provided forces	Package dimension, overall weight	Control
Model aircraft servo actuator	++	+	++	- -
Rotational motor with spindle	+	++	+	++
Linear motor	++	++	-	+
Hydraulic piston	+	++	- -	- -
Pneumatic piston or muscle	++	+	- -	- -
Shape memory alloy actuator	- -	++	+ +	0
Electro active polymer	++	- -	+ +	0
Voice coil	++	++	- -	0
Linear ultrasonic piezo–actuator	++	++	++	+

++ excellent, + good, 0 average, - weak, - - poor.

However, as mentioned before the small DC motors are quite fragile and would be damaged if a user touched the device. Due to the driving principle ultrasonic piezo–actuators have a built–in friction clutch. As a result users can interact with the camera orientation system without destroying the actuators. Thus, further investigations will concentrate on piezo–actuators.

Since the development of new piezo–actuators is not in the scope of this thesis, in the remaining work we will focus on actuators available on the market.
The investigated actuators are based on the same principle: The inverse piezoelectric effect transforms electric energy to a high–frequency motion of a small pusher. Via an intermittent frictional coupling the small movements are transmitted to a prismatic joint[2]. To control the actuator, joint positions are measured. On the market complete systems, consisting of pre–assembled piezo–actuator, prismatic joint, and measuring device, can be found. However, to yield maximum flexibility we decided to select single components and combine them to an actuator.
A vast amount of linear piezo–actuator kits are available on the market, see [50]. In Table 3.3 the most suitable actuators to drive the camera orientation system are listed. The criteria *Package dimension* and *Overall dimension* account for the piezo–actuator (without prismatic joint, power electronics, and measuring system) only. Comparing different ultrasonic linear piezo–actuators, *Physik Instrumente P–661*, was found to be the only model which meets the required velocities and forces. Table 3.3 reveals further that the P–661 are the heaviest. In theory eight X15G or two ST working in parallel have the same weight as one P–661. Of course the output capabilities of actuators working in parallel increases. However, also the complexity, the package dimension, and the required power electronics increases too. Thus,

2 For more information refer to Section 5.1.1.

Table 3.3.: Comparison of different piezo–actuators available on the market.

Manufacturer	Product	Reachable velocity [mm/s]	Reachable acceleration [mm/s^2]	Reachable forces [N]	Package dimension [mm^3]	Overall weight [g]
EDO Ceramics	PDA130, [31]	200	-	2.5	$18 \times 37 \times 5$	9
Elliptec AG	X15G, [33]	350	5000	0.1	$28.2 \times 11.2 \times 8.2$	1.2
Nanomotion Ltd.	ST Motor, [74]	250	-	1.3	$6.1 \times 21.9 \times 22.8$	5.5
Physik Instumente	P–661, [81]	600	150000	2.0	$14 \times 35 \times 6$	10

we decided to use P–661 from *Physik Instrumente* to drive the camera orientation systems.

3.2.2. Sensors

To orient a camera to desired orientations the selected ultrasonic piezo–actuators must be adjusted to predefined set positions. Closed loop control architectures are required to guarantee high orientation accuracy. Therefore, appropriate position sensors must be selected. As for the actuators, a compact and lightweight design is also required for the sensors. Even for very fast actuator movements (600 mm/s) sensors must provide reliable position feedback. Since the accuracy of the camera orientation system is affected by the sensors, they must further provide a high resolution. The camera orientation must be measured with a resolution outreaching the human eye fixation accuracy of about 0.16 deg which indicates a required sensor resolution of 0.1 deg.
To measure the camera orientation, sensors could be directly attached on the two axes of the gimbal joint. However, this would increase the inertial mass of the pivotable parts. Hence, this approach is not further investigated. A contact free three dimensional optical angular sensor, where only minor masses must be added to the pivotable parts, is presented in [59]. The sensor covers a large workspace, but has a maximum quantization error of more then 1 deg. Non contacting multi–dimensional magnetic sensors are presented for angle measurement in [53] and for angle velocity measurement in [58]. Particularly for the angle measurement only few masses must be added to the movable parts of the camera orientation device. However, similar to the optical sensors, the entire sensor system is comparatively quite large and therefore not applicable. In [102] the mathematical models for an optical binary spherical encoder are described. Since the sensor uses only binary input signals, the computational amount is small compared to [59]. The resolution of the encoder is bound by the fact that infinite orientations are represented by a limited number of binary combinations. Increasing the number of digital sensors yields a higher resolution, but also a larger design. Another approach to identify the camera orientation is to measure the piezo–actuator positions and to calculate the angles via the direct kinematics, which is introduced in Appendix A.1.3. The approach has the advantage that only the positions of the linear actuators must be determined. Thus, it is easier

to fulfill the requirements on accuracy and weight than when directly measuring the camera orientation.
In Table 3.4 different sensor concepts are compared with each other. With the criterion *Package, weight movable parts* we evaluate the package dimension and the weight of the sensor components which must be oriented altogether with the camera. Depending on the approach, the measured data must be evaluated to gain the camera orientation angles. This effort is incorporated in *Amount of data post–processing*.

Table 3.4.: Comparison of different sensor concepts.

Design concept	Achievable resolution	Package, weight movable parts	Package, weight overall system	Amount of data post–processing
Sensors attached to the gimbal joint	++	- -	0	++
Optical angular sensor	- -	++	- -	-
Magnetic angular sensor	0	++	-	-
Magnetic angular velocity sensor	0	+	- -	-
Binary angular sensor	0	+	- -	0
Linear sensor (one DoF)	++	++	++	+

++ excellent, + good, 0 average, - weak, - - poor.

Table 3.4 clearly reveals that measuring the linear actuator position is the most suitable approach. The camera orientation is calculated using the direct kinematic solution and the positions acquired with two single sensors.
In the literature different sensor concepts are reported, see [96] for an overview. A possible classification can be made according to the measuring principle: absolute or incremental. As the name implies absolute sensors always provide absolute position information. Incremental sensors give only relative information and an initialization procedure is required to gain absolute positions. The major drawback of absolute sensors on the other hand is their bulkiness. Thus, the following investigations concentrate on incremental sensors.
The most common incremental sensors are so called encoder systems. Basically such a device is composed of two elements: an encoder stripe and the encoder module. The encoder module measures the relative stripe movements. This implies that both elements are mounted on different sides of e.g. a joint. The lightweight encoder stripes can easily be adapted to different travel ranges. Thus, a high flexibility is gained[3].

Commercial products are also utilized for the sensors. Since a vast amount of linear sensor systems is available on the market, different devices are investigated and

3 In the literature so called resolver systems are also known. Basically, they use the same principle as encoders. The main difference is that encoders provide digital output signals while resolvers provide analog output signals. Since the evaluation of analog signals is more complex, resolver systems are not further investigated.

compared. In Table 3.5 the most suitable sensors are listed. Some encoders are able to evaluate a reference signal, called “index”, for initialization. Note that the criteria *Package dimension* and *Overall dimension* account for the encoder module only. The encoder stripe is not considered.

Table 3.5.: Comparison of different encoder systems available on the market.

Manufacturer	Product	Achievable resolution [µm]	Index signal [–]	Package dimension [mm^3]	Overall weight [g]
Avago Technologies	AEDR–8400, [5]	25	no	$3.28 \times 3 \times 1.26$	< 1.0
Encoder Technology LLC	LM720cpi, [34]	8.8	yes	$20.1 \times 13.7 \times 11.4$	4.0
US Digital	EM1-0-500, [109]	12.7	yes	$26.6 \times 11.4 \times 10.1$	–

Due to the high resolution, *LM720cpi* from *Encoder Technology LLC* are used for the development of the camera orientation system with two DoFs. The position can be measured with a resolution of 8.8 µm when using quadrature encoder evaluation. To evaluate the chosen sensor system the angular quantization error is of interest. The quantization error depends on the selected kinematic parameters and on the encoder resolution. As illustrated in Section 3.4, the maximum error of the mono camera system is about 0.09 deg and about 0.063 deg for the stereo camera system. In both cases the selected sensor system has a higher resolution than the human oculomotor system, see [14]. Furthermore, it can be stated that the sensor system fulfills the resolution requirements of 0.1 deg.

3.3. Mechanical Design Description

To reduce the mechanical design effort, as far as possible identical parts, such as the custom made gimbal joint and the camera mounting frame, are used for both camera orientation systems. Computer–aided–design (CAD) drawings[4] of the developed camera orientation systems are presented in Figure 3.4.
In the case of the mono system, Figure 3.4 (left), the camera orientation device sits on the human head. Thus, a flat design is required. A special mounting frame, adapted to the head dimensions, allows for a rigid fixation of the single components of the mechanism with respect to each other. The gimbal joint and the actuator unit are bolted on this mounting frame. The gimbal joint is equipped with two pairs of face–to–face arranged preloaded ball bearings which effectively reduces friction and assures a nearly backlash–free joint [48]. The actuator unit consists of the actuators itself, the sensors, and the prismatic joints. As indicated in the picture, actuators and sensors are serially arranged yielding a flat design.

4 For the work presented here all constructions are carried out using the 3D–CAD system *CATIA V5* from *Dassault Systémes*.

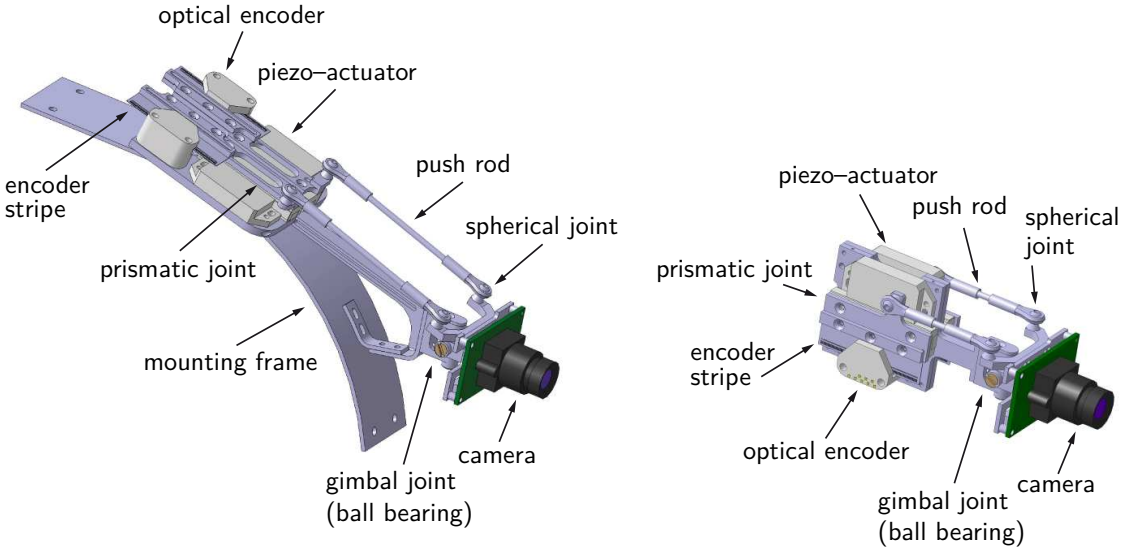

Figure 3.4.: CAD model of the mechanical setup: mono camera system (left), stereo camera system (right).

The stereo system, Figure 3.4 (right), is mounted on the left and right side of the human head. Therefore, a slender design is needed. Due to the compact design no supplementary mounting frame is required, hence the actuator unit is directly connected to the gimbal joint and so to the camera. The actuators and sensors are arranged facing each other and folded together.
To minimize the movable mass, the camera platform orientation is calculated from the linear actuator positions. Therefore, incremental encoder stripes are attached to the prismatic joints which are evaluated by the optical encoder modules. A cover (not shown) is fixed on top of the encoders to protect the linear stripes.

3.4. Kinematic Design Optimization

A camera orientation system which combines a large workspace (about $\pm 30\,\mathrm{deg}$), small quantization errors (less then $0.1\,\mathrm{deg}$), with compact overall size is required. Thus, to determine and optimize the workspace the nonlinear inverse kinematics is calculated. This model does not only take the kinematic structure of the system into account, but also the travel range limitations of the prismatic, gimbal, and spherical joints.

$$\boldsymbol{q} = \boldsymbol{g}(\boldsymbol{w}). \tag{3.2}$$

Equation (3.2) denotes the general form of the inverse kinematic model $\boldsymbol{g}$. In the present case the linear piezo–actuator positions (θ_1, θ_2) correspond to the joint coordinates $\boldsymbol{q}$. The orientation angles (α, β) correspond to the world coordinates $\boldsymbol{w}$. The extensive inverse kinematic calculations are presented in Appendix A.1.1. Using (A.11) and (A.12) the theoretically desired actuator set points can be calculated from given camera orientation angles. As a matter of fact the prismatic, gimbal,

and spherical joints used provide only a limited operating range. We describe these restrictions with (A.13), (A.16), and (A.25), see Appendix A.1.2. If the conditions are not fulfilled, the desired orientation angles are out of range.
In Table 3.6 the maximum working range of the selected gimbal and spherical joints is listed. Furthermore, three prismatic joint configurations, providing different working ranges, are investigated. Based on the following analyses we selected the most suitable prismatic joint.

Table 3.6.: Operating range limits.

Joint	Limit
Prismatic, θ_{max}	$\pm$10 mm, $\pm$15 mm, $\pm$20 mm
Gimbal, O_{GJmax}	$\pm$42 deg
Push rod spherical, O_{PRmax}	$\pm$30 deg

We defined three kinematic parameters r_1, r_2, and l. The minimal distance between the push rod end points on the actuator base and the z–axes of the base coordinate system $\boldsymbol{S}_0$ is denoted with r_1. On the camera side this distance is described with r_2. The push rods length is denoted with l. We chose the minimal distances between the two end points on the actuator base and on the camera frame to be identical. Thus, push rod spherical joint distortions around the vertical and longitudinal axes are omitted in the home position. In doing so, the push rods are in parallel, see Figure 3.5.

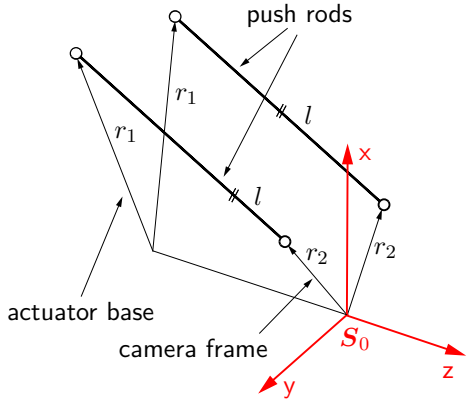

Figure 3.5.: Kinematic parameters in home position.

To determine the influence of the different design parameters r_1, r_2, and l, parameter variation studies are conducted considering the joint restrictions. These studies reveal: i) The smaller the parameter r_1 and r_2, the larger the workspace. ii) The larger the parameter l, the larger the workspace. The studies confirmed also that the parameter r_2 has the greatest influence.
By analyzing the spherical joint movements this can be explained. The joints mounted on the camera frame are subject to rotations. Since they are not situated in the center of the rotation, they are subject to translations too. The closer

the joints to the center, the smaller their relative movements. So, smaller spherical joint deflections are required and a larger workspace is yielded. On the actuator side the spherical joints are fixed to the prismatic joints. For that reason the attachment points are subject to translations only. Therefore, the requirements on the operational range of the spherical joints on the actuator side are smaller than the requirements posed to the joints mounted on the camera frame. Note further that the longer the push rods, the smaller the spherical joint deflections, and the larger the workspace. However, longer push rods imply also a larger package size.

Taking into account these considerations, the distances r_1 and r_2 should be minimized as much as possible. But reducing these parameters implies also drawbacks: the quantization error and the required actuator forces increase. As reported before, the camera orientation is determined by measuring the actuator position and calculating the direct kinematics. The closer the spherical joints are placed to the center, the larger the camera orientation changes by given prismatic joint displacements. Of course the selected sensors provide only a limited resolution. Thus, the closer the spherical joints, the larger the angular quantization error. The design parameters were varied systematically and the workspace as well as the quantization error was determined. Note that the models do not take into account the package dimensions or possible collisions between the single components. Therefore, the developed CAD models are used to determine the final parameters. Due to the different application scenarios for the camera orientation systems, two data sets were defined. They are indicated in Table 3.7.

Table 3.7.: Optimization results.

Propriety	Mono camera system [mm]	Stereo camera system [mm]
Distance r_1	40.12	21.21
Distance r_2	21.21	21.21
Push rod length, l	70	40

The selected prismatic joints are available with different working ranges. As mentioned before, to choose the appropriate range we investigated three different configurations. Considering the ascertained kinematic parameters, the achievable workspace is calculated and presented in Figure 3.6 for both the mono camera system (left) and the stereo camera system (right).

As the plot indicates the required workspace can not be reached using the joints with the smallest working range. A similar workspace is covered by the remaining two joints. Only in the small bottom left and right corners do the largest joints yield to better results. Compared to the entire workspace these areas are very small. Due to the smaller package dimensions we selected prismatic joints with a working range of $\pm 15\,\text{mm}$ to setup the camera orientation systems. By doing so, the presented

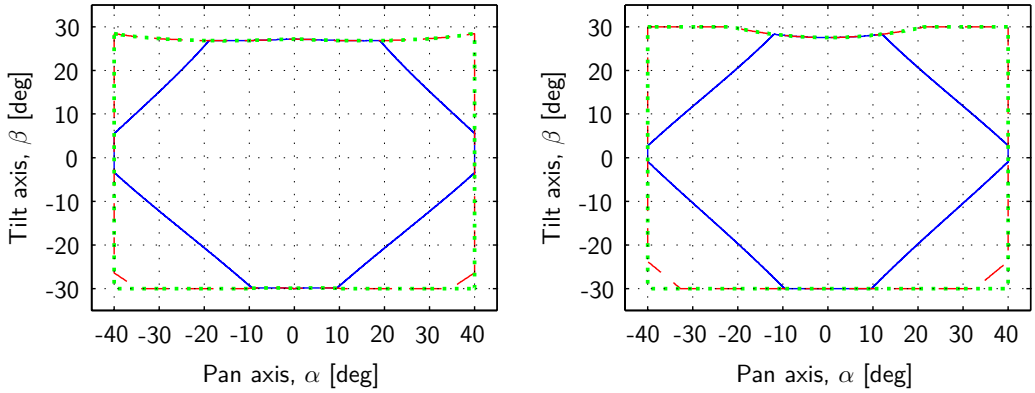

Figure 3.6.: Achievable workspace with different prismatic joints (±10 mm [—], ±15 mm [– –], and ±20 mm [· · ·]): mono camera system (left), stereo camera system (right).

devices achieve a workspace of about ±40 deg for the pan and nearly ±30 deg for the tilt orientation. The overall size is about 102 × 52 × 214 mm^3 for the mono camera and about 40 × 40 × 122 mm^3 for the stereo camera system.
In Figure 3.7 the maximum quantization error of both angular axes over the entire workspace is introduced for the mono camera (left) and stereo camera system (right). Due to the nonlinear relation between the actuator positions and the camera orientation the angular resolution is not constant over the whole workspace.

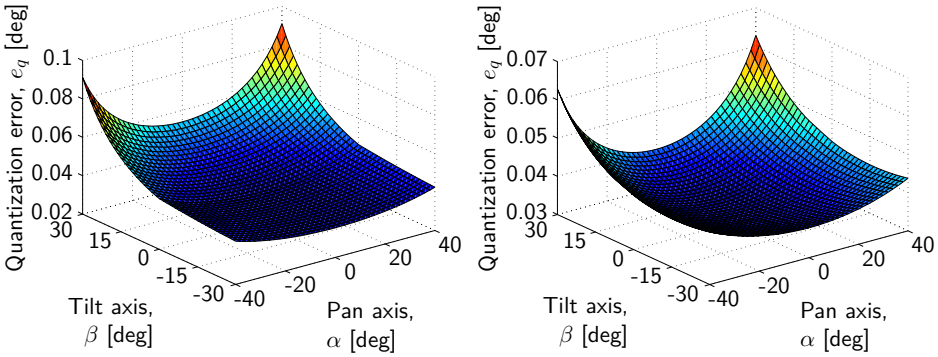

Figure 3.7.: Quantization error over the workspace: mono camera system (left), stereo camera system (right).

The plots suggest that the maximum quantization error occurs with large tilt angles and large or small pan angles. In this case the error is about 0.09 deg for the mono camera and about 0.063 deg for the stereo camera system. Usually a user's eye does not remain in this uncomfortable position very long. Hence, the mean error over the entire workspace is calculated, being less than 0.045 deg for the mono and 0.04 deg for the stereo camera system. As reported the camera orientation systems quantization error is below the human eye fixation accuracy of about 0.16 deg, see [14] for more information.

3.5. Kinematic and Dynamic Simulations

To prove that the selected actuators are able to drive the camera orientation systems, kinematic and dynamic simulations were performed. Therefore, two different models are established. In the first step, a kinematic model is developed and evaluated. With this model the required velocities are determined. In the second step, a multi–body system is simulated giving access to the entire system dynamics.

3.5.1. Kinematic Simulations

In the first step, a simple kinematic model of the camera orientation system is designed. Therefore, the nonlinear inverse kinematic solution, (3.2) is differentiated with respect to time. This yields to a linear projection between joint and workspace velocities.

$$\dot{\boldsymbol{q}} = \boldsymbol{J}^{-1}(\boldsymbol{w})\,\dot{\boldsymbol{w}}. \tag{3.3}$$

The kinematic model allows easy determination of the required actuator velocities $\dot{\boldsymbol{q}}$ over the entire workspace by given angular velocities $\dot{\boldsymbol{w}}$. $\boldsymbol{J}^{-1}(\boldsymbol{w})$ denotes the inverse Jacobian of the system. Since the manipulator is free of singularities for the desired workspace, the inverse Jacobian can be calculated as follows:

$$\boldsymbol{J}^{-1}(\boldsymbol{w}) = \frac{\partial \boldsymbol{q}}{\partial \boldsymbol{w}} = \frac{\partial \boldsymbol{g}(\boldsymbol{w})}{\partial \boldsymbol{w}}, \tag{3.4}$$

where $\boldsymbol{g}$ denotes the inverse kinematic solution, $\boldsymbol{w}$ the orientation angles and $\boldsymbol{q}$ the joint values.
Simulations are carried out to prove that the selected piezo–actuators are able to provide the needed velocities. To simulate the most ambitious case, we chose the fastest human eye movements. These movements are called saccades and can reach velocities of up to 500 deg/s. Investigations confirm that contemporaneous movements around all axes are the most challenging. Thus, saccadic movements around both axes are simulated at the same time. In doing so, desired velocities are calculated for the single actuators for every orientation within the workspace. However, to verify that the actuators suit the application the maximum needed velocity is of interest. Thus, only the maximum absolute required velocity of the linear actuators over the workspace is depicted in Figure 3.8.

On the left side of Figure 3.8 the required linear velocities for the mono camera system are introduced. To drive the camera in the described way, velocities of up to 260 mm/s are necessary. As the right side of Figure 3.8 depicts, similar actuator velocities, up to 260 mm/s, are needed to drive the stereo camera system. According to the data sheet the actuators are able to provide velocities of up to 600 mm/s [81]. Based on the presented observations it can be stated that the actuators are able to drive the camera orientation systems with the desired constant velocities. To

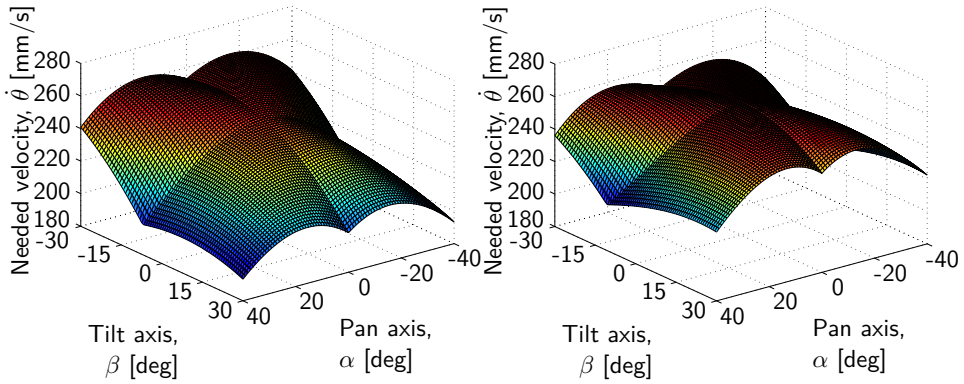

Figure 3.8.: Kinematic simulation results with velocities of 500 deg/s around both axes: mono camera system (left), stereo camera system (right).

determine whether the actuators can also cope with high dynamic velocity changes further investigations with a dynamic model are required.

3.5.2. Dynamic Simulations

For an appropriate actuator selection besides the needed velocities, the required accelerations and forces play an important role. While the velocities can be calculated with a kinematic model, a dynamic model is required for the accelerations and forces. To reproduce the entire system behavior the dynamic model accounts for the inertial masses and for the friction in the joints. Such a multi–body model is derived by the evaluation of the Lagrange or Newton–Euler equations. We used the multi–body simulation tool *MBSim*[5] which is based on a Newton–Euler formalism.
Because of the high stiffness and the low weight of the utilized parts, elastic deformation during the motion can be neglected. Therefore, the parallel kinematics presented are implemented as a rigid body model and parameterized appropriately. Based on this description *MBSim* is able to internally generate and evaluate the dynamic equations.
The inertia matrices of the single parts, needed for the dynamic model parameterization, can be directly derived from the CAD model. In Table 3.8 the mass of the movable parts for both the mono and the stereo camera systems are presented. Since the stereo camera system is more compact, the masses of the single parts are smaller.

The mass denoted with *Camera* holds the camera, the camera mounting frame and the gimbal joint. The mass denoted with *Push rod* accounts for the push rod itself and for the two attached spherical joints. Finally, the mass denoted with *Prismatic joint* implies the movable part of the prismatic joints, the linear encoder stripes and the mounting frame for the encoder stripes. The inertial mass of the *Push rods* and

5 *MBSim* is an open source **M**ulti **B**ody **Sim**ulation tool which was developed at the Institute of Applied Mechanics, TUM, see [39]. Is available on http://mbsim.berlios.de, June 2010

Table 3.8.: Mass movable parts.

Part	Mono camera [g]	stereo camera [g]
Camera	17	16.5
Push rod	1.5	1.2
Prismatic joint	14	13.2

the *Prismatic joints* is considered twice in the dynamic model, once for the left and once for the right actuator.

Among other component gimbal, spherical, and prismatic joints are used to set up the camera orientation system. Of course these joints have friction. To decide whether the friction must be considered in the dynamic model, we calculate the friction in the single joints.
The custom made gimbal joint is equipped with four ball bearings. According to [91] the bearings frictional torque $M_{F_{BB}}$ under normal loading conditions and with an adequate lubrication can be expressed as follows:

$$M_{F_{BB}} \leq \mu_{BB}\, F_{radial}\, \frac{d}{2}, \tag{3.5}$$

where μ_{BB} denotes the friction coefficient, F_{radial} the radial bearing load, and d the shaft diameter.The parameters used for the friction estimation in the ball bearings are listed in Table 3.9.

Table 3.9.: Frictional torque: ball bearing.

Parameter	Mono camera	Stereo camera
μ_{BB}	0.0015	0.0015
F_{radial}	0.47 N	0.51 N
d	1.5 mm	1.5 mm

The frictional coefficient of the ball bearings μ_{BB} has been taken from [91]. The maximum radial force F_{radial} applied to the bearings has been determined by dynamic simulation and reaches its maximum when saccadic eye movements are performed simultaneously around both axes. The frictional torque results in $M_{F_{BB}} = 0.57 \cdot 10^{-6}\,\mathrm{Nm}$ for a single ball bearing of the stereo camera system (worst case). Moreover, compared to the torque needed to accelerate the camera ($M = 4.5 \cdot 10^{-3}\,\mathrm{Nm}$) the ball bearings frictional torque can be neglected.

The frictional torque in the spherical joints $M_{F_{SJ}}$ is calculated using the following equation:

$$M_{F_{SJ}} \leq C_\alpha \frac{F\, r_{SJ}\, \mu_{SJ}}{\sqrt{1+\mu_{SJ}^2}}, \tag{3.6}$$

where C_α is a weighting factor, F denotes the external force applied to the spherical joint, r_{SJ} denotes the radius of the used ball, and μ_{SJ} is the friction coefficient. A detailed derivation of (3.6) with more information on the parameters is given in [37]. Table 3.10 presents the parameters used for the estimation.

Table 3.10.: Frictional torque: spherical joint.

Parameter	Mono camera	Stereo camera
C_α	1.0	1.0
F_{max}	0.51 N	0.39 N
r_{SJ}	2.375 mm	2.375 mm
μ_{SJ}	0.08	0.08

According to [37] the coefficient C_α is chosen to be equal to one. The maximum force F_{max} applied to the spherical joints is determined by dynamic simulations and occurs when the camera rotates with maximum velocity around both axes. Due to the higher masses of the driving parts the required forces are higher for the mono camera system. μ_{SJ} describes the frictional coefficient between the steel ball and the plastic joint socket. In the case of the mono camera system (worst case) the maximum frictional torque of the spherical joints is estimated to $M_{F_{SJ}} = 96.9 \cdot 10^{-6}$ Nm for each of the four joints. It can be assumed that any actuator must compensate the friction of two spherical joints. Furthermore, it can be stated that there is a distance of 9 mm between the point of application of the actuator force and the spherical joint center. By taking into account all this information the frictional force in the spherical joints results to $F_{F_{SJ}} = 0.0215$ N. With respect to the driving force this small frictional force can be neglected.
As mentioned before the force produced by the piezo–actuators is directly transmitted to the free direction of a prismatic joint. This joint is modeled as a mass–damper element, see Figure 3.9.

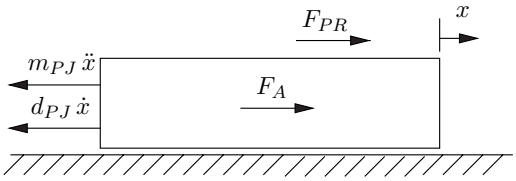

Figure 3.9.: Mass–damper model of the prismatic joint.

It can be described as follows:

$$m_{PJ}\,\ddot{x} = F_A - d_{PJ}\,\dot{x} + F_{PR}, \tag{3.7}$$

where m_{PJ} denotes the mass and d_{PJ} the damping coefficient of the prismatic joint. $\ddot{x}$ and $\dot{x}$ correspond to the prismatic joint accelerations and velocities respectively. F_A denotes the actuator force needed to drive the system and F_{PR} the force induced in the push rods.

The mass of the custom made moving parts and the prismatic joint m_{PJ} is obtained from the CAD model and from the data sheet respectively. According to the manufacturer the damping coefficient d_{PJ} varies from 0.1–0.2 Ns/m. In Table 3.11 the parameters used for simulation are introduced.

Table 3.11.: Frictional force: prismatic joints.

Parameter	Mono camera	Stereo camera
m_{PJ}	14 g	13.2 g
d_{PJ}	1.5 Ns/m	1.5 Ns/m

The simulation revealed that because of the required high velocities and accelerations of the linear actuators, the influence of the frictional force in the prismatic joints plays an important role. Thus, it has to be considered in the dynamic simulation model.
To recapitulate, the frictional influence in the ball bearings and in the spherical joints is negligible. However, the friction in the prismatic joints plays an important role and is therefore considered.

Dynamic simulations yield similar results for both the mono and the stereo camera system. In the following paragraphs the results obtained with the mono camera system are introduced. The findings related to the stereo camera system are reported in Appendix C.1.
As already mentioned, simultaneously orienting both axes with saccadic movements is most challenging. Thus, further investigations concentrate on this motion pattern.

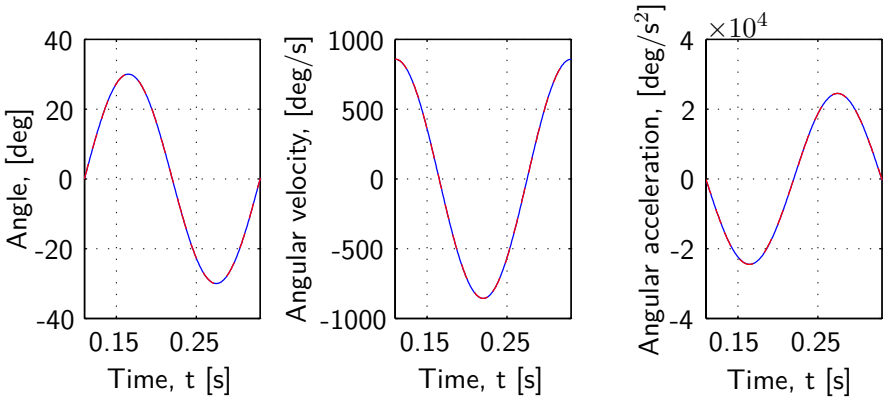

Figure 3.10.: Desired angles, angle velocities, and angle accelerations around the pan [—] and the tilt axis [– –].

Figure 3.10 (left) illustrates the desired angles for the simulation of saccadic movements. The angles change simultaneously with an amplitude of 60 deg. This simulated saccade covers nearly the entire workspace of the camera orientation device

presented. A desired sinusoidal angle movement has been chosen to imitate the human eye's accelerations and deceleration phases. Figure 3.10 (middle) indicates that the requested angular velocities exceed 800 deg/s. Finally, in Figure 3.10 (right) the calculated angular accelerations are plotted over time, indicating that the value of the peak accelerations are about 25000 deg/s^2. In Figure 3.10 pan and tilt movements can not be distinguished since the graphs are superposed in the plots.
Figure 3.11 presents the linear actuator positions, velocities, and accelerations calculated with the dynamic model when the values indicated in Figure 3.10 serve as input for the simulation.

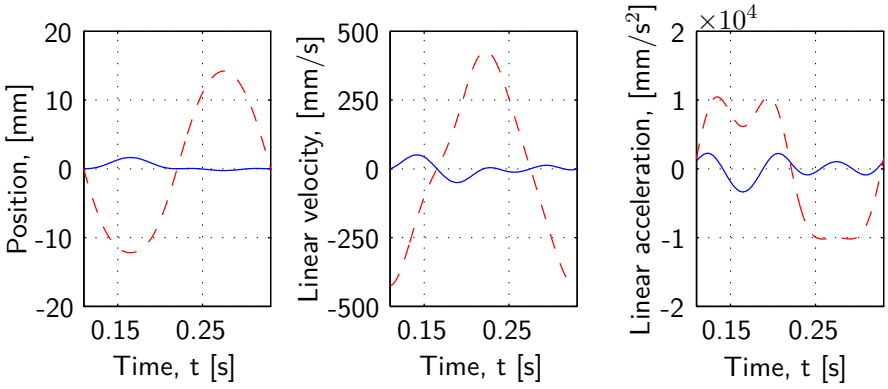

Figure 3.11.: Desired positions, linear velocities, and linear accelerations of actuator one [—] and two [– –].

Because of the special type of camera movements, from right down to left up, mainly the second actuator must contribute to the change of the camera orientation. Figure 3.11 (middle) confirms that maximum velocities of about 430 mm/s are needed to drive the parallel kinematics. The right side of Figure 3.11 reveals that peak accelerations of about 10000 mm/s^2 are required. Since the mechanical design of the camera orientation device is only left/right symmetrical, the desired actuator movements are not symmetrical. However, according to the actuators' data sheet, the needed velocities and accelerations can be provided.
The required linear velocities calculated with the dynamic model are higher then the velocities calculated with the kinematic model. For the dynamic simulations sinusoidal angular orientation changes between ±30 deg with a peak acceleration of 25000 deg/s^2 are used. Thus, the desired angular velocities for the dynamic simulation are higher than the velocities used for the kinematic simulation. As demonstrated the actuators are also able to cope with these requirements.
Figure 3.12 (left) presents the needed actuator force to drive the camera orientation system. Again it can be observed that the second actuator accelerates and decelerates the system, while the first actuator manly compensates the gravitational force. On the right side of Figure 3.12 a force/velocity diagram is shown where the outer rhomb (bold line) depicts the piezo–actuator limits according to the data sheet. Inside this rhomb two graphs are illustrated which represent the requirements posed to the actuators, which are smaller than the maximum available ones.

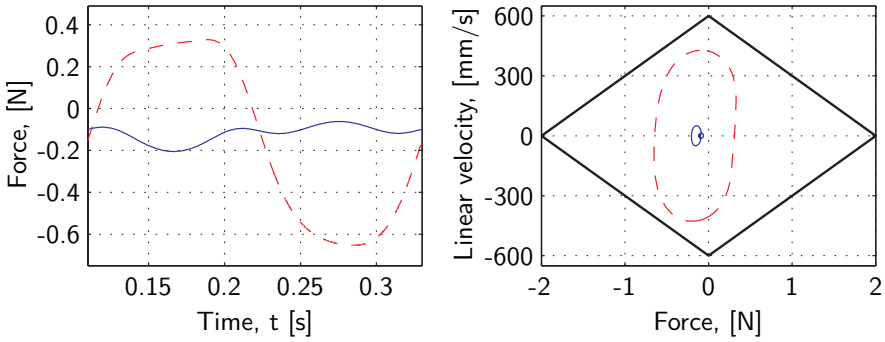

Figure 3.12.: Desired forces (left), force/velocity diagram (right) of actuator one [—] and two [– –].

Considering the presented simulations and the information obtained from the data sheet it can be concluded that the selected piezo–actuators are able to drive the camera orientation system with the needed high velocities and accelerations. However, in the considerations depicted model inaccuracies and the negative influence of the signal cable for the camera are neglected. As confirmed with experiments, see Chapter 5, the actuators power reserve is high enough to cope with these inaccuracies. Note further, that for the simulation we assumed saccades with an amplitude of 60 deg. According to [19] the amplitude of more then 90 % of the human saccadic eye movements are within 20 deg, which represents lower requirements to the system than the one presented.

3.6. Device Setup

Based on the data obtained from the simulations and the optimization process, prototypes were set up. The developed camera orientation systems are presented in Figure 3.13 (mono camera system) and in Figure 3.14 (stereo camera system). To save weight most of the custom made parts are manufactured from aluminum alloy (*AlZn5.5MgCu*). The tensioning screws and the shaft axles for the gimbal joints are manufactured from a high alloy chrome–nickel steel (1.4305) to guarantee supplementary stiffness. In the two pictures the oriented camera, *Firefly MV* from *Point Grey Research* [86], is also shown. This small camera is able to acquire pictures with a high frame rate and has a weight of about 11 g.

The mono camera system has a size of $102 \times 52 \times 214\,\text{mm}^3$ and an approximate weight of 130 g. To provide a deeper insight into the setup the encoder covers are omitted in Figure 3.13. The developed stereo camera system has a size of $40 \times 40 \times 122\,\text{mm}^3$ and an approximate weight of 115 g. Both systems cover a workspace of ±40 deg around the pan axis and nearly ±30 deg around the tilt axis. As presented in Chapter 5, angular velocities of over 1000 deg/s can be reached, which exceed the human eye capabilities of 500 deg/s [60]. To save weight and reduce complexity the camera orientation is calculated from measured linear actuator positions. Due to the nonlinearity in the kinematic solution, the angular resolution

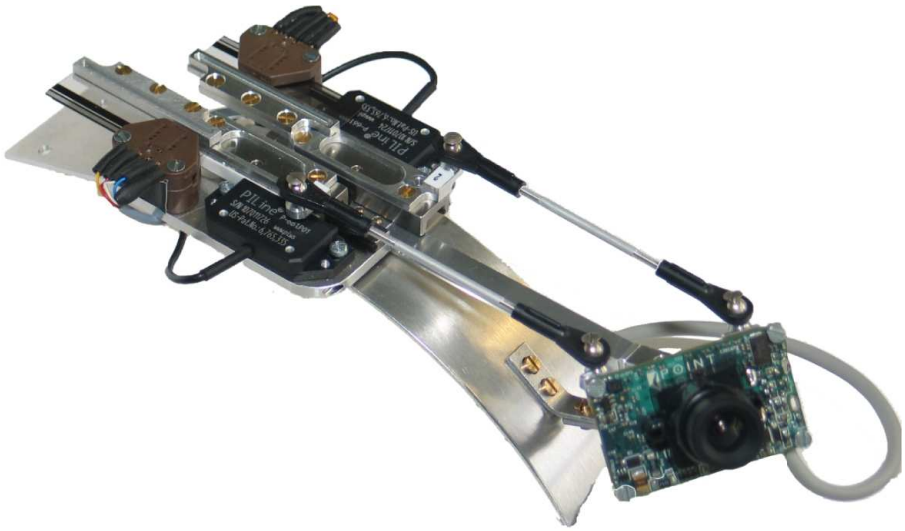

Figure 3.13.: Mono camera orientation system.

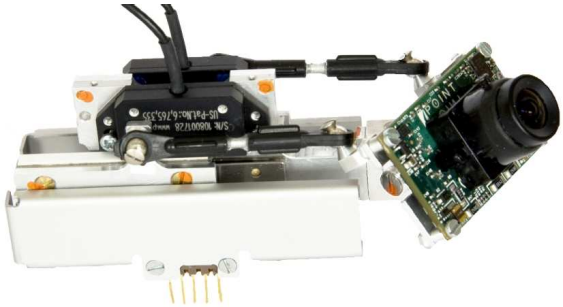

Figure 3.14.: Stereo camera orientation system.

is not constant. For the developed systems the maximum quantization error is about 0.09 deg for the mono and 0.063 deg for the stereo camera system. Although both have similar output capabilities, the overall mass and most notably the overall size of the mono camera system is larger. Due to the different application scenarios, the mono camera system requires a larger mounting frame, which makes the whole system heavier. The main specifications of both camera orientation systems are summarized in Table 3.12.

3.7. Discussion

In this chapter we presented and verified the design and the optimization of two configurations of a two DoF camera orientation system. Both are based on the same kinematic structure, which is adapted to the respective application. The developed devices are intended to be used as a part of a gaze–driven head–mounted camera system or as an artificial eye for humanoid robots. Thus, the devices must cope

Table 3.12.: Specifications of the mono and stereo camera orientation systems.

Propriety	Mono camera system	Stereo camera system
Covered workspace pan axis	± 40 deg	± 40 deg
tilt axis	nearly ± 30 deg	nearly ± 30 deg
Angular velocities	> 1000 deg/s	> 1000 deg/s
Maximum quantization error	0.09 deg	0.063 deg
Mean quantization error	0.045 deg	0.04 deg
Overall size*	$102 \times 52 \times 214\,\text{mm}^3$	$40 \times 40 \times 122\,\text{mm}^3$
Push rod length	70 mm	40 mm
Elevation angle	14.84 deg	0 deg
Actuator travel range	± 15 mm	± 15 mm
Overall mass*	130 g	115 g
Mass movable parts*	48 g	45 g

* The presented values do not account for cabling.

with the high velocities and accelerations of the human oculomotor system and at the same time be small and light in weight. Therefore, our proposed approach is based on a piezo–actuator driven parallel kinematic structure. To determine the workspace, the inverse kinematics considering the different joint limitations were calculated. Accounting for the application, the workspace/package dimension ratio was maximized. Both camera orientation systems provide a workspace of ± 40 deg around the pan axis and nearly ± 30 deg around the tilt axis. Furthermore, they are able to reach angular velocities of over 1000 deg/s and so outreach the capabilities of the human oculomotor system. A maximum quantization error of about 0.09 deg occurs for the mono and 0.063 deg for the stereo camera system. Both errors are below the human oculomotor system fixation accuracy of about 0.16 deg. The mono camera system has a size of $102 \times 52 \times 214\,\text{mm}^3$ and an approximate weight of 130 g. Due to the application the stereo camera system is more compact and has a size of $40 \times 40 \times 122\,\text{mm}^3$ as well as an approximate weight of 115 g. Besides a kinematic, also a dynamic simulation model was developed. Simulations were carried out using these models. Even for saccades, which can be considered the most challenging eye movements, the selected piezo–actuators suit the application. The simulation results were confirmed with closed loop control experiments, see Chapter 5.

4. Camera Orientation System with three Degrees–of–Freedom

The human gaze is one of the most crucial indicators of the direction of spatial and social attention. By evaluating images from the user's perspective, information about a user and his intention can be gained. As mentioned before a possible approach to acquire images with a high quality, even under dynamic conditions, is to align a camera with the human line of sight. In such a case a technical system is used to measure and reproduce the human eye movements. When the latencies between human eye and camera movements are small enough, the camera orientation system can be stabilized by the human vestibulo–ocular and optokinetic reflexes only. By doing so, supplementary image post–processing can be avoided. However, to gain this advantage the camera orientation device must cope with the high dynamic human eye movements and guarantee a large workspace. To allow for an accurate re–tracking of eye movements a high resolution orientation measurement system is required as well. In order to guarantee only minimal user restriction furthermore, a compact and lightweight design is needed. Due to the positive experience gained with the two DoF camera orientation systems, we selected again a mounting position on the human head for the system with three DoF. In addition to the arrangement of the camera orientation devices Figure 4.1 indicates also the mounting position of the eye tracker which is used to determine the human gaze direction.

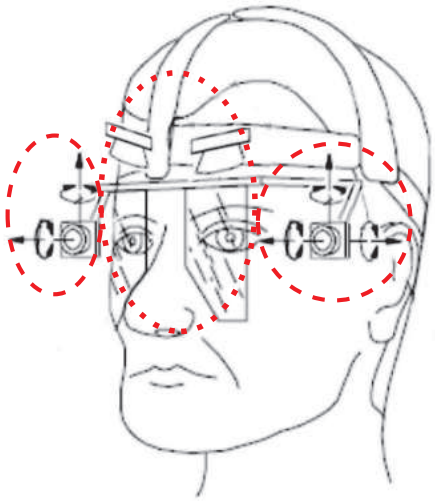

Figure 4.1.: Mounting position of the three DoF camera orientation devices [– –] and the eye tracker [· · ·], modified from [93].

The camera orientation devices are mounted at eye level on the left and on the right side of the human head. Using two cameras to acquire images of the user's surroundings has the advantage that three dimensional data, which also provides depth information, can be gained.
A three DoF camera orientation device is presented in this chapter. After formulating the requirements on the actuators and sensors, concepts and possible candidates are introduced in Section 4.2. Evaluation criteria are defined and based on them the candidates are compared with each other. Afterwards, the selected actuators and sensors are introduced. A deeper insight into the mechanical design is given in Section 4.3. In Section 4.4 the nonlinear inverse kinematics is introduced. In addition to the kinematic relations, this model also accounts for the travel range limitations of the selected joints. To optimize the workspace/package dimension ratio, parameter variation studies are conducted using an implicit filtering algorithm. Once the optimal kinematic parameters are determined, the masses of the single components are ascertained. Using these data the kinematic and the dynamic simulation models, derived in Section 4.5, are parameterized. Taking into account the findings obtained from simulations and the optimization process, a prototype was built, see Section 4.6. This chapter concludes with a discussion, reported in Section 4.7.

4.1. Kinematic Structure

Humans are capable of orienting their eyes around three axes. To reproduce these movements we developed a system which is able to actively orient a camera around its vertical (pan axis), its horizontal (tilt axis), and its longitudinal axis (roll axis), see Figure 4.2.

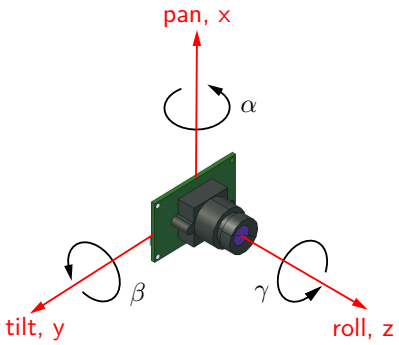

Figure 4.2.: Overview of the camera axes.

Based on the experience gained with the two DoF camera orientation systems, see Chapter 3, and our observations reported in [18] we decided to develop a three DoF camera orientation system based on a parallel kinematics.
The introduced kinematic structure is inspired by a parallel robot that was previously presented by Merlet [72]. We revised the original structure with particular focus on compactness and the required high velocity and acceleration output capabilities. Moreover, completely different actuator as well as sensor concepts are used.

Figure 4.3 reveals the selected kinematic scheme and the from MERLET [72] adapted nomenclature.

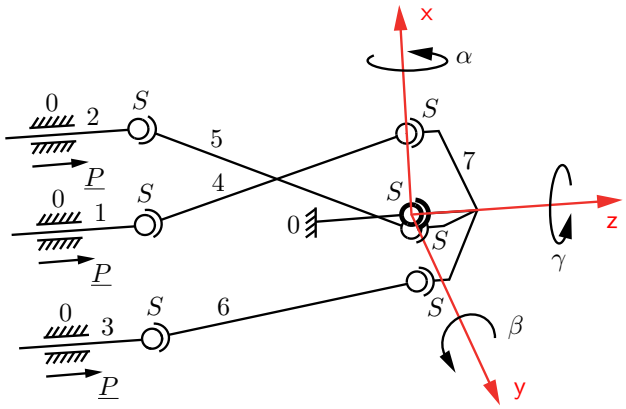

Figure 4.3.: Kinematic scheme of the system with three DoF.

Three actuated prismatic joints $\underline{P}$ are used to drive the system. The joints are fixed on the base 0, while 1, 2, and 3 describe the movable components of the joints. Push rods, with spherical joints S attached at both ends, are depicted with 4, 5, and 6 in the sketch. The actuator movements are transmitted via these push rods to the camera frame 7, forming three so–called $\underline{P}SS$ chains. The joints are arranged in such a way, that lever arms around all camera axes are gained. An additional passive chain with a spherical joint (bold in Figure 4.3) is used to connect the camera frame and the actuator base plate. By doing so, three rotational DoFs are ensured. Because of its central role we call this joint, "main spherical joint". On both sides (actuator base and camera frame) the pivot points of the push rod spherical joints are arranged on a circle, with 120 deg offset between each other. To avoid singularities the actuator base plate and the camera frame are rotated with 60 deg with respect to each other in the kinematics home position.
The mobility M of the investigated kinematics is calculated using the GRÜBLER formula [116].

$$M = 6(n - j - 1) + \sum_{i=1}^{j} f_i, \tag{4.1}$$

n depicts the amount of utilized links and j the quantity of the joints used. f_i describes the connectivity (DoF) of the selected joints. Based on the kinematic scheme, see Figure 4.3, the single parameters are ascertained. They are listed in Table 4.1.

Three prismatic joints, six spherical joints attached to the push rods, and the main spherical joint are considered. Evaluating (4.1) the mobility of the kinematics is calculated as being six. The pan, the tilt, and the roll orientation of the camera can be directly controlled. The other three DoFs result from the push rods. Since they are equipped on both sides with spherical joints, they are able to rotate around

Table 4.1.: Mobility parameters.

Parameter	Value
Links, n	8
Joints, j	10
DoF prismatic joint, f_i	1
DoF spherical joint, f_i	3

their longitudinal (roll) axis. Due to the kinematic structure these rotations can not be controlled. However, the camera orientation is not influenced. Modifying the kinematic structure the additional push rod rotations can be eliminated. In such a case, the push rods are equipped with a spherical joint at one end and a gimbal joint at the other. However, gimbal joints with a quality comparable in terms of backlash to one of the used spherical joints demand more space. Due to the more compact package dimensions and considering that the push rod rotations do not influence the camera orientation, the push rods are equipped with spherical joints on both ends.

4.2. Actuator Sensor Selection

In this section requirements on the actuators and sensors are introduced. Different possible candidates are presented and compared with each other. Furthermore, the chosen actuators and sensors are denoted.

4.2.1. Actuators

High velocities and accelerations are required to orient a camera with dynamics comparable to the human eye. Using a simple point mass model and more sophisticated multi body simulation models velocities of up to 300 mm/s and forces of up to 1 N are estimated, see Section 4.5. As for the camera orientation systems with two DoF, the actuators must be small in size and weight. Furthermore, they must have a high accuracy. The application scenarios, see Chapter 6, implicate that users touch the camera orientation device[1]. Neither the users must get harmed, nor must the system be damaged during such interactions.
Due to the positive experience gained with the linear ultrasonic piezo–actuators, *Physik Instrumente P–661*, the manipulator with three DoF is also driven by the same actuators. However, linear joints with a shorter working range and a more compact design are chosen.

1 As mentioned before, during normal operation no collision occurs between the device and the environment (e.g. the human head). But most of the users interact with the camera orientation device before or after the experiment.

4.2.2. Sensors

The camera orientation is adjusted by moving the chosen piezo–actuators to predefined set positions. To allow for high orientation accuracy closed loop control architectures are required. This implies the need for appropriate position sensors. These sensors must also guarantee reliable position information for the very fast actuator velocities (600 mm/s). To facilitate the evaluation of the acquired images the camera orientation must be measured with a resolution of 0.02 deg. This resolution outreaches the human eye fixation accuracy of 0.16 deg and the resolution of the two DoF camera orientation systems.

Several concepts to determine the camera orientation are introduced in Section 3.2. Measuring the linear actuator positions and afterwards calculating the camera orientation was found to be the most suitable approach. Therefore, also for the system with three DoF encoder stripes are attached to the linear joints. With static mounted encoder modules the stripe positions (and also those of the joints) are measured.

Since the three DoF system must be smaller and have a higher orientation resolution than its predecessors, new sensors are selected. The most suitable devices are listed and compared in Table 4.2. All of them are incremental encoders, thus they need to be initialized using a so–called "index" signal. Some sensors are able to evaluate this signal directly. The evaluation criteria *Package dimension* and *Overall dimension* accounts for the encoder module only, while the encoder stripe is neglected.

Table 4.2.: Comparison of different encoder systems available on the market.

Manufacturer	Type	Achievable resolution [µm]	Index signal [–]	Package dimension [mm^3]	Overall weight [g]
austriamicrosystems AG	AS5311, [4]	1.95	no	$7.0 \times 6.2 \times 1.1$	< 1.0
Numeric Jena GmbH	Kit L4, [75]	0.05	yes	$13 \times 8 \times 1.2$	1.0
Sensitec GmbH	SST03, [98]	0.5	no	$9.8 \times 9.4 \times 2.9$	< 1.0

For the development of the three DoF camera orientation system *Sensitec SST03* sensors are chosen. Since the selected encoders do not provide an index signal a supplementary sensor *Honeywell 2SS52M* [51] is used to initialize the measuring system. As Table 4.2 suggests, the sensor *Numeric Jena L4* has about the same overall size while providing a ten times higher resolution. However, due to the larger encoder stripes and due to the arrangement of encoder module with respect to the stripe, the overall size increases.
The *Sensitec SST03* sensors are composed of a resolver module and an on–board micro controller, which converts the analog signals directly to encoder signals. By programming the micro controller, the linear resolution is optimized with respect to the maximum velocity of the selected piezo–actuators. After this adaption and

quadrature encoder evaluation the sensors are able to measure positions with an accuracy of 0.5 µm. To evaluate the chosen sensor system the angular quantization error is of interest. The quantization error depends on the selected kinematic parameters and on the encoder resolution. For the developed camera orientation system a maximum quantization error of about 0.017 deg arises, see Section 4.4. Therefore, the high resolution requirements of 0.02 deg are satisfied by the selected sensor system.

4.3. Mechanical Design Description

During the mechanical design phase particular attention must be paid to the main spherical joint selection. This joint must be small and guarantee a large workspace while at the same time small friction and backlash is required. Figure 4.4 illustrates three investigated approaches for the integration of the main spherical joint.

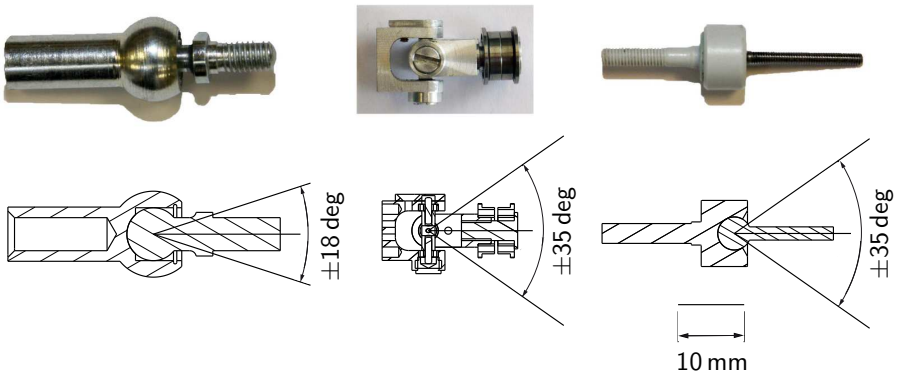

Figure 4.4.: Photos and sections of the investigated joints: off–the–shelf *MBO Osswald* (left), custom made *AM TUM* (middle), custom made *Kullborg Engineering* (right).

In the upper half of the picture photos of the joints are shown, while in the lower half the respective section is presented. On the left side of Figure 4.4 an off–the–shelf spherical joint from *MBO Osswald* is presented. It allocates only a small operational range and has further a high backlash and a high friction. In the middle of Figure 4.4 a custom made joint, based on a gimbal joint with an additional DoF is presented. A Fick configuration is chosen were the sequence of rotation corresponds to x–y–z [108]. The custom made joint is equipped with three pairs of face–to–face arranged preloaded ball bearings. Thus, the friction and the backlash of such a joint are negligible and a large workspace can be covered. However, the joint is quite bulky. In Figure 4.4 (right) a custom made spherical joint from *Kullborg Engineering* is presented. The joint provides a large workspace and has a compact design. The friction and backlash are negligible. Therefore, this joint is chosen to set up the camera orientation device.

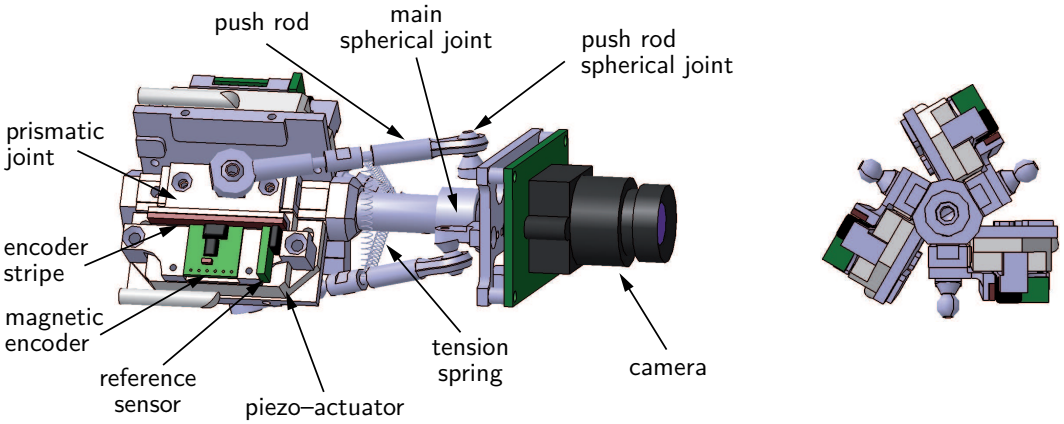

Figure 4.5.: Assembly of the mechanical setup: camera orientation system (left), star–shaped actuator unit in detail (right).

Figure 4.5 presents the full assembly of the developed camera orientation system. Actuators and sensors are stacked one upon the other on three single plates arranged in star–shaped manner, see Figure 4.5 (right), forming the so called actuator base. When the camera is oriented around the vertical and diagonal axes the spherical joints attached to the push rods guarantee a high accuracy. To avoid backlash during camera orientations around the roll axis the joints are preloaded. Therefore, three tension springs are used to connect the push rods with each other.
As stated before, the encoder modules and the reference sensors are mounted on the actuator unit. Using this sensor system the encoder stripes attached to the prismatic joints are evaluated and the joint positions are determined.

4.4. Kinematic Design Optimization

As for the camera orientation systems with two DoF, for the system with three DoF a large workspace (about ± 20 to ± 30 deg), a small quantization error (not more than 0.02 deg), and a compact overall size is also required. Experiments with users wearing the previously developed stereo camera orientation system illustrated, that besides a slender design it is also important to achieve a short design.
The nonlinear inverse kinematic solution, considering the travel range limitations of the joints, is ascertained to determine and optimize the camera orientation system workspace.

$$\boldsymbol{q} = \boldsymbol{g}(\boldsymbol{w}). \tag{4.2}$$

The general form of the inverse kinematic model $\boldsymbol{g}$ is described in (4.2). With this equation world coordinates $\boldsymbol{w}$ can be transformed to joint coordinates $\boldsymbol{q}$. In the investigated case the world coordinates correspond to the orientation angles (α, β, and γ) and the joint coordinates correspond to the linear piezo–actuator positions (θ_1, θ_2, and θ_3).

Due to the kinematic structure the derivation of the inverse kinematics is extensive. Thus, it is reported in Appendix A.2.1. For given camera orientation angles the theoretical desired actuator set points can be calculated using (A.54), (A.56), and (A.56), respectively. The joint limitations are considered with (A.57), (A.58), and (A.69). Table 4.3 depicts the operating range limits of the selected joints.

Table 4.3.: Operating Range Limits.

Joint	Limit
Prismatic, θ_{max}	± 11 mm
Main spherical, O_{Mmax}	± 35 deg
Camera side push rod spherical, O_{CPRmax}	± 30 deg
Actuator side push rod spherical, O_{APRmax}	± 20 deg

Depending on the mounting position, two different kinds of spherical joints are attached to the push rods. Since the spherical joints on the actuator side are fixed on the prismatic joints, the attachment points are subject to translations only. Thus, spherical joints, which guarantee a higher stiffness around the longitudinal axis, at the cost of a smaller working range, are chosen. The push rod spherical joints on the camera frame are subject to rotations and translations. Therefore, a larger working range is required compared to the joints fixed on the actuator side.
The selected push rod spherical joints provide limited deflections around their tilt and roll axes, while the pan axis is not affected by such restrictions. To maximize the camera orientation system workspace, this unsymmetrical working range is considered.

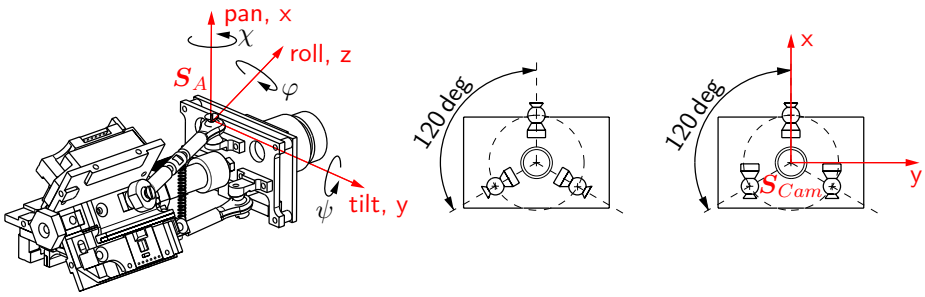

Figure 4.6.: CAD model of the camera orientation system (left); alignment of the spherical joints on the camera frame: initial (middle), optimized (right).

Figure 4.6 (left) reveals a CAD model of the developed camera orientation system. In the middle and on the right side of Figure 4.6 the initial and the optimized alignment of the spherical joints on the camera frame are presented. In both cases they are placed on a circle with 120 deg offset. In the initial configuration a star–shaped configuration is chosen. Figure 4.6 (right) presents the optimized arrangement of the joints. The spherical joints are placed vertically, such that the fixation screw lies in the camera's xz–plane. By doing so, the camera orientation system workspace is enlarged more than 10 %.

Once the joints and their arrangement are chosen, the workspace depends only on the kinematic parameters. For the camera orientation device we have defined three parameters, r_1, r_2, and d. The ends of the push rods are arranged on circles on the actuator base and on the camera frame. The radius of the circle on the actuator base is denoted with r_1 and r_2 on the camera frame. The minimum distance between the two circles is described by d, see Figure 4.7.

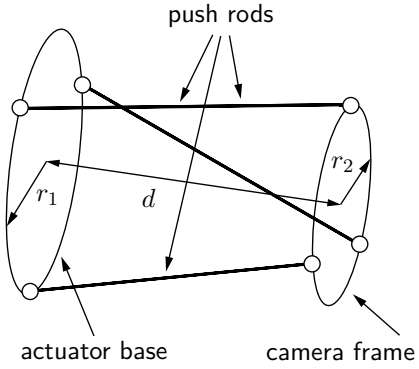

Figure 4.7.: Kinematic parameters in home position.

To determine the influence of the three chosen kinematic parameters, parameter variation studies are conducted. These studies revealed: i) The smaller the circles the spherical joints are arranged on, the larger the workspace. ii) The larger the distance between the two circles, the bigger the workspace.
The main objective of the optimization process is to yield a small overall size and contemporaneously a large workspace. In case i) both aims can be reached by reducing the two circles radii to a minimum. To guarantee a correct kinematics operation, collision between the single components must be avoided. Therefore, the developed CAD model is used to reduce the radii r_1 and r_2 as much as possible. In case ii) the two goals can not be fulfilled at the same time. The larger the distance between the two circles, the bigger the workspace, but also the bigger the overall size. To solve this contradiction we applied a numerical optimization, utilizing an implicit filtering algorithm *IFFCO*. The algorithm is based on a projected quasi–Newton iteration which uses difference gradients. For more information refer to [41]. To maximize the workspace/package dimension ratio the following objective function is chosen:

$$\min f(d) = \min \left(1 - \left(\frac{\mathrm{WS}(d)}{\mathrm{WS}_{max}} - \frac{d}{d_{max}} \right) \right). \tag{4.3}$$

During the optimization the distance d between the two circles is varied. For every length the reachable workspace $\mathrm{WS}(d)$ must be calculated. Thus, we gridded the maximum desired workspace WS_{max} with 0.1 deg steps, yielding a set of desired points. A cubic workspace volume with an edge length of ± 30 deg in all three axes is assumed. Afterwards, we checked whether the single points were within the reachable workspace using (A.54)–(A.58) and (A.69). Both values, length between the circles and reachable workspace, are normalized. The maximum allowed distance

between the two circles is described with d_{max} and is chosen to 165 mm. WS_{max} denotes the maximum desired cubic workspace. For the optimization an initial value of 100 mm was chosen for the distance d.
Possible collisions and the package dimensions of the single components are not regarded by the models used for the optimization process. Therefore, using the CAD model the final kinematic parameters are determined. They are denoted in Table 4.4.

Table 4.4.: Optimization Results.

Propriety	Value [mm]
Radius circle 1, r_1	17
Radius circle 2, r_2	13
Distance circles, d	40

The whole covered workspace is presented in Figure 4.8 (left). Due to the mechanical design and because of the joint limitations, the covered workspace is not a cuboid but a twisted sphere.

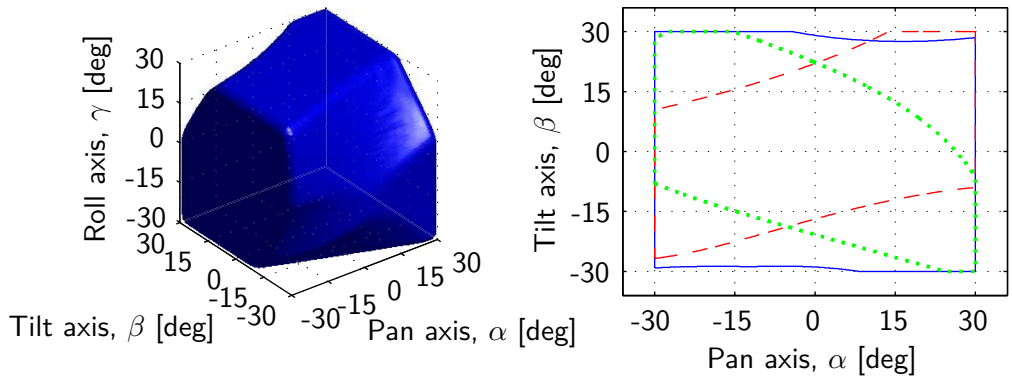

Figure 4.8.: Covered workspace: 3D (left), slices for neutral [—], maximum [– –], and minimum [· · ·] roll angle (right).

The achieved camera orientation device covers about 84 % of a cubic workspace volume with an edge length of ±30 deg for all three orientations. It is possible to fully cover a cubic workspace volume with about ±19 deg for all three orientations. If only one orientation is changed at a time and the other two are zero, a workspace of ±30 deg is covered in the pan and roll orientation, while in the tilt orientation a workspace of ±29 deg is provided. For a better overview the achievable pan and tilt angles are plotted on the right side of Figure 4.8 for three different roll orientations. If the roll angle is zero, nearly ±30 deg can be covered in both the pan and the tilt orientation. As the plot suggests, the smallest workspace is covered when the roll orientation is either at its maximum or minimum. The resulting system has an overall size of about $44 \times 44 \times 100\,\mathrm{mm}^3$.

Figure 4.9 indicates the color–coded maximum quantization error of all three axes over the entire workspace. Due to the nonlinear relation between the actuator positions and the camera orientation, the angular resolution is not constant over the workspace.

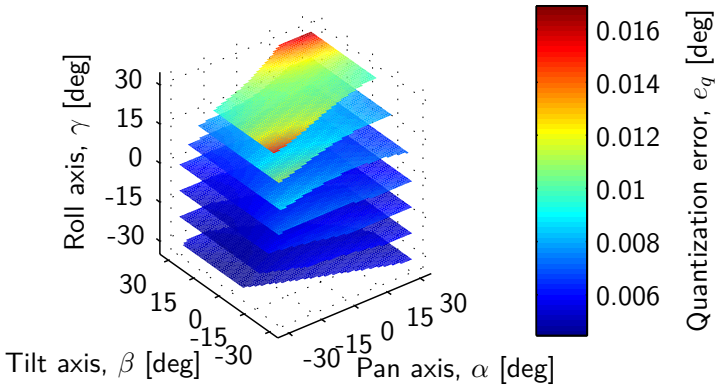

Figure 4.9.: Quantization error over the workspace.

The maximum quantization error of about 0.0169 deg occurs when the pan, tilt, and roll orientations are maximal. Normally a human does not keep his eye very long in such an uncomfortable position. To yield a more practical value, the mean quantization error over the entire workspace is calculated to 0.0067 deg. Thus, it can be confirmed that the developed camera orientation device provides a higher angular resolution then the human oculomotor system and can further cope with the required resolution of 0.02 deg.

4.5. Kinematic and Dynamic Simulations

As for the two DoF camera orientation systems, also for the three DoF system, kinematic as well as dynamic simulations are used to prove that the selected actuators are able to drive the device. As before, the kinematic model is developed and evaluated first. To yield access to the entire system dynamics a multi–body system is simulated in the second step.

4.5.1. Kinematic Simulations

To obtain a kinematic model, the nonlinear inverse kinematic solution (4.2) is differentiated with respect to time.

$$\dot{\boldsymbol{q}} = \boldsymbol{J}^{-1}(\boldsymbol{w})\,\dot{\boldsymbol{w}}. \tag{4.4}$$

Using this linear projection, the required actuator velocities $\dot{\boldsymbol{q}}$ can be calculated over the entire workspace by given angular velocities $\dot{\boldsymbol{w}}$. $\boldsymbol{J}^{-1}(\boldsymbol{w})$ describes the inverse

Jacobian. The developed camera orientation system is free of singularities over the entire workspace. Thus, the inverse Jacobian calculation is straightforward:

$$\boldsymbol{J}^{-1}(\boldsymbol{w}) = \frac{\partial \boldsymbol{q}}{\partial \boldsymbol{w}} = \frac{\partial \boldsymbol{g}(\boldsymbol{w})}{\partial \boldsymbol{w}}, \tag{4.5}$$

where the inverse kinematics is denoted with $\boldsymbol{g}$, the orientation angles with $\boldsymbol{w}$, and the linear actuator positions with $\boldsymbol{q}$.
To prove that the selected piezo–actuators are able to cope with the required velocities, the most ambitious case is chosen: constant velocities of 500 deg/s around all three axes. Evaluating (4.4), required velocities for the single actuators are calculated. To prove the actuators' suitability, only the maximum velocities needed of all actuators must be evaluated, which is introduced in Figure 4.10.

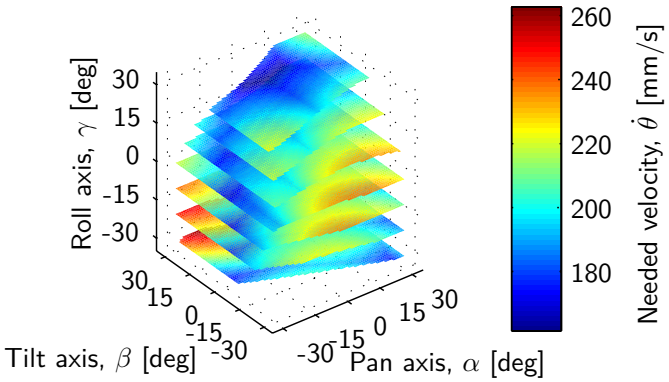

Figure 4.10.: Kinematic simulation results with constant velocities of 500 deg/s around all three axes.

The plot illustrates that actuator velocities of up to 260 mm/s are required. According to the data sheet the actuators are able to provide velocities of up to 600 mm/s [81].

4.5.2. Dynamic Simulations

To confirm that the selected actuators meet the requirements besides the velocities needed, also the accelerations and forces needed must be estimated. As reported in the previous section the required velocities can be calculated with a kinematic model. To gain the needed accelerations and forces a dynamic model is required. Such a model accounts for the inertial masses, the friction in the joints, and for the influence of the tension springs.
For the dynamic model setup the multi–body simulation tool *MBSim* is used. We modeled the developed camera orientation system as a rigid body model since elastic deformation during motion is small and therefore negligible. After an appropriate model parameterization, the Newton–Euler equations are generated and evaluated by the used simulation tool.

To parameterize the dynamic model the inertia matrices of the single parts are derived from the CAD model. The mass of the movable parts is introduced in Table 4.5.

Table 4.5.: Mass movable parts.

Part	Mass [g]
Camera	16
Push rod	3
Prismatic joint	5
Spring	< 0.1

Hereby the mass denoted with *Camera* includes the camera, the camera mounting frame and the main spherical joint. *Push rod* implies the push rod itself and the two attached spherical joints. The movable part of the prismatic joints, the linear encoder stripes, and the mounting frame for the encoder stripes are described with *Prismatic joint*. Finally, *Spring* denotes the selected tension springs mass. Because the mass of the latter is very small, it is neglected for the simulation. Since the system is driven by three actuators the inertial mass of the *Push rods* and the *Prismatic joints* must be considered three times in the dynamic model.
In Table 4.6 parameters of the selected springs are listed.

Table 4.6.: Tension springs.

Parameter	Value
m_{TS}	$< 0.1\,\mathrm{g}$
$l_{0_{TS}}$	$16\,\mathrm{mm}$
c_{TS}	$55\,\mathrm{N/m}$

Hereby, the spring mass is denoted by m_{TS}. $l_{0_{TS}}$ describes the unloaded spring length and c_{TS} the spring stiffness.

In the following the friction produced in the joints is calculated. Afterwards we decide whether the friction must be taken into account in the dynamic model.
First, the influence of the spherical joints is calculated with the following equation:

$$M_{F_{SJ}} \leq C_\alpha \frac{F\, r_{SJ}\, \mu_{SJ}}{\sqrt{1+\mu_{SJ}^2}}. \tag{4.6}$$

Thereby, the frictional torque is denoted with $M_{F_{SJ}}$. While C_α is a weighting factor, the external applied force to the joint is described by F. The ball radius is denoted with r_{SJ} and μ_{SJ} depicts the friction coefficient between the ball and the joint socket. For more information regarding (4.6) and its parameters refer to [37].

As mentioned before we used different kinds of spherical joints: the main spherical joint and the push rod attached spherical joints. For all the frictional torque is calculated evaluating (4.7). In Table 4.7 the parameters for the estimation of the friction in the main spherical joint are presented.

Table 4.7.: Frictional torque: main spherical joint.

Parameter	Value
C_α	1.0
F_{MSJmax}	0.87 N
r_{MSJ}	2.5 mm
μ_{MSJ}	0.08

The parameter C_α was chosen to be equal to one, see [37]. F_{MSJmax} denotes the maximum applied force to the main spherical joint. Conducting dynamic simulations, the force was estimated. As expected the maximum value arises when the camera is oriented around all three orientations simultaneously with the maximum velocity. The frictional coefficient between the steel ball and the plastic joint socket is described by μ_{MSJ}. The maximum friction torque of the main spherical joint was estimated to $M_{F_{MSJ}} = 0.173 \cdot 10^{-3}$ Nm. We calculated that the driving torque needed for the main spherical joint reached up to $8.1 \cdot 10^{-3}$ Nm. With respect to the driving torque the small frictional torque can be neglected.
The friction in the spherical joints, attached to the push rods, is calculated in the same way as the friction in the main spherical joint. The parameters for the estimation are listed in Table 4.8.

Table 4.8.: Frictional torque: push rod spherical joint.

Parameter	Value
C_α	1.0
$F_{PRSJmax}$	0.65 N
r_{PRSJ}	2.375 mm
μ_{PRSJ}	0.15

μ_{PRSJ} describes the worst frictional coefficient of both types of spherical joints used to setup the push rods. The maximum frictional torque was calculated to $M_{F_{PRSJ}} = 0.229 \cdot 10^{-3}$ Nm for each of the six joints. We assumed that each piezo–actuator must compensate the friction of two spherical joints. The distance between the point of application of the actuator force and the spherical joints center is 8 mm yielding to a frictional force of 0.057 N. Compared to the driving force, the frictional force is quite small and can be neglected.
Each piezo–actuator transmits its force over a small pusher to the free direction of a prismatic joint. To estimate the induced friction the joint is modeled as a mass–damper element, see Figure 4.11.

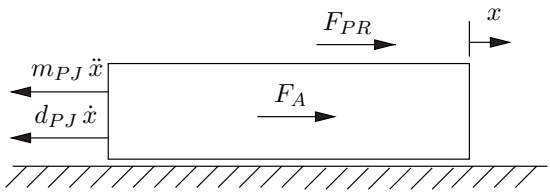

Figure 4.11.: Mass–damper model of the prismatic joint.

Such a system can be described as follows:

$$m_{PJ}\,\ddot{x} = F_A - d_{PJ}\,\dot{x} + F_{PR}, \tag{4.7}$$

where the mass and the damping coefficient of the prismatic joint are denoted with m_{PJ} and with d_{PJ} respectively. The joint velocity and the acceleration are described by $\dot{x}$ and $\ddot{x}$. F_A corresponds to the force required from the actuators to drive the camera orientation system. Finally, the force included in the push rods is denoted by F_{PR}.
We evaluated (4.7) to calculate the required actuator force, considering the prismatic joints influence. Table 4.9 illustrates the parameters used for the simulation.

Table 4.9.: Frictional force: prismatic joints.

Parameter	Value
m_{PJ}	5 g
d_{PJ}	1.5 Ns/m

m_{PJ} accounts for the prismatic joints and for the custom made moving parts. This mass is obtained from the CAD model and from the data sheet, respectively. Alike the damping coefficient d_{PJ} was taken from the data sheet. The conducted simulations confirmed that the frictional force in the prismatic joint plays an important role and is therefore taken into account in the dynamic simulation model.
To summarize, we developed and parameterized a dynamic simulation model using *MBSim*. This model accounts for the inertial masses of the single components and for the influence of the tension springs. We also estimated the friction in the different joints. These calculations demonstrate that the frictional influence of the spherical joints is negligible. However, the friction in the prismatic joint is quite large and consequently taken into account.

We carried out different simulations with the implemented dynamic model. Since saccadic eye movements pose the strongest requirements to the system, further investigations concentrate on this motion pattern. Simulations demonstrate, the bigger the simulated saccades and the more DoF involved, the higher the requirements posed to the actuators. For that reason we present simulations where all three DoF change simultaneously over the entire reachable workspace of ± 19 deg. We use sinusoidal angle changes to imitate the human eyes' acceleration and deceleration

phases, see Figure 4.12 (left). In Figure 4.12 (middle) the required angular velocities are indicated. They exceed 800 deg/s. Finally, in Figure 4.12 (right) the calculated angular accelerations are presented. The peak value of the simulated saccades reach about 25000 deg/s^2.

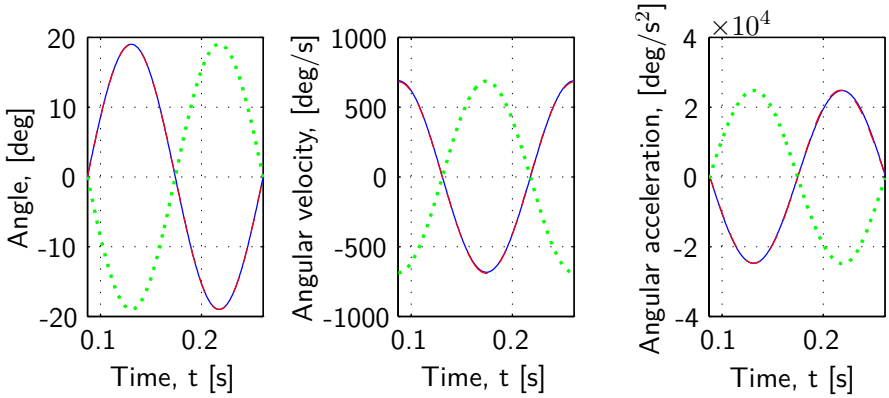

Figure 4.12.: Desired angles, angle velocities, and angle accelerations around the pan [—], tilt [– –], and roll [· · ·] axis.

The pan and the tilt movements can not be distinguished in Figure 4.12 because the graphs are superposed. The roll angle changes with a negative amplitude with respect to the other two orientations. Due to the mechanical design, the actuators must cope with longer travel ranges to fulfill this pattern, compared to one where all angles have the same amplitude.
The required linear actuator positions, velocities, and accelerations are calculated with the dynamical model using the introduced camera orientation changes. The results are presented in Figure 4.13.

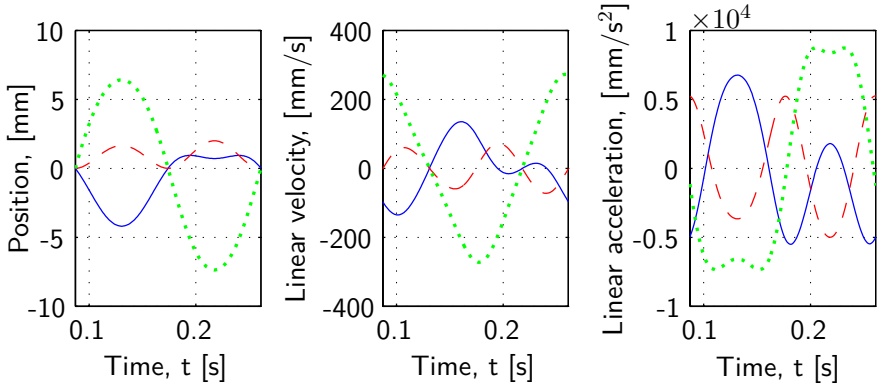

Figure 4.13.: Desired positions, linear velocities, and linear accelerations of actuator one [—], two [– –], and three [· · ·].

Figure 4.13 reveals that the requirements posed to the third actuator are the strongest. Maximum velocities of up to 270 mm/s (see Figure 4.13 (middle)) and maximum

accelerations of up to 8740 mm/s^2 (see Figure 4.13 (right)) are required. According to the data sheet [81] both, the velocities and the accelerations, can be supplied by the selected actuators.
On the left side of Figure 4.14 the calculated actuator forces are introduced. Compared to the remaining two actuators, the third actuator must fulfill longer travel ranges in the same time period, see Figure 4.13 (left). Thus, higher accelerations are necessary, which yield to the highest force changes. However, the maximum absolute force of about 0.7 N must be supplied by the first actuator. The simulation results reveal further that only negative forces must be provided by the piezo–actuators. As stated, to avoid backlash we connected the single push rods with each other using tension springs. Thus, the push rods are tightening together and the camera tends to rotate clockwise around the longitudinal axis. To inhibit this rotation a negative force must be applied by the actuators.

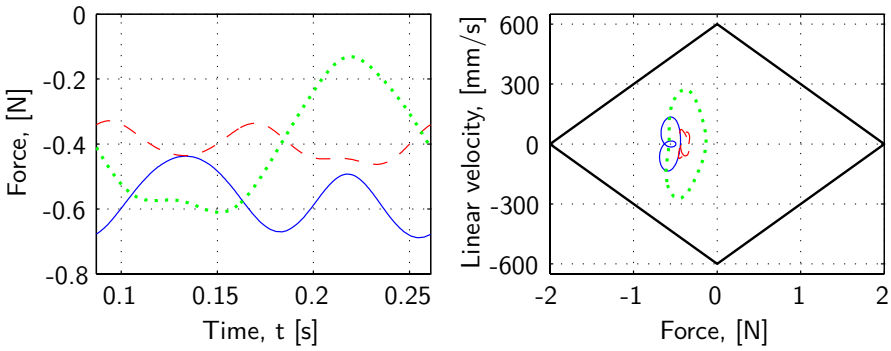

Figure 4.14.: Desired forces (left), force/velocity diagram (right) of actuator one [—], two [– –], and three [· · ·].

On the right side of Figure 4.14 a force/velocity diagram is presented. Here the outer rhomb (bold line) indicates the piezo–actuator limits according to the data sheet. Inside this rhomb three graphs are presented which introduce the requirements posed to the actuators. The simulation results reveal that the required actuator output capabilities are smaller than the maximum achievable ones.

Based on these simulations and the information obtained from the data sheet we can confirm that the selected piezo–actuators are able to drive the camera orientation system with the high dynamic motion patterns needed. Model inaccuracies and the negative influence of the signal cable for the camera are neglected in the considerations presented. However, the actuators' power reserve is high enough to deal with these deviations, see Chapter 5. To simulate the most ambitious case, saccades with an amplitude of 38 deg were assumed. Since more than 90 % of the human saccadic eye movements are within 20 deg, see [19], real saccades are typically less challenging than the simulated ones.

4.6. Device Setup

We set up a prototype using the information yield from the simulations and the optimization process. The so developed camera orientation device is introduced in Figure 4.15.

Figure 4.15.: Camera orientation system with three DoF.

Aluminum alloy (*AlZn5.5MgCu*) is used to fabricate most of the custom made parts. The push rods are manufactured out of a high alloy chrome–nickel steel (1.4305) which guaranties a higher grade of stiffness. The camera orientation system has a size of about $44 \times 44 \times 100\,\mathrm{mm}^3$ including the used *Point Grey Firefly MV* camera and an approximate weight of 100 g (without wiring). The movable parts mass, including the 11 g of the camera, is about 40 g. About 84 % of a cubic workspace volume with ± 30 deg for all three orientations is covered. As will be presented in Chapter 5, angular velocities of more than 1000 deg/s can be reached. The camera orientation is calculated from the measured linear actuator positions using the nonlinear kinematic relations. Thus, the angular resolution is not constant over the entire workspace. The maximum quantization error is about 0.0169 deg. Table 4.10 summarizes the main parameters of the developed camera orientation system.

4.7. Discussion

A three DoF camera orientation system has been introduced, optimized, and verified. Due to the planned applications as part of a gaze–driven head–mounted camera system or as an artificial eye for humanoid robots, the camera orientation device must cope with the high dynamic properties of the human oculomotor system. Thus, a compact and lightweight design is important. Besides a supplementary DoF also a higher angular resolution compared to the system with two DoF is required while the needs to the workspace are reduced. Our suggested approach is based on a piezo–actuator driven parallel kinematics which orients a camera around the pan, tilt, and roll axis. Considering the joint limitations the inverse kinematics was ascertained

Table 4.10.: Specifications of the camera orientation system with three DoF.

Propriety	Value
Covered workspace	84 % of a cubic Volume with ± 30 deg
	100 % of a cubic Volume with ± 19 deg
Angular velocities	> 1000 deg/s
Maximum quantization error	0.0169 deg
Mean quantization error	0.0067 deg
Overall size*	$44 \times 44 \times 100\,\mathrm{mm}^3$
Push rod length	42.86 mm
Actuator travel range	± 11 mm
Overall mass*	100 g
Mass movable parts*	40 g

* The presented values do not account for cabling.

and the workspace was calculated. Applying an implicit filtering algorithm onto the kinematic model, the workspace/package dimensions ratio was maximized. About 84 % of a cubic workspace volume with ± 30 deg for all three orientations is covered with a camera orientation device with a size of $44 \times 44 \times 100\,\mathrm{mm}^3$. It is possible to fully cover a cubic workspace volume with about ± 19 deg for all three orientations. While the moving parts of the system have a weight of about 40 g, the overall weight is about 100 g (excluding wiring). To reduce the size and the weight, compared to the camera orientation systems with two DoF, a new sensor system was chosen, which allowed placement of the push rod nearer to the center. The maximum quantization error of the camera orientation system with three DoF was calculated to be less than 0.017 deg, while the mean quantization error is about 0.0067 deg. Thus, the developed device provides a higher angular resolution than the human oculomotor system and can further cope with the required resolution of 0.02 deg. Besides a kinematic, also a dynamic simulation model was developed. Investigations carried out with them revealed that the selected piezo–actuators are able to cope even with the most challenging eye movements, the saccades. Closed–loop control experiments confirmed the simulation results.

5. Control Architectures

To allow a continuous alignment of a camera with the human line of sight, besides compact camera orientation systems also appropriate control structures are required. While the mechanical development is described in the last two chapters, this chapter deals with the control design. The controllers must ensure a high speed camera orienting with small overshoot and smooth trajectory pursuit. For acquiring stabilized images without supplementary post–processing, the latencies of the overall system must be kept small. Thus, the frequency response of the controlled mechatronic system must outreach the human eye capabilities. Furthermore, a low noise level of the controlled system is important for keeping the influence on users low.
In the first section of this chapter the selected piezo–actuators as well as the power electronics needed are introduced and their driving principle is explained. Subsequently, different linear and nonlinear control architectures are discussed. We distinguish two control classes: joint space controllers and workspace controllers. In case of the joint space controllers the desired camera orientation is transformed to linear actuator set points. These positions are then adjusted with closed–loop controllers. The thereby underlying concepts are introduced in Section 5.2. In the second group of investigated control architectures the camera orientation (and not the linear actuator position) is adjusted directly by closed–loop controllers. Therefore, this principle is declared as workspace controller. The examined approaches are described in Section 5.3, where also a state space decoupling controller according to Falb and Wolovich is introduced. Using a simplified mechanic model, the equation of motion are ascertained and validated with a dynamic simulation model which accounts for the entire manipulator. To compare the control approaches with each other, step response and following behavior experiments were performed. Based on these results the most suitable controller is selected and additional experiments, concerning the overall head–mounted gaze–driven camera system as well as the image quality were conducted, see Section 5.4. Finally, a discussion summarizes the results, see Section 5.5.

5.1. Actuator System

In this section the selected actuator system is presented. Therefore, the driving principle and the characteristics of the used power electronics are described. Furthermore, we propose methods to deal with the actuator dead zone.

5.1.1. Driving Principle

To drive the camera orientation devices ultrasonic piezo–actuators P–661 from *Physik Instrumente* [81] were chosen. This actuator consists basically of two single piezo–elements connected with each other. In the middle of them a small pusher is situated. This pusher is pressed against a friction bar which is fixed on a prismatic joint, see Figure 5.1 (left).

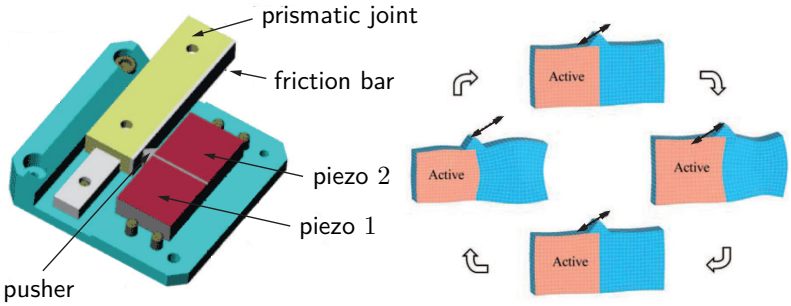

Figure 5.1.: Ultrasonic piezo–actuator: structure (left), periodical piezo–elements oscillations (right), modified from [118].

By applying a sinusoidal voltage to one of the two piezo–elements a two dimensional standing wave is generated. Due to the indirect piezoelectric effect the active element is contracted and expanded, respectively. Because of the mechanical coupling also the passive element is excited. The result is an asymmetric oscillation of the pusher, see Figure 5.1 (right). The small pusher movements are transmitted to the prismatic joint via the friction bar. Thus, the travel range of such actuators is, theoretically, limited only by the used prismatic joint. To invert the actuators moving direction the passive piezo–element must be driven. For more detailed information about the operating principle of piezo–actuators refer to [118].

5.1.2. Power Electronics

Special power electronics are required to drive the piezo–actuators. To yield high efficiency they are operated at resonance frequency. By varying the applied voltage amplitude the actuator velocity is changed. *Physik Instrumente* provides two different types of drivers: C–180 [80] and C–184 [83].
The C–180 adjusts the voltage using PWM. According to the manufacturer the maximum PWM frequency is 300 Hz. This results in two major drawbacks: first a supplementary time delay of 3.3 ms is introduced, second an acoustic noise is produced by the actuators. By overclocking the power electronics both the time delay and the acoustic noise can be reduced. However, the noise level remains high. According to the manufacturer the C–184 adjusts the voltage continuously. Therefore, no acoustic noise is produced. Compared to the C–180 the C–184 provides more

adjustment possibilities. Thus, better control results can be achieved with the drawback of a larger package dimension. Due to the reduced noise and the enhanced control quality C–184 is selected.

In Figure 5.2 the voltage applied to the two piezo–elements is illustrated, while the actuator performs movements with the maximum velocity in negative direction. Sinusoidal voltage signals with an amplitude of about 70 V and a frequency of about 210 kHz are applied to the second piezo–element.

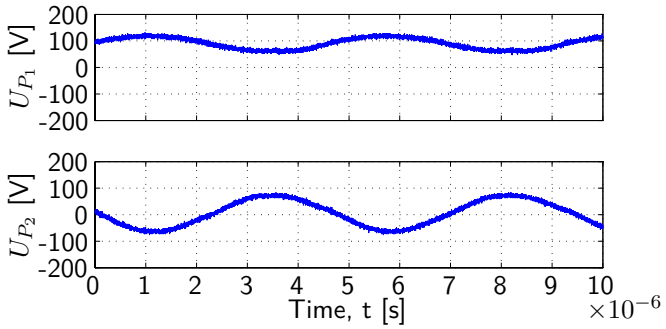

Figure 5.2.: Piezo–element voltage while performing movements with maximum negative velocity: U_{P_1} passive, U_{P_2} active.

Due to the mechanical coupling of the piezo–elements and due to the direct piezoelectric effect, the piezo–element P_1 produces sinusoidal voltages with the same frequency but a smaller amplitude. The piezo–element is a capacitor and able to store energy. Therefore, a positive offset is registered in the first voltage signal U_{P_1}. Measurements have reported that the resulting offset voltage is always positive. The noise indicated in the plots occurs due to quantization of the measured signal.
We further investigated the dynamic characteristics of the power electronics. Different step input signals are applied, while the output behavior is observed. These measurements revealed that the system is nonlinear. If the step size increases a longer time period is required to reach the new output signal. Moreover, we have observed that the delay depends also on the sign of the input signal. If this signal changes from a positive to a negative one, the new output signal can be reached about ten times faster compared to signal changes in the opposite direction. A possible explanation for this behavior can be found in the fact that a positive energy is always stored in the passive piezo–element. The power electronics is not able to deal with this energy in both directions identically. In Figure 5.3 the worst case is plotted, were the input signal U_{In} changes from maximum negative to the maximum positive value. The noise in the plots arises due to the high piezo–actuators driving frequency (210 kHz).

The voltages applied to the piezo–elements reach the new desired values in about 0.7 ms. Since most of the control architectures are running with a sampling frequency of 1 kHz, the new desired piezo–actuator signals are provided in less than one time period. Thus, the nonlinear behavior of the used power electronics is neglected.

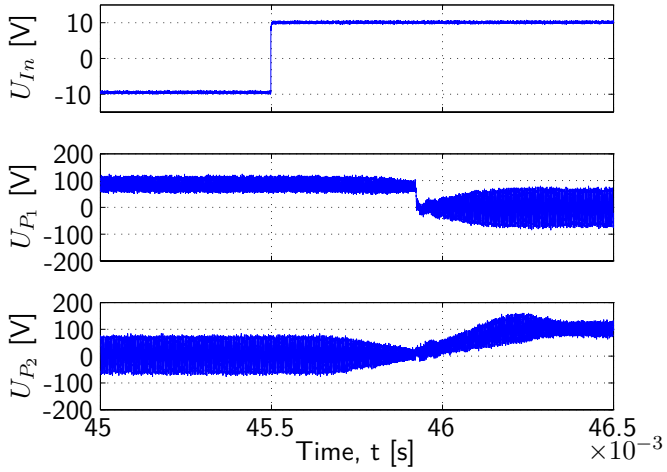

Figure 5.3.: Dynamic behavior of the piezo–element voltage during input signal changes.

5.1.3. Dead Zone Compensation

Preliminary control experiments with the actuator system indicated that for small input signals no piezo–actuators movements can be registered. This phenomenon, which can be described as a dead zone, has two major reasons. The first is the static friction of the mechanical setup. The second is the adjustment of the power electronics itself. Potentiometers can influence the characteristic response of the actuators, so that movements also occur for small input signals. Because of the high bandwidth of the piezo–actuators, an acoustic noise will be generated in this case. Since the developed camera orientation system is intended to be head–mounted, users should be affected as little as possible. Therefore, the dead zone is enlarged artificially.

For the following investigations a simplified actuator model, illustrated in Figure 5.4, is used. The dead zone arising between the power electronics input signal I_S and the actuator forces F_A is indicated by $\mathcal{NL}$. The actuator forces are transmitted to a prismatic joint, which is modeled as a mass–damper system (see Section 3.5 and Section 4.5). To cope with the dead zone, we estimated the nonlinearity and applied the inverse function $\mathcal{NL}^{-1}$ to the actuator system.

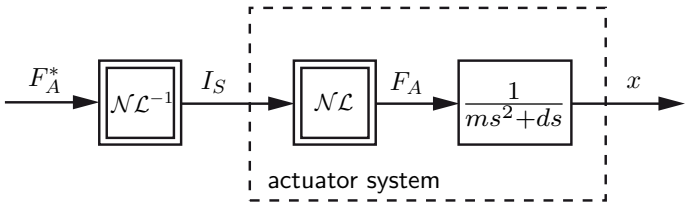

Figure 5.4.: Simplified actuator model.

Two different approaches have been investigated. Velocity and (static) force measurements are performed with the actuators. First, a neuronal network is trained off–line to fit these characteristic curves, yielding suitable initial values. After that,

the basic data gained is refined and adapted during measurements to other actuators while training the neuronal network on–line. In this way, the data validity is improved and the amount of measurements necessary is reduced. The approach has been described in detail in [2].
The nonlinear behavior between the power electronic input signal and force produced by the actuators is also rudimentarily described in the piezo–actuators data sheet, see [81] and [82]. The few data provided by the manufacturer is matched with the following quadratic equation:

$$F_A = k_F \, I_S^2 \, sgn(I_S), \tag{5.1}$$

where F_A represents the force produced by the actuator, k_F is the motor constant chosen to be 2.5 N, and I_S depicts the input signal.

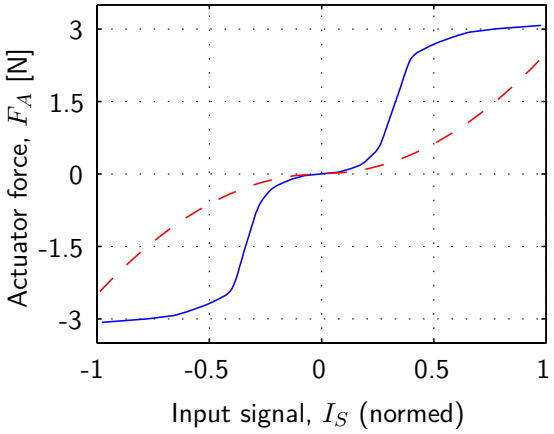

Figure 5.5.: Relation between input signal and produced force: adapted [—] and quadratic approach [– –].

As Figure 5.5 shows, the graph obtained with the quadratic equation differs from the real measurements. It can be further observed that similar results are gained with both descriptions for small input signals. In this area (the dead zone) no forces or movements are produced by the actuator. We therefore inverted both functions and used them to compensate the dead zone as illustrated in Figure 5.4.
To compare the two approaches the following measurements were performed with a simple closed–loop proportional controller. Without an integral part in the controller, the system is very sensitive to inaccuracies in the compensation function. To exclude any influence from the parallel kinematics or from the other actuators, the tested actuator was examined without any connection to the camera orientation system.
As expected, better control results can be achieved with the adapted compensation that is based on measurements and the neuronal network. However, considerable acoustic noise is produced by the advanced compensation. Hence, control gains have been manually reduced to minimize acoustic noise. In Figure 5.6 the position control

errors for the different compensations are shown for sinusoidal actuator movements with an amplitude of 10 mm and a frequency of 0.5 Hz.

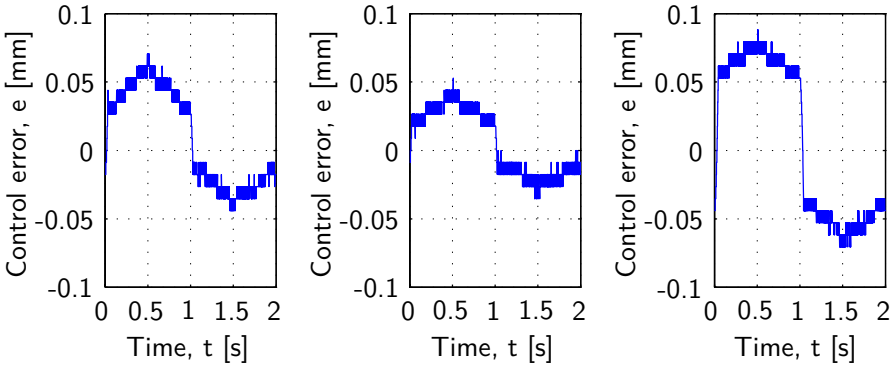

Figure 5.6.: Control error: adapted compensation (left), quadratic compensation (middle), without compensation (right).

Less noise was produced when reducing the control gains. This, however, led to inferior control results of the adapted compensation compared to the quadratic compensation (see Figure 5.6 left and middle). Furthermore, measurements with no compensation at all were performed. The noise was reduced a little at the cost of an increasing control error, see Figure 5.6 (right).
Thus, the quadratic approach offers the best tradeoff between acoustic noise and nonlinear dead zone compensation. To deal with the inaccuracies, an integral part is added to the closed–loop controller, which notably improves the control results. Subjective examinations revealed that the integral controller increases the acoustic noise only slightly.

5.2. Joint Space Controller

Because of the simple design joint space controllers are implemented first. Thereby set points for the linear actuators are calculated from the desired camera orientation. These positions are then adjusted with different controllers. The advantage of this approach is that the start up of the single actuator controllers can be done independently from each other. Once the control parameters are adjusted, the entire system is started and the parameters are refined.
The joint space and workspace architectures introduced are implemented using *Matlab/Simulink Real Time Workshop* from *The MathWorks* on a rapid prototyping real time processing board *DS 1103 PPC* from *dSPACE*. In addition, a user interface and a data acquisition tool are developed based on this rapid prototyping environment.

5.2.1. PID–Controller

For the first experiments, we integrated a proportional–integral–differential (PID) closed–loop controller to adjust the set points for the linear actuators. In Figure 5.7 the joint space PID control architecture is illustrated for the two DoF camera orientation systems.

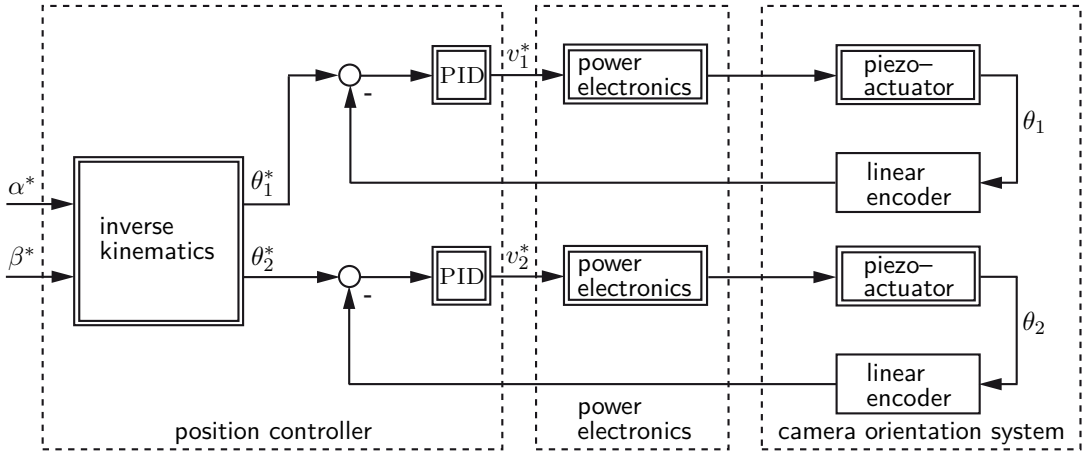

Figure 5.7.: Joint space PID controller architecture for the two DoF camera orientation systems.

Using the inverse kinematic solution, see Section A.1.1, the desired orientation angles (α^* and β^*) are transformed to the desired position values (θ_1^* and θ_2^*). The linear actuator positions (θ_1 and θ_2) are measured directly with two optical linear encoders. From the difference between desired and measured positions, required velocities (v_1^* and v_2^*) are calculated using two PID controllers and routed to the power electronics. These devices include the power stages that are required to convert the input signals to the respective piezo–actuator control signals. Both PID controllers are equipped with an integral anti–windup to avoid possible overshoots, see [95]. Since short response times are required in case of fast set point changes, a differential controller part is needed. This, however, will lead to acoustic noise, especially during slow phases where a large amount of small actuation movements are fulfilled. To affect users as little as possible, the differential part of the controller is activated only during large movements.

In Section 2.1 the most important human eye movements are introduced. They must be reproduced by the mechatronic systems. Therefore, in the following experiments with i) square pulses (step response), to simulate human eye saccades, and ii) sinusoidal movements, to simulate human eye smooth pursuit, are carried out. To cover nearly the entire workspace the orientation changes within a range of $\pm 20\,\text{deg}$.

To evaluate the selected architecture, the orientation accuracy is also important. Thus, results are presented in workspace coordinates. The camera orientation is calculated from the measured actuator positions via the direct kinematic solution introduced in Section A.1.3. Here, only worst case measurements with the highest

control errors are presented. In the experiments, the mono camera orientation system was used. With the stereo camera system similar results were obtained. They are reported in Section C.2.
Figure 5.8 illustrates the system response for a step command from -20 deg to 20 deg in the pan direction while the tilt angle is set to zero.

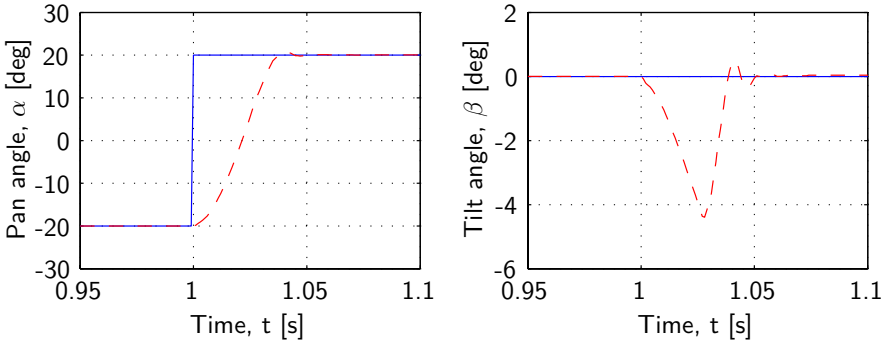

Figure 5.8.: Desired [—] and measured [– –] orientation during step response, PID joint space controller.

Figure 5.8 (left) suggests that the new desired pan orientation can be reached in less then 40 ms, which yields an average angular velocity of over 1000 deg/s. Only a small overshoot of about 1 % is measured. Figure 5.8 (right) confirms that an angular error in the tilt orientation of less than 5 deg occurs. The tilt deviation is limited to the same small time gap in which the pan orientation changes. This measurement illustrates, that an orientation error occurs not only in the pan axis, where orientation changes are applied, but also in the tilt axis. The investigated approach implies that both actuators must move simultaneously and with the same response characteristics. Due to the remaining discrepancy between the two actuators, an orientation error will occur especially when the piezo–actuators are in saturation. Furthermore, we conducted experiments where the maximum angular velocity is limited. By doing so, the periods where the actuators are in saturation are reduced and the control quality is enhanced. If a simple linear filter would be used to restrict the maximum velocity, every signal would be filtered and an undesirable supplementary dead time would be introduced. Therefore, a so–called rate limiter, which is active for high dynamic signal changes only, is used.
Figure 5.9 reveals the system response for a step input of ±20 deg pan angle and zero tilt orientation. A new desired pan orientation can be reached in about 51 ms, which yields an average angular velocity of nearly 800 deg/s. An overshoot by about 4.5 % can be observed. Figure 5.9 (right) indicates that the orientation error in the tilt direction is reduced of about the factor four to 1.35 deg. The measurements reveal that by limiting the time period where the actuators are in saturation, the control error can be reduced. However, compared to a system without rate limiter the maximum achievable velocity is limited and the settling time is increased.
Besides the different actuator characteristics the mechanical coupling between the two actuators represents a possible source for the error in the tilt orientation. Due to the parallel kinematics, forces applied by one actuator must be supported by the

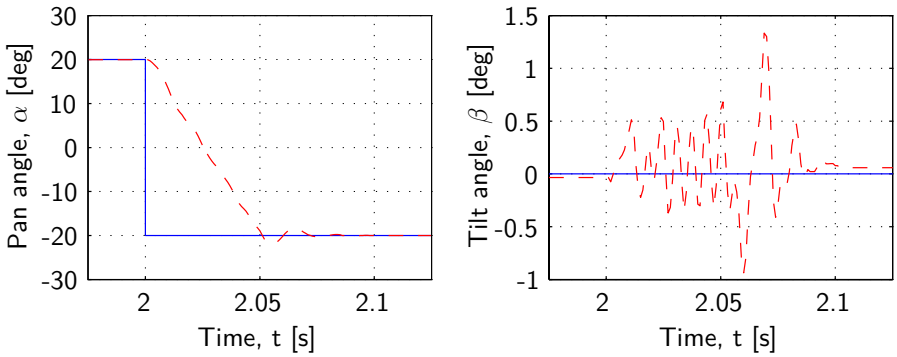

Figure 5.9.: Desired [—] and measured [– –] orientation during step response, PID joint space controller, angular velocities limited to 800 deg/s.

other. Therefore, it can occur that one actuator is forced in the wrong direction by the other. This mechanic coupling is not considered in the control architecture. The additional force is handled as a disturbance and is compensated by the controller integral part.
In Figure 5.10 the error in angular position is illustrated, while the pan axis is subject to sinusoidal movements with an amplitude of 20 deg and a frequency of 0.5 Hz and the tilt axis is held to zero. In the plots, quantization noise, arising from the limited encoder resolution, is illustrated.

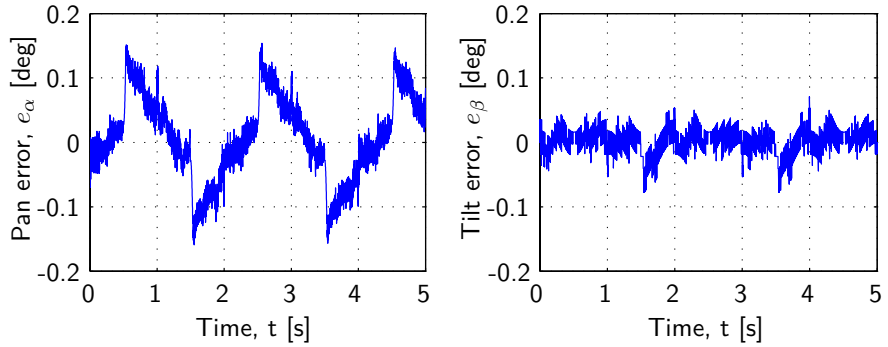

Figure 5.10.: Angular error during sinusoidal movements, PID joint space controller.

The figure suggests that the orientation error remains below 0.15 deg for the pan and 0.08 deg for the tilt orientation. Orientation errors of both axes are smaller than the human extreme gaze fixation accuracy of 0.16 deg [14]. In Figure 5.10 (left) steps can be observed. They occur with a period of 1.0 Hz and an offset of 0.5 s. The steps in the error signal occur when the direction of rotation of the simulated eye movements changes. At these points the actuators are idling. Before the motion restarts, the static friction of the used prismatic joints must be overcome. During this time period the positioning error increases rapidly. To restrict the maximum allowed angular velocity a rate limiter is used, which is active for high dynamic signals only. Therefore, the measurements conducted with slow orientation changes are not influenced.

The experimental results presented were yielded without a special actuator dead zone compensation. The integral controller part was able to compensate for the nonlinearities, thus in experiments using the quadratic compensation no improvements could be observed.

Due to the positive experience the joint space controller is also applied to the three DoF camera orientation system. The implemented structure is introduced in Figure 5.11.

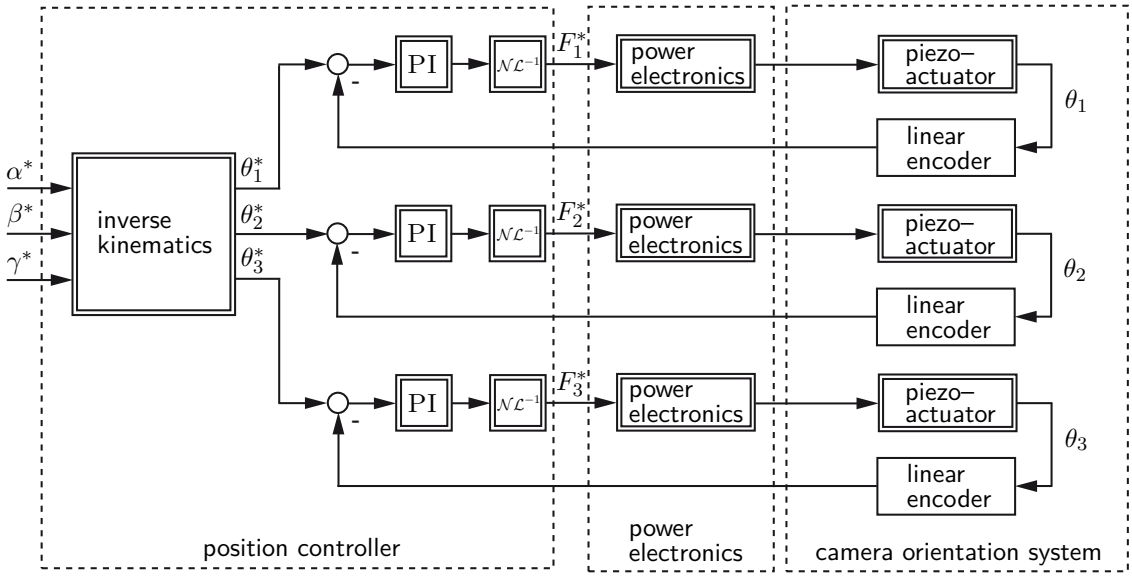

Figure 5.11.: Joint space PI controller architecture for the three DoF camera orientation system.

As for the system with two DoF, the desired camera orientation angles are transformed to set points for the linear actuators using the inverse kinematic solution. The positions of the linear actuators are measured with magnetic encoders. The desired values are adjusted with three separated proportional–integral (PI) controllers. First experiments indicated that in contrast to the two DoF system, in the three DoF system the actuator nonlinearities can not be compensated by the controllers. Due to the mechanical design the orientation of the system is more sensitive to position inaccuracies than two DoF systems. Therefore, we used the quadratic compensation, see Section 5.1.3, to deal with the piezo–actuator dead zone. After applying the compensation, the desired forces (F_1^*, F_2^*, and F_3^*) are passed to the power electronics. The PI controllers are equipped with an integral anti–windup and a rate limiter is used to artificially restrict the camera velocity.
Figure 5.12 reveals the camera orientation behavior when a step in the tilt direction from -20 deg to 20 deg is applied and the pan and roll orientations are set to zero. Figure 5.12 (middle) indicates that new orientation can be reached in about 40 ms, which results in an average angular velocity of about 1000 deg/s, with only a small overshooting of about 1 %. An angular orientation error in the pan axis of less than 0.7 deg and in the roll axis of about 2.1 deg can be observed. These

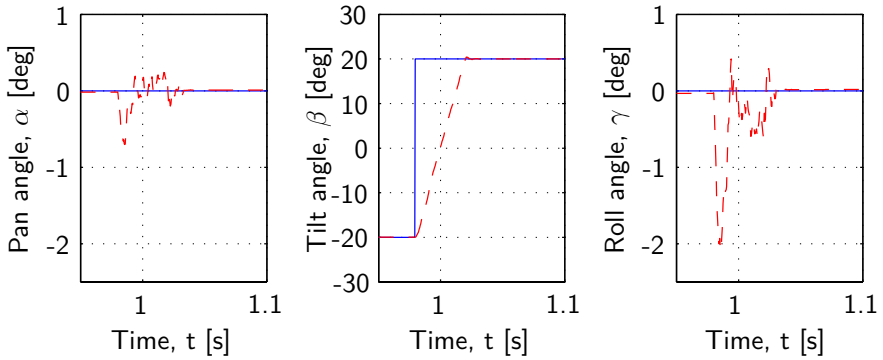

Figure 5.12.: Desired [—] and measured [– –] orientation during step response, PI joint space controller, three DoF camera orientation system.

errors occur because of the kinematics parallel structure. Position errors that arise during displacement of at least one of the linear axes always result in angular errors of all orientations. Due to the kinematical structure, the roll orientation is the most sensitive one, and its error is larger than the error in the pan axis. As stated before, the maximum achievable velocity is artificially limited to 1000 deg/s by the controller. That way, the required angular velocities of 500 deg/s can be provided and the angular error in the non–tilted axes is reduced. Experiments without this limitation reveal that it is possible to fulfill steps of 40 deg in less then 15 ms in roll orientation. Thus, it is possible to reach an average velocity of more than 2500 deg/s with this camera orientation system.
Further experiments simulated slow human eye orientation changes, so–called smooth pursuit. The movements were executed for the roll axis, the other two axes were kept at zero.

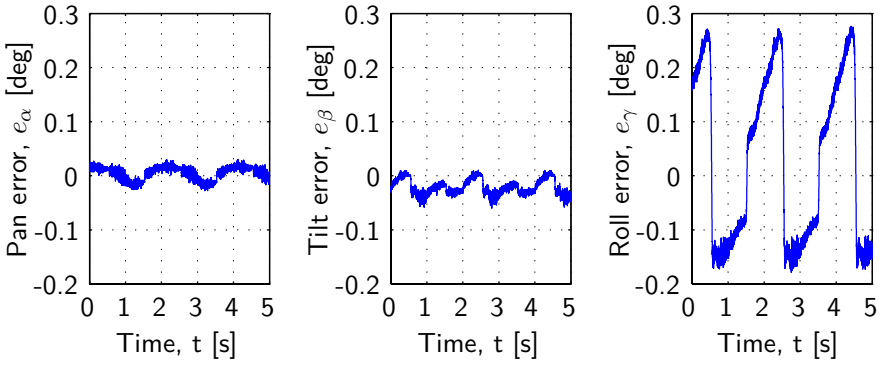

Figure 5.13.: Angular error during sinusoidal movements, PI joint space controller, three DoF camera orientation system.

Since the roll axis is the most sensitive axis, it reveals the highest error of about 0.27 deg. The error in the other two axes is much smaller, about 0.03 deg for the pan axis, and about 0.06 deg for the tilt axis. Periodical steps can be observed for the angular error, especially for the roll orientation. They occur when the direction

of rotation of the simulated eye movement changes and consequently the actuators idle due to the non ideal compensated dead zone.

5.3. Workspace Controller

The controller presented in the last section are open–loop angle controllers, with low–level closed–loop position controllers. Due to discrepancies in response characteristics of the low–level controllers, an error arises. To account for this drawback workspace controllers are designed that adjust the camera orientation by a closed–loop controller directly.

5.3.1. PID–Controller

In a first step we implemented a PID controller that operates in workspace coordinates. The architecture for the two DoF camera orientation systems is illustrated in Figure 5.14.

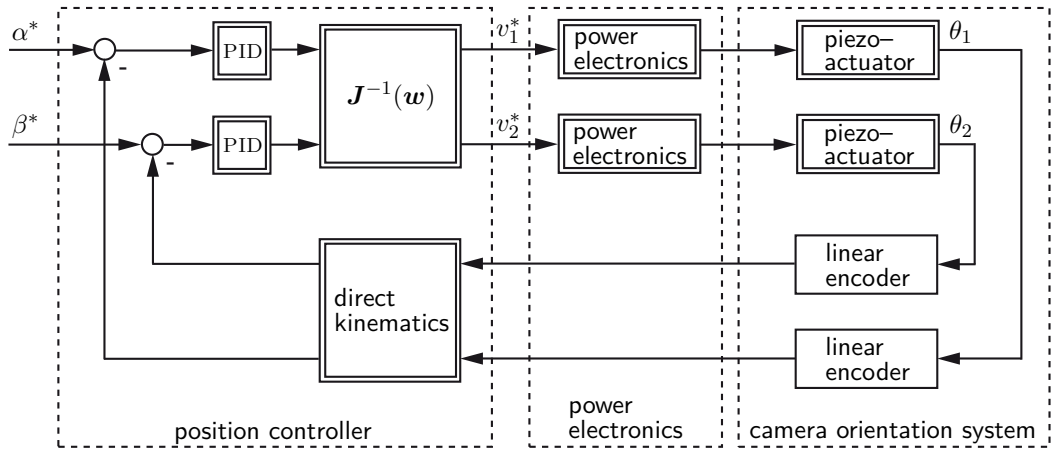

Figure 5.14.: Workspace PID controller architecture for the two DoF camera orientation systems.

The actuator positions (θ_1 and θ_2) are measured using the optical encoders and transformed to orientation angles (α and β) with the semi numerical direct kinematic solution, see Section A.1.3. After subtracting them from the desired (α^* and β^*) orientation angles, the desired velocities are calculated using two PID controllers. With the inverse Jacobian ($\boldsymbol{J}^{-1}(\boldsymbol{w})$, see (3.4)) velocities are transformed into joint space and then transmitted to the power electronics.

The presented experiments were executed using the mono camera orientation system. Figure 5.15 indicates the tracking performance with the workspace controller, when a 40 deg step is applied in the pan orientation with zero tilt angle.

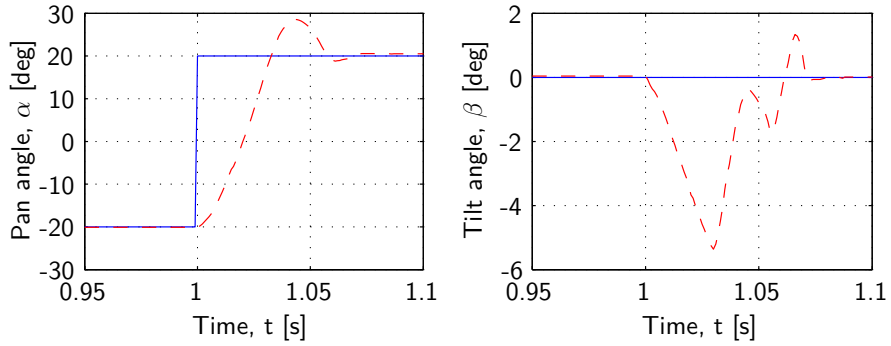

Figure 5.15.: Desired [—] and measured [– –] orientation during step response, PID workspace controller.

The left side of the figure confirms that a new desired pan orientation can be reached within 40 ms yielding an overall angular velocity of 1000 deg/s. At the same time a relatively high overshoot of about 20 % is registered. Figure 5.15 (right) indicates that an angular error in the tilt orientation of less then 6 deg occurs.
Figure 5.16 presents the angular position error of the camera orientation during sinusoidal movements with an amplitude of 20 deg and a frequency of 0.5 Hz applied to the pan axis while the tilt axis is kept zero.

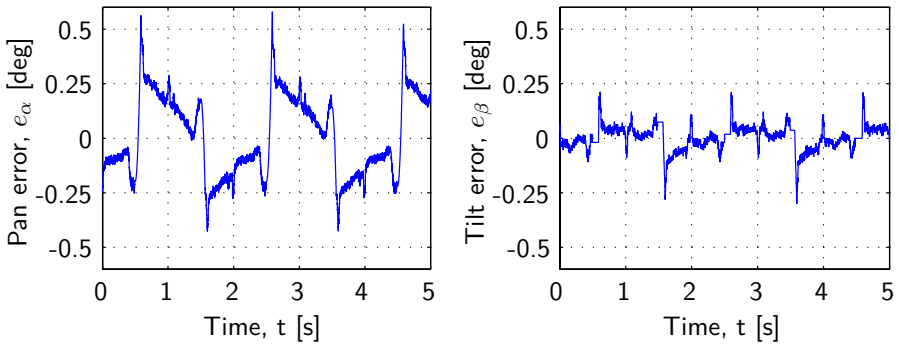

Figure 5.16.: Angular error during sinusoidal movements, PID workspace controller.

The graphs reveal that the orientation error remains below 0.6 deg for the pan and 0.28 deg for the tilt orientation.
Since the workspace control architecture takes into account the camera orientation and not only the linear actuator positions, it should be able to compensate the negative influence of different actuator dynamic responses. However, it was not possible to decouple the two axes with the architecture presented. Thus, orientation errors can be observed in both axes. The main reason for this effect is that in the architecture presented two linear controllers must handle the nonlinear coupling between the camera and the linear axes. At present the negative influence of the nonlinear transmission ratio, induced by the gimbal joint, is not considered sufficiently. Furthermore, in Figure 5.16 steps can be observed in the angular error. Basically they arise due to the same issue, namely static friction from the used prismatic joints, as the steps registered in the joint space control architecture. The comparison of

Figure 5.10 and Figure 5.16 reveals a larger error in the latter. Choosing a stiffer workspace controller would reduce the tracking errors. However, then a much higher overshoot would be observed in step response experiments.
The investigations confirmed that the results achieved with a simple PID workspace controller were not satisfying. To gain a better decoupling of the single axes a more sophisticated control architecture is required.

5.3.2. State Space Decoupling Control

To yield an enhanced controller performance, a model based control architecture is investigated. To allow for such an approach, a state space model of the system is calculated. Using this analytical model a feedback controller is developed. Very common approaches to design such controllers are e.g. pole placement or to use a linear quadratic regulator (LQR). Since the camera orientation system follows human eye movements, the desired angles are changing all the time. In such a case the procedure introduced by Falb and Wolovich [36] suits particularly well. The basic idea of the approach is to decouple the input from the output signals, so that the controlled system is diagonalized.
To derive the control parameters, we used the classical state space description:

$$\begin{aligned} \dot{\boldsymbol{x}} &= \boldsymbol{A}\,\boldsymbol{x} + \boldsymbol{B}\,\boldsymbol{u}, \\ \boldsymbol{y} &= \boldsymbol{C}\,\boldsymbol{x} + \boldsymbol{D}\,\boldsymbol{u}. \end{aligned} \tag{5.2}$$

The four system states (α, β, $\dot{\alpha}$, and $\dot{\beta}$) are described by the vector $\boldsymbol{x}$. The input vector $\boldsymbol{u}$ corresponds to the forces applied to the prismatic joints and the output vector $\boldsymbol{y}$ to the camera orientation. $\boldsymbol{A}$ denotes the state matrix, $\boldsymbol{B}$ the input matrix, $\boldsymbol{C}$ the output matrix, and $\boldsymbol{D}$ the feed through matrix which is zero for the investigated system. The equations of motion are deduced using a simplified three mass model. To prove that the state space model represents the dynamic behavior of the entire system, the model is validated using a *MBSim* dynamic simulation model. The latter accounts for the entire manipulator. Since the derivation of the equations of motion is extensive, the calculations are presented in Appendix B. The matrices for the mono camera orientation system are illustrated exemplarily, see (B.25)[1].
The selected controller obeys the following state feedback law:

$$\boldsymbol{u} = -\boldsymbol{R}\,\boldsymbol{x} + \boldsymbol{F}\,\boldsymbol{w}. \tag{5.3}$$

The desired values are described with $\boldsymbol{w}$, the feedback control matrix with $\boldsymbol{R}$, and the pre–filter matrix with $\boldsymbol{F}$. To determine the two matrices, each system output y_i is repeatedly differentiated with respect to time until a dependency from the input vector $\boldsymbol{u}$ occurs.

$$y_i^{(\delta_i)} = \boldsymbol{c}_i^T \boldsymbol{A}^{\delta_i} \boldsymbol{x} + \boldsymbol{c}_i^T \boldsymbol{A}^{\delta_i - 1} \boldsymbol{B}\,\boldsymbol{u}, \qquad i = 1, \ldots, n. \tag{5.4}$$

1 For the controller design we neglected the disturbance vector $\boldsymbol{z}$. Due to model inaccuracies the yielded values can not be applied directly for compensation. To deal with this drawback we used an additional integral controller.

The amount of required differentiations for each output is denoted with δ_i, while $\boldsymbol{c}_i^T$ denotes the i–th row of the input matrix $\boldsymbol{C}$. Inserting (5.3) in (5.4) leads to:

$$y_i^{(\delta_i)} = \left(\boldsymbol{c}_i^T \boldsymbol{A}^{\delta_i} - \boldsymbol{c}_i^T \boldsymbol{A}^{\delta_{i-1}} \boldsymbol{B}\boldsymbol{R}\right) \boldsymbol{x} + \boldsymbol{c}_i^T \boldsymbol{A}^{\delta_{i-1}} \boldsymbol{B}\boldsymbol{F}\boldsymbol{w}, \qquad i = 1, \ldots, n. \tag{5.5}$$

Furthermore, the dependency of each output from the input vector can be formulated as follows:

$$\boldsymbol{D}^* = \begin{bmatrix} \boldsymbol{c}_1^T \boldsymbol{A}^{\delta_1 - 1} \boldsymbol{B} \\ \vdots \\ \boldsymbol{c}_n^T \boldsymbol{A}^{\delta_n - 1} \boldsymbol{B} \end{bmatrix}. \tag{5.6}$$

To yield a decoupling, it is important that every output depends on the respective input and its derivations only. This relation can be illustrated with:

$$y_i^{(\delta_i)} + M_{i\delta_i - 1}\, y_i^{(\delta_i - 1)} + \cdots + M_{i1}\, \dot{y}_i + M_{i0}\, y_i = k_i\, w_i, \qquad i = 1, \ldots, n, \tag{5.7}$$

where $M_{i\delta_i - 1}$ and k_i indicate design parameters. Inserting (5.7) into (5.5) and considering (5.6) the feedback control matrix $\boldsymbol{R}$ and the pre–filter matrix $\boldsymbol{F}$ are determined. For the investigated system with two DoF the matrices can be calculated as follows:

$$\boldsymbol{R} = (\boldsymbol{D}^*)^{-1} \begin{bmatrix} \boldsymbol{c}_1^T \boldsymbol{A}^{\delta_1} + \sum_{m=0}^{\delta_1 - 1} M_{1m}\, \boldsymbol{c}_1^T \boldsymbol{A}^m \\ \boldsymbol{c}_2^T \boldsymbol{A}^{\delta_2} + \sum_{m=0}^{\delta_2 - 1} M_{2m}\, \boldsymbol{c}_2^T \boldsymbol{A}^m \end{bmatrix}, \tag{5.8}$$

$$\boldsymbol{F} = (\boldsymbol{D}^*)^{-1} \begin{bmatrix} k_1 & 0 \\ 0 & k_2 \end{bmatrix}. \tag{5.9}$$

As (5.8) and (5.9) reveals, it is only possible to decouple the system if the matrix (5.6) is invertible ($det(\boldsymbol{D}^*) \neq 0$). Since the investigated system fulfills this requirement and the entire amount of differentiations ($\delta = \delta_1 + \delta_2 = 4$) is equal to the plant order, a stable decoupling controller can be derived [63]. Using the parameters $M_{i\delta_i - 1}$ and k_i, introduced in (5.7), the controlled system is designed to imitate a desired second order transfer function.

$$y_i = \frac{k_i}{s^2 + M_{i1} s + M_{i0}}\, w_i, \qquad i = 1{,}2. \tag{5.10}$$

The values for k_i and M_{i0} must be equal to guarantee diminishing steady–state errors, see (5.10).

To allow for a state space controller, the four system states must be available. However, in the case of the investigated camera orientation system only the linear actuators' positions can be measured. Using the direct kinematic solution the camera orientation can be calculated from the actuator positions. Since the camera velocity can not be measured it is estimated using an observer. A standard observer is able to estimate all states of a system. Since two of the states are already known from

measurements we used a reduced observer, see e.g. [38]. To develop the reduced observer (5.2) is re–written as:

$$\underbrace{\begin{bmatrix}\dot{\boldsymbol{x}}_e\\ \dot{\boldsymbol{x}}_m\end{bmatrix}}_{\dot{\boldsymbol{x}}} = \underbrace{\begin{bmatrix}\boldsymbol{A}_{11}\,\boldsymbol{A}_{12}\\ \boldsymbol{A}_{21}\,\boldsymbol{A}_{22}\end{bmatrix}}_{\boldsymbol{A}}\underbrace{\begin{bmatrix}\boldsymbol{x}_e\\ \boldsymbol{x}_m\end{bmatrix}}_{\boldsymbol{x}} + \underbrace{\begin{bmatrix}\boldsymbol{B}_1\\ \boldsymbol{B}_2\end{bmatrix}}_{\boldsymbol{B}}\boldsymbol{u}, \tag{5.11}$$

where the vectors and matrices related to the estimated states are described with index e and the measured states with index m. According to [38] the reduced observer can be described as follows:

$$\dot{\tilde{\boldsymbol{x}}}_e = (\boldsymbol{A}_{11} - \boldsymbol{L}\boldsymbol{A}_{21})\,\tilde{\boldsymbol{x}}_e + (\boldsymbol{B}_1 - \boldsymbol{L}\boldsymbol{B}_2)\,\boldsymbol{u} + ((\boldsymbol{A}_{11} - \boldsymbol{L}\boldsymbol{A}_{21})\,\boldsymbol{L} + \boldsymbol{A}_{12} - \boldsymbol{L}\boldsymbol{A}_{22})\,\boldsymbol{y}, \tag{5.12}$$

$$\hat{\boldsymbol{x}}_e = \tilde{\boldsymbol{x}}_e + \boldsymbol{L}\boldsymbol{y}. \tag{5.13}$$

The state vector of the reduced observer is described by $\tilde{\boldsymbol{x}}_e$, while the estimated states of the system are denoted with $\hat{\boldsymbol{x}}_e$. Using the matrix $\boldsymbol{L}$ the eigenvalues of the matrix $(\boldsymbol{A}_{11} - \boldsymbol{L}\boldsymbol{A}_{21})$ can be adjusted. To yield a good trade off between filtering and short settling time we chose the observer poles to be two times faster than the system poles.

Finally, the implemented workspace decoupling control architecture is introduced in Figure 5.17.

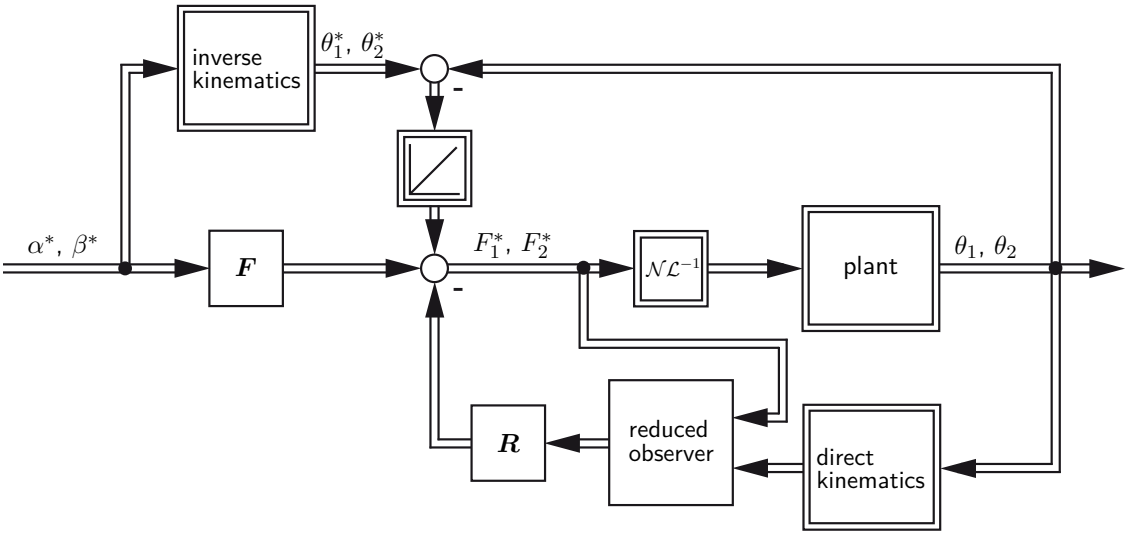

Figure 5.17.: Workspace decoupling controller architecture for the two DoF camera orientation systems.

Onto the commanded angle orientation (α^* and β^*) the pre–filter matrix $\boldsymbol{F}$ is applied. Using the actuator dead zone compensation, see Section 5.1.3, the calculated forces (F_1^* and F_2^*) are transferred to the power electronics, which converts the desired values to piezo–actuator control signals. While the actuators are used to orient the camera, the actuators' position is measured using optical encoders. To keep the

diagram simple, the single sub–components of the plant are omitted. The measured positions (θ_1 and θ_2) are converted to the camera orientation using the direct kinematic solution. Besides the camera orientation, the reduced observer takes the desired forces as an input signal to calculate the two non–measurable system states ($\dot{\alpha}$ and $\dot{\beta}$). At last, the loop is closed over the feedback matrix $\boldsymbol{R}$. Measurements with the joint space controller indicated that better control results can be achieved by limiting the maximum camera velocity. Thus, also for the workspace controller a rate limiter is used to restrict the velocities to 800 deg/s.
To deal with model inaccuracies we also implemented a joint space integral controller. As for the other architectures, the controller is equipped with an integral anti–windup and the set values (θ_1^* and θ_2^*) are calculated with the inverse kinematic solution from the desired orientation.

We applied a step from -20 deg to 20 deg in the pan orientation while the tilt orientation was kept to zero to imitate saccadic human eye movements.

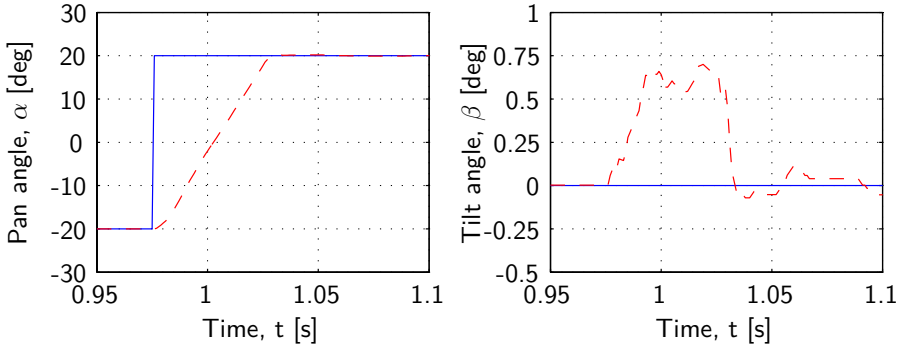

Figure 5.18.: Desired [—] and measured [– –] orientation during step response, workspace decoupling controller, angular velocities limited to 800 deg/s.

The left side of the plot illustrates, that new desired pan orientations can be reached in about 55 ms, which yields an average angular velocity of about 720 deg/s. An overshoot of less than 1 % was found. Figure 5.18 (right) reveals only a small orientation error of about 0.7 deg in the tilt direction. As expected, better step response results can be achieved with the workspace decoupling controller than with the simple joint space PID controller. The negative influence in the non–tilted axis was reduced by a factor two.
To imitate human eye slow phases, sinusoidal movements with an amplitude of 20 deg and a frequency of 0.5 Hz were performed around the pan axis, while the tilt axis was held to zero.

The orientation error remained below 0.175 deg for the pan and 0.115 deg for the tilt orientation. Again, the error peaks coincide with the moment when the rotation changes and the actuators idle. Compared to the joint space controller, the maximum errors are slightly increased, but the average control error is reduced.
Since the decoupling controller is based on a model of the camera orientation system, the influence between the two camera axes was reduced and the best control results

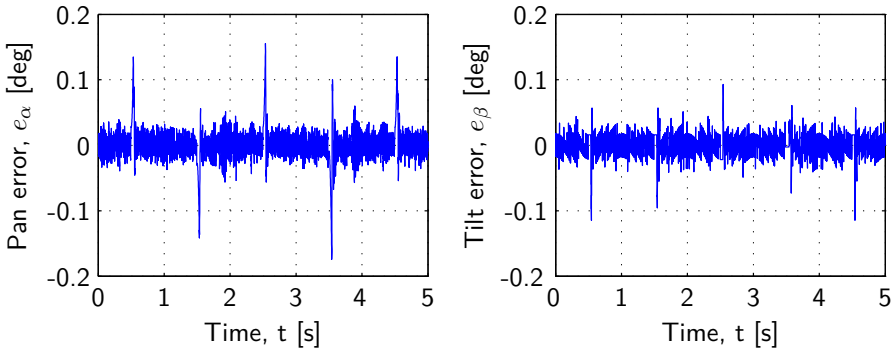

Figure 5.19.: Angular error during sinusoidal movements, workspace decoupling controller.

were achieved. However, the implementation and calculation effort is the highest of all investigated approaches.

5.4. Additional Experiments

In the previous two sections different investigated control approaches were introduced. The PID joint space controller and the workspace decoupling controller were found to be the most suitable approaches. The latter provides the best control results at the cost of a more complex implementation.
The current head–mounted gaze–driven camera system setup provides two small micro controllers which are used to adjust one single piezo–actuator each. In doing so a compact package size is yielded. The drawback is that the controllers are not very powerful and that the communication between them is restricted. Thus, at the moment it is not possible to implement the workspace decoupling controller on the portable system. Therefore, the following experiments were conducted with the joint space PID controller.

5.4.1. Frequency Response

According to Carpenter [19] and Glasauer [42] the frequency response of a human eye can be roughly described as a first–order low–pass system with a characteristic frequency of about 1 to 2 Hz. To prove that the developed camera orientation devices are able to deal with such a behavior, frequency response measurements were conducted with all three systems.
The transfer function between desired and measured orientation of the single camera axes was determined using sinusoidal activation signals with an amplitude of 20 deg. Due to the analog mechanical design, similar control results were achieved with the mono and the stereo camera orientation system. Thus, only the measurements related to the mono camera system are introduced here, see Figure 5.20, while the results of the stereo camera system are reported in Section C.3. For a comparison, also the human eye frequency response is plotted.

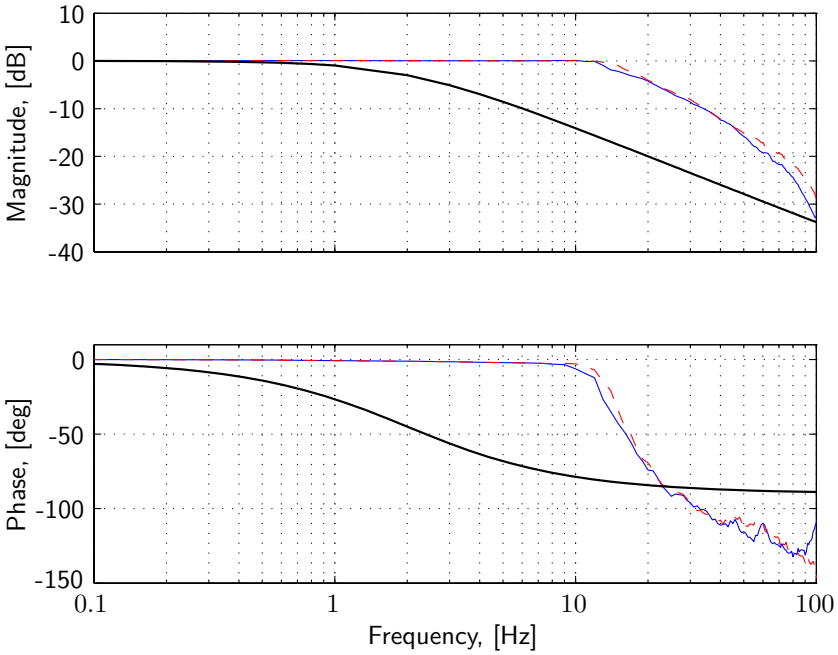

Figure 5.20.: Frequency response of the mono camera orientation system around the pan [—] and the tilt axis [– –] as well as a first–order low–pass system [**—**] with a cut–off frequency of 2 Hz.

The system cut–off frequency is about 17 Hz for movements around the pan axis and about 18.5 Hz for movements around the tilt axis. A possible explanation for the differences in the two axes can be found in the camera's signal cable arrangement, which is used to read the acquired images. Due to the arrangement, this cable is tilted less during orientation changes around the tilt axis. As mentioned before, experiments with the stereo camera orientation system provided similar results; a cut–off frequency of about 17 Hz around the pan axis and a frequency of about 18 Hz around the tilt axis. We also performed measurements with the three DoF camera orientation system. They illustrated that the behavior around the pan and the tilt axes are nearly identical and have a cut–off frequency of about 26 Hz, see Section C.3. Thus, compared to the systems with two DoF a higher frequency can be reached due to the smaller design and oriented masses. Around the roll axis, where the inertial mass is even smaller, a cut–off frequency of about 39 deg was registered.
The conducted measurements indicated clearly that all developed camera orientation systems are able to outreach the requirements posed on the cut–off frequency.

5.4.2. Latencies between Eye and Camera Movements

One application scenario of the introduced camera orientation devices is the employment as part of a head–mounted gaze–driven camera system. To meet the requirements, latencies between human eye and camera movements must be small. The following investigations were carried out together with project partners from the Chair for Clinical Neurosciences, LMU Munich.

We conducted latency measurements including the whole head–mounted gaze–driven camera system. To yield objective results, an artificial eye is oriented using a model aircraft servo actuator imitating the movements of a human eye. These movements are estimated by a custom–made eye tracker [26] running at 500 Hz and are passed to the camera orientation system. Both the orientation artificial eye and the camera changes are measured using small gyroscopes. In Figure 5.21 an overview of the measurement setup is given.

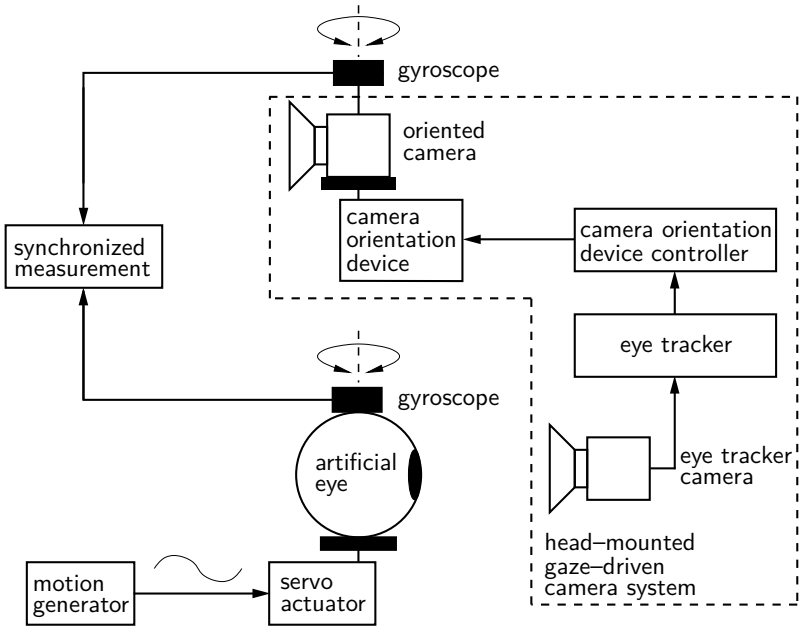

Figure 5.21.: Overall latency measurement setup, modified from [113].

Using a motion generator the artificial eye was oriented with frequencies from 0.5 Hz to 20 Hz. Figure 5.22 indicates the artificial eye and the oriented camera velocities for a frequency of about 5 Hz.

To determine the overall system latency, the phase differences between the two measured signals are calculated. The experiments revealed that the mean latency is about 10 ms, while the frequency of the simulated eye movement plays only a minor role. Thus, the overall latency is in the human vestibulo–ocular reflex range, see [60]. The introduced measurements were performed with the mono camera orientation system. Since the performance of the remaining two systems is similar or even higher, it can be deduced that also for the remaining systems the delay is in the same range.

5.4.3. Image Quality

The investigations presented in this section focus on the effect of the controller on the image quality. Therefore, pictures are acquired by a digital camera mounted on the mono camera orientation device with a resolution of 320 x 240 pixels at 120 Hz. The

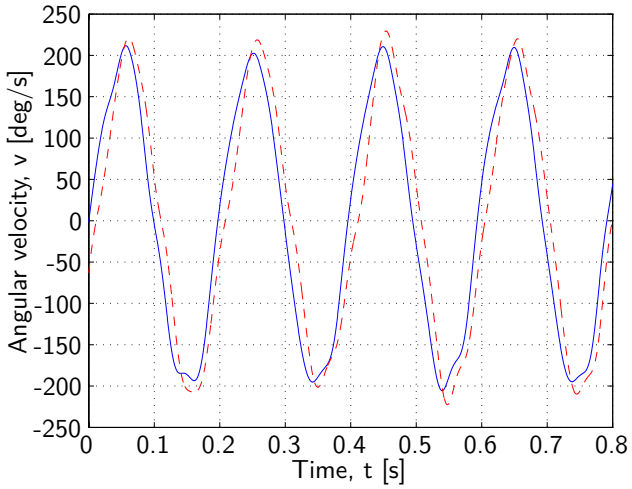

Figure 5.22.: Artificial eye [—] and oriented camera [– –] angular velocities; courtesy of the Chair for Clinical Neurosciences, LMU Munich.

system performs different motion patterns, which imitate the three major groups of human eye movements: fixations, smooth pursuit, and saccades, see Section 2.1. During fixations, the human eye is nearly stationary, so that fixed desired camera orientations must be adjusted with the mechanical device. Once the desired orientations are reached, the camera does not perform any motions. Therefore, the image quality reaches the level of fixed cameras. The first picture in Figure 5.23 presents an example of an image which is acquired during fixation.

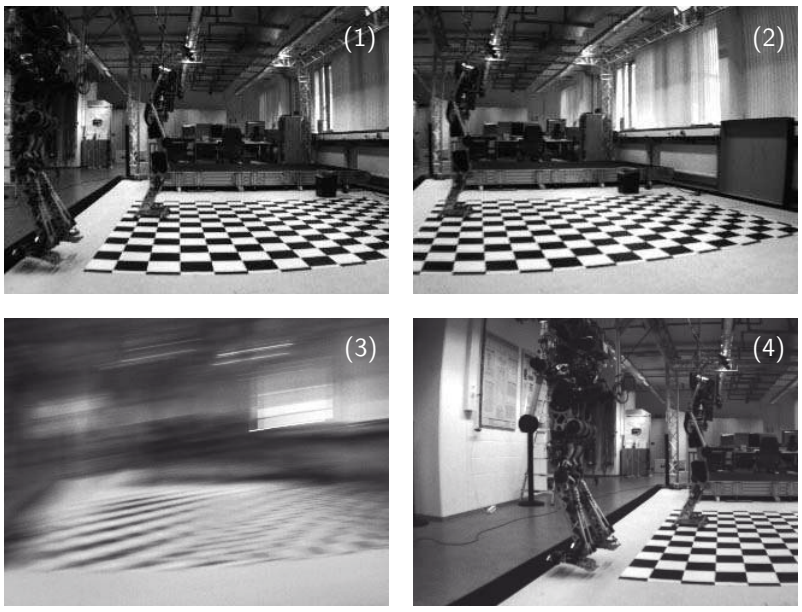

Figure 5.23.: Images acquired during fixation (1), smooth pursuit (2), saccade (3) and after saccade (4).

The second image in Figure 5.23 is acquired during simulated smooth pursuit movements. During that process sinusoidal orientation changes are performed by the

device. Figure 5.10 reveals that the camera is exposed to small vibrations during such movements. However, due to the high camera frame rate and the precision of the mechanical assembly, the subjective quality of this image can be compared to images acquired during fixations. Finally saccades are simulated, whereas the device is performing square pulse movements. The images obtained directly during the step, where velocities of over 1000 deg/s are reached in the pan direction and small deviation occurs in the tilt orientation, are blurred, see the third image in Figure 5.23. The last image is acquired at the end of a saccade. At this time, the camera does not perform movements, thus the subjective quality of this image matches the image quality during fixations.
The images gained from a human's eye during saccades are also blurred and the human brain discards them. Thus, humans are blind during saccades, see [28].
The illustrated procedure is also applied to the stereo camera orientation system and to the three DoF camera orientation system. After subjective evaluation it can be stated, that high quality images can be acquired with the camera orientation systems while performing eye like motion patterns.

5.5. Discussion

This chapter deals with the control of the developed camera orientation systems. Therefore, an overview of the actuators' operation principle and of the power electronics was given. We reported on the nonlinear dynamic behavior of the amplifier, which resulted in varying time delays. However, they were so short that new driving signals could be applied to the actuators in less than one controller time step. Furthermore, it was observed that by applying small input signals to the power electronics, a dead zone was found. We illustrated the main reasons for this behavior and introduced methods for compensation.
Subsequently, different control structures were discussed which can be subdivided into two groups: joint space and workspace controllers. First, open–loop angle controllers, with subordinate closed–loop position controllers were investigated. They feature a simple setup, at the cost of reduced orientation accuracy. To account for this drawback, workspace controllers were designed, where the camera orientation is directly adjusted by a closed–loop controller. All controllers introduced were verified experimentally. Step response measurements were used to imitate human eye saccadic movements and sinusoidal following behavior measurements were performed to simulate smooth pursuit of the humans eye. Based on the experiments it can be stated, that the PID joint space controller and the workspace decoupling controller were found to be the most suitable approaches.
Step response measurements performed with the two DoF camera orientation systems using the simple joint space PID controller revealed that commanded camera orientations can be reached with average velocities of more than 1000 deg/s and a small overshoot of about 1 %. However, the measurements also indicated, that a control error arises in the non–tilted axis which is restricted to the same small time as the orientation changes in the deflected axis. Due to the used parallel kinematics,

there is a mechanical coupling between the single linear positions and both orientation angles. Thus, a position error in a linear axis affects both orientations. Since the human eye is able to fulfill movements with velocities of up to 500 deg/s, the velocities of the technical system were limited artificially. By doing so, the time period during which the piezo–actuators are in saturation were minimized and the negative influence in the non–tilted axis was reduced.
A possibility to further reduce the coupling between the single orientations was presented in form of a model–based workspace controller. To allow for such an approach, a state space model was determined and validated. Using the method proposed by Falb and Wolovich a so–called decoupling controller was developed. While the simulated saccades yielded better control results with the workspace controller, comparable results were achieved for simulated slow phases. The drawback is a higher computational cost.
At present the head–mounted gaze–driven camera system provides a small controller for each piezo–actuator, yielding a compact package size. Since the controllers are not very powerful and the communication between them is restricted, it is not possible to implement the workspace decoupling controller directly on the overall system. Therefore, we selected the joint space PID controller and adapted it also to the three DoF system. Measurements indicated that it is possible to orient a camera around the pan and tilt axes with an average velocity of over 1000 deg/s. Since the inertial mass around the roll axis is smaller, even higher average velocities, of over 2500 deg/s, can be reached around the third axis.
In addition to the step response and following behavior experiments, also frequency response measurements were performed. Cut–off frequencies from 17 Hz (around the pan orientation of the mono and the stereo camera orientation system) to 39 Hz (around the roll orientation of the three DoF camera orientation system) were registered. It can be stated that the developed mechatronic systems outreach the human eye capabilities by about ten times.
Overall latency measurements revealed further that due to the high dynamic output capabilities of the camera orientation devices, the head–mounted gaze–driven camera system has a delay of about 10 ms. Therefore, the system is able to provide stabilized images without any ulterior image post–processing.
Finally, the quality of acquired images when the system was performing human eye–like motions was evaluated subjectively. The quality of images is comparable to images acquired with a static camera. Exceptions are images acquired during saccades, which are blurred. However, during saccades also images acquired from the human eye are blurred and therefore discarded by the human brain.

6. Applications

In this chapter different application scenarios for the developed camera orientation devices are introduced. Integration was performed in collaboration with project partners from the Chair for Clinical Neurosciences, LMU Munich (gaze–driven head–mounted camera, remote eye tracker, and Wizard–of–Oz), the Institute for Human–Machine Communication, TUM (remote eye tracker), and the Institute for Cognitive Systems, TUM (humanoid robot eyes). In Section 6.1 the setup of three different gaze–driven head–mounted camera systems is presented. An active remote eye tracker is introduced in Section 6.2. The camera orientation systems are also intended to be used as robotic eyes in a humanoid robot, see Section 6.3. In Section 6.4 two platforms for eye–related Wizard–of–Oz experiments are illustrated. Finally, Section 6.5 concludes the chapter with a discussion.

6.1. Gaze–driven head–mounted Camera System

The main application of the developed camera orientation devices is a gaze–driven head–mounted camera orientation system. Such a portable system is able to determine the human line of sight and to align continuously at least one camera in the same direction. The device enables the performance of fundamental studies on human gaze behavior in natural environments. Furthermore, images from a user's perspective can be acquired e.g. for documentation or educational purposes.

In the following paragraphs, three different gaze–driven head–mounted camera systems are introduced. As the name implies, the systems are worn on the head. To allow for an adequate fixation the components are mounted on modified swimming goggles. Using Velcro stripes the goggles can be adapted to different head sizes. Thus, adequate wearing comfort is achieved, while goggles slippage is reduced.
During operation the human eyes are illuminated with infrared (IR) light, which is invisible to humans. In front of the human eyes semi–transparent mirrors are placed. They redirect IR light to the video oculography (VOG) cameras, while they transmit visible light. Evaluating the VOG camera images the human gaze direction is estimated. Algorithms for calculations are running on portable computers, which are also used to store the acquired data and to provide the needed power for the cameras as well as the camera orientation systems.

First, the mono camera configuration is introduced, see Figure 6.1. The VOG cameras are arranged on the left and on the right side of the human head at eye level. After identifying the human line of sight the "gaze camera" is aligned with it using the camera orientation device. The gaze camera is able to acquire high resolution

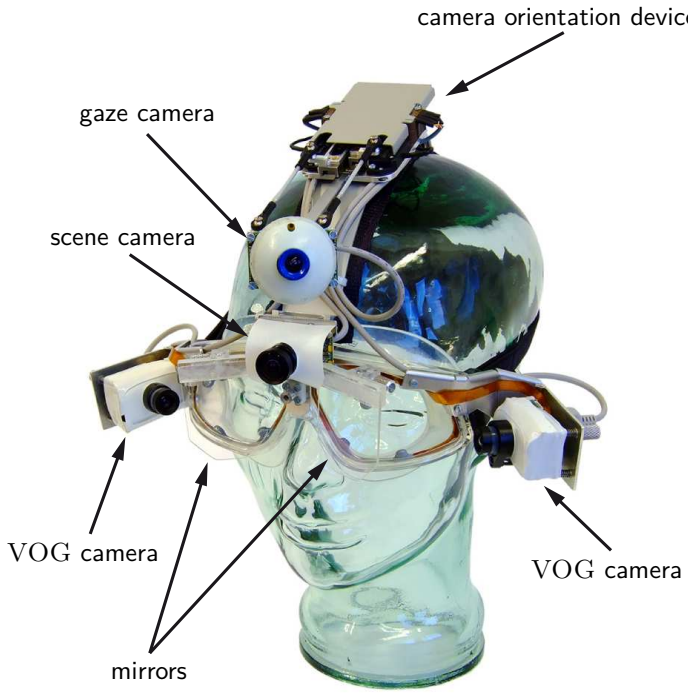

Figure 6.1.: Head–mounted gaze–driven mono camera system; courtesy of the Chair for Clinical Neurosciences, LMU Munich.

detail images. A fourth camera is mounted above the nose between the human eyes. This so called "scene camera" is used to acquire low resolution overview images of the entire scene. By combining the gaze and scene images into a single one, a hybrid perspective is gained [111]. Two examples of such pictures are presented in Figure 6.2.

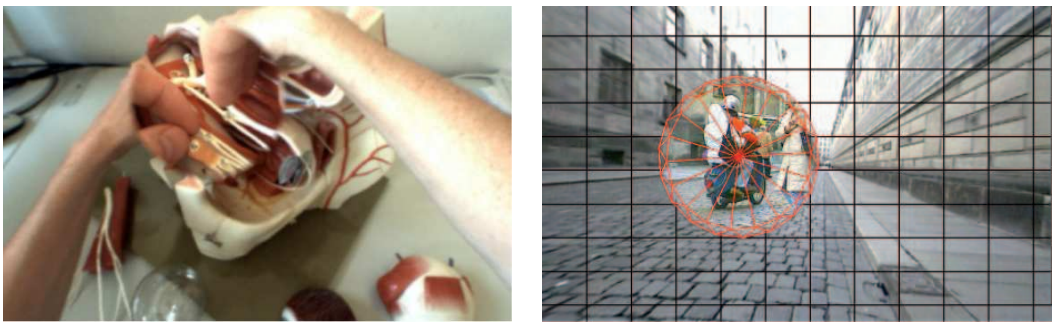

Figure 6.2.: Hybrid perspective images: looking at an eye model (left), looking at a motor scooter (right); courtesy of the Chair for Clinical Neurosciences, LMU Munich.

In these images, similar to the human fovea, only the region that people are directly looking at is acquired with high resolution and the surroundings are acquired with a reduced resolution. To distinguish the single pictures in Figure 6.2 (right) the image acquired with the scene camera is overlaid with a rectangular grid, the one acquired with the gaze camera is circled.

In Figure 6.3 a preliminary version of the stereo camera configuration is introduced. On the left and on the right side of the human head the camera orientation systems are fixed. The scene camera is mounted above the nose between the eyes. However, in the presented version, the final eye tracker is not installed. Therefore, only the left camera orientation system is used to align the gaze camera with the human line of sight. On the right camera orientation system the VOG camera is mounted. Thus, the camera orientation is always fixed to the semi–transparent mirror in front of the right eye and so images of the eye are acquired.

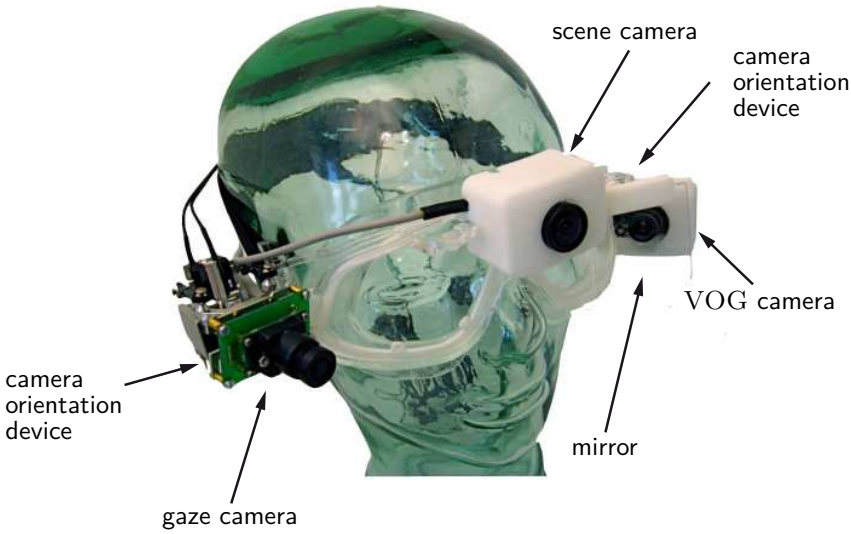

Figure 6.3.: Preliminary version of the head–mounted gaze–driven stereo camera system; courtesy of the Chair for Clinical Neurosciences, LMU Munich.

Figure 6.4 illustrates a preliminary version of the configuration with three DoF. In contrast to its predecessors the custom made fixation parts are designed using rapid prototyping (3D printing), yielding a compact and lightweight design.

As for the stereo camera system the camera orientation devices are intended to be fixed on the left and on the right side of the human head. However, in a first integration step we arranged only one three DoF camera orientation system on the right side, while on the left a box, housing the needed electronic components, is attached. In the previous two versions (mono and stereo), this box is situated on the back of the head. Further, the VOG cameras, situated above the eyes and the semi–transparent mirrors are depicted in the figure.

6.2. Remote Eye Tracker

Besides head–mounted eye trackers, a vast amount of remote eye trackers are known in the literature. In this approach the VOG cameras are e.g. integrated into a

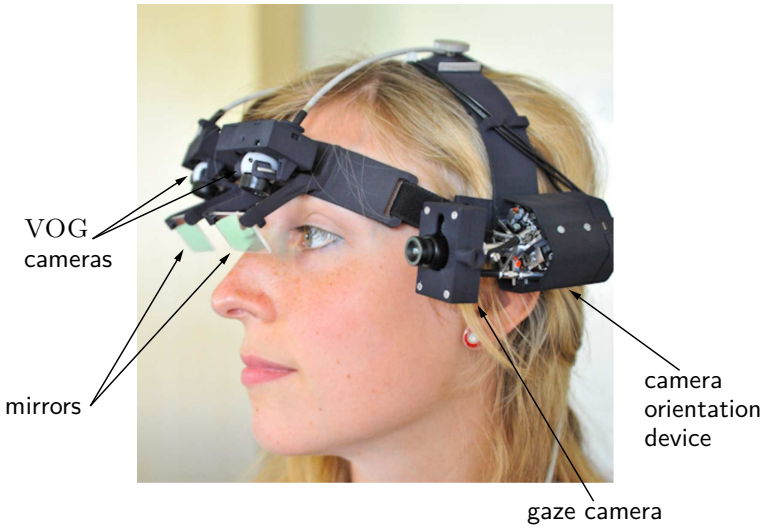

Figure 6.4.: Preliminary version of the head–mounted gaze–driven camera system with three DoF; courtesy of the Chair for Clinical Neurosciences, LMU Munich.

computer display. With such a system the gaze behavior of users can be investigated without the need for devices attached to the human head. The drawbacks are a restricted operational range and limited resolution. Using active camera orientation systems, these drawbacks can be compensated. Such systems are known in the literature too. However, usually only the gaze direction of a single person can be determined.

In Figure 6.5 a remote eye tracker with active camera orientation systems is introduced. Due to the fast camera orientation systems it is possible to investigate the gaze direction of more than one subject.
Using the scene camera, an overview of the monitored field is acquired and the user's position in front of the system can be determined. The VOG cameras are mounted on the two camera orientation systems. They are adjusted to a user's face and thus the line of sight can be determined. For the gaze direction estimation of a different user, the VOG cameras have to be reoriented. Afterwards the cameras are switched to a further user.
In the background of Figure 6.5, the images acquired with the different cameras are depicted. While images acquired with the scene camera give an overview of the investigated area, images acquired with the VOG cameras represent the user's face.

6.3. Humanoid Robot Eyes

In recent years a growing amount of publications on humanoid robots can be found in the literature. To enhance their autonomy most systems are equipped with a vision system. It is common to arrange two cameras as stereo pairs in the robot head. Different approaches, ranging from static mounted cameras, through systems

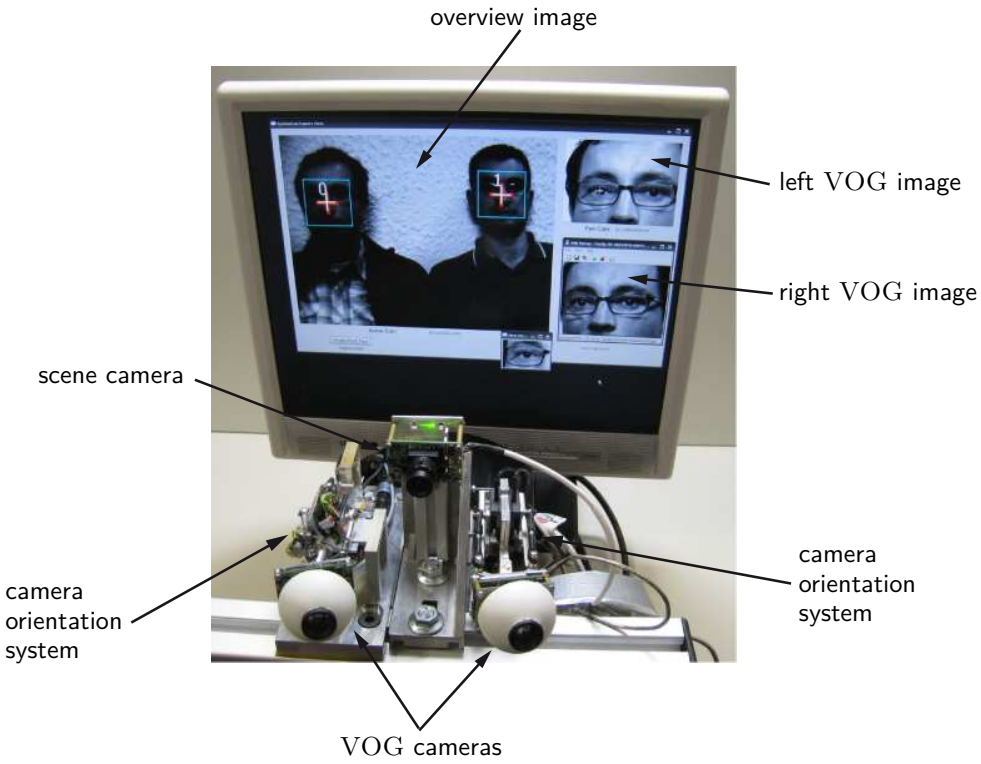

Figure 6.5.: Remote eye tracker with active camera orientation systems; courtesy of the Chair for Clinical Neurosciences, LMU Munich and the Institute for Human–Machine Communication, TUM.

with active neck, to devices with oriented cameras are investigated. However, only few systems are reported which are able to orient two cameras independently from each other around three axes.
Therefore, the development of an active vision system with two "eyes", using our three DoF camera orientation devices, was investigated. This system can be used to guide robots in the real world and to naturally, nonverbally communicate with humans.
In the first step, we arranged a pair of three DoF camera orientation systems with a human interpupillary distance, see Figure 6.6. That way a platform for an active vision system is provided, where the computer vision algorithm can be developed and tested. In the next step, the system integration in a humanoid's head is planned.

6.4. Wizard–of–Oz Experiments

Experiments, where humans interact with a computer system which is believed to be autonomous, but is fully or partially operated by a human, are very popular in the field of human–computer interaction. Such investigations are known as Wizard–of–Oz experiments, see [55] for more information.

Figure 6.6.: Preliminary active vision system intended for humanoid robots; courtesy of the Institute for Cognitive Systems, TUM.

Using the developed camera orientation systems two different platforms for eye–related Wizard–of–Oz experiments were set up. In both cases, the camera orientation systems are used to imitate the human eye movements. The cameras are steered by a hidden operator wearing an eye–tracker. To mimic human eye balls the cameras are covered with table tennis balls.
Figure 6.7 (left) presents the camera orientation systems mounted on the humanoid robot JOHNNIE [79]. On the right side of Figure 6.7, the integration of the camera orientation systems into a human–sized styrofoam head is depicted.

6.5. Discussion

The present chapter reports on the integration of the developed camera orientation systems into different application scenarios. All of them profit from the fact that the camera orientation devices combine high dynamic orientation output capabilities with a small and lightweight design. The described integration was carried out in collaboration with different project partners.
All three camera orientation devices were used to set up head–mounted gaze–driven camera orientation systems. Due to the fact that the three DoF device is the smallest one and that the used eye–tracker was revised, the most compact overall system resulted. The developed head–mounted gaze–driven camera systems provide a research tool which can be used in various research fields of vision, in natural environments and for subjective documentation e.g. surgery. Using the camera orientation devices we developed an active remote eye–tracker. The output capability of the system in terms of high dynamic orientation changes allows one to track more users contemporaneously by switching quickly between them. We further reported the first integration steps towards an active vision system for humanoid robots. This

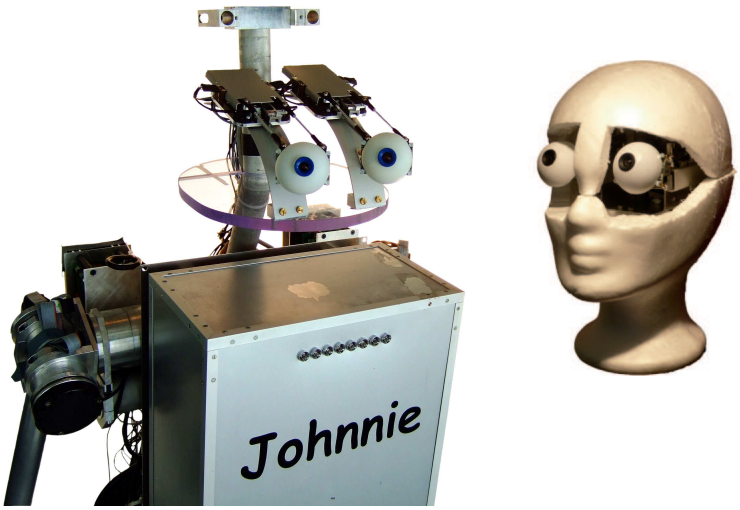

Figure 6.7.: Eye related Wizard–of–Oz setup: eyes mounted on the humanoid JOHNNIE (left), eyes integrated into a human sized styrofoam head (right); courtesy of the Chair for Clinical Neurosciences, LMU Munich.

system will be composed of a human–like head with two eyes. To represent the eyes, we used the three DoF camera orientation devices. By doing so, the robotic head is able to reproduce all rotational DoF of the human eye. Besides acquiring images from the surroundings, the robotic eyes can also be used for a natural nonverbal communication. Finally, the design of two eye–related Wizard–of–Oz scenarios were introduced. In such cases the camera orientation systems are driven by a hidden user wearing an eye–tracker.

7. Conclusions and Future Directions

7.1. Discussion

The design and control of compact high–dynamic camera orientation systems is introduced in this thesis. The achieved system performance outreaches the human oculomotor system, while featuring a small design.

In Chapter 2 the capabilities and main reflexes of the human oculomotor system are introduced. Based on these observations, the requirements on the technical systems are formulated. Focusing on active camera orientation systems and giving an overview of digital image stabilization, the state of the art is introduced. Due to the fact that no known device was able to fulfill all demands, possible approaches were introduced and evaluated. In doing so active systems based on small parallel kinematic manipulators were found to be the most suitable solution.

In Chapter 3 two camera orientation systems with two DoF each are introduced. Both systems are based on a parallel kinematics. Using the same structure and modifying the kinematic parameters only, the devices are suitable for different application scenarios. After a rough estimation of requirements, different actuator and sensor concepts were introduced and compared. On the theoretical side, the inverse and direct kinematic solutions were calculated. Besides allowing the development of the closed–loop control architectures, these functions were required to calculate and optimize the workspace. After optimizing the structure, the dimensions and the masses of the mechanical components were determined. These data were used to parameterize the kinematic and dynamic simulation models. Simulations confirmed that the camera orientation systems are able to reproduce human eye movements. Thus, the devices were set up and discussed along with their specifications.

The three DoF camera orientation system, introduced in Chapter 4, is based on a small parallel kinematic manipulator too. During experiments with the two DoF devices, requirements for the three DoF system were found. While the demands on the measurement unit and design were enhanced, the requirements for the workspace were diminished. According to the previous section, demands on actuators and sensors where estimated. Subsequently, concepts and off–the–shelf products were listed and compared. Furthermore, the inverse and the direct kinematic solutions were calculated for the three DoF kinematics. The workspace/package dimension ratio was optimized conducting parameter variation studies using an implicit filtering algorithm (IFFCO). Again kinematic and dynamic simulation models were developed and parameterized appropriately. Since simulations with both models confirmed that

the investigated system is able to cope with the human eye orientation capabilities, a prototype was built.

Besides a mechanical system, also an appropriate control architecture is needed to align a camera with the human gaze direction. Chapter 5 investigates different approaches. Thereby, the focus was firstly laid on the actuator system and the dead zone compensation. Afterwards, different linear and nonlinear control strategies were introduced. Among others, a state space decoupling controller, based on a Falb and Wolovich scheme, was developed and the equations of motion were established. Step response and following behavior measurements were performed with all developed controllers. The joint space PID controller and particularly the state space decoupling controller provide the best results. However, due to the higher computational amount, the decoupling approach was not realizable on to the current electronic hardware of the gaze–driven head–mounted camera system. Thus, the PID controller was used and additional measurements were executed. The experiments confirmed that all developed camera orientation systems are able to outreach the human oculomotor system. Furthermore, the quality of the images acquired during orientation changes was subjectively evaluated and classified as comparable to the one of static mounted cameras.

Finally, the integration of the camera orientation devices into various application scenarios is described in Chapter 6. First of all, the three designed head–mounted gaze–driven camera systems were introduced. The research tools gained can be used to investigate research questions in the field of vision and subjective documentation. The camera orientation systems were further used to develop a remote eye–tracker, and eye–related Wizard–of–Oz platforms. After that, first steps to equip a humanoid robot head with “eyes” were presented, too.

7.2. Outlook

The presented work reports on the design and development of compact high–dynamic camera orientation systems. In the following, possible extensions and directions for future research are shown.

Tracking behavior experiments illustrated that the control error increases when the direction of rotation of simulated eye movement changes. This error occurs because the actuators are idling and the dead zone must be overcome before the motion restarts. With the developed compensations this effect could not be completely avoided. Therefore, enhancing the compensation procedure would be a promising extension.

Measurements revealed further that the workspace decoupling controller achieves the best results. However, the control structure is developed using a simple three mass model. Simulations indicated that this model is valid for short time periods only. Refining the level of detail and enhancing the approximation of the inverse kinematic solution, e.g. by using piecewise linear functions, the model validity, and

thus also the performance of the controller, could be improved. So far, the approach was applied to the mono camera system only. However, the controller would be beneficial for all presented camera orientation systems and their applications. Therefore, the equation of motion for all camera orientation devices must be established. Furthermore, the microprocessors used for the head–mounted gaze–driven camera system must be substituted with faster ones or with field programmable gate arrays (FPGA) to cope with the higher computation amount.

Another field of research can be accessed by investigating the piezo–actuator power electronics. As reported, this electronics exhibit a nonlinear behavior and has to be adapted to the single actuators manually. By designing an adaptive driving circuit, the starting time can be shortened and the control results improved. Momentarily each actuator has its own driver, which results in up to six identical power stages (for a three DoF stereo camera system). By redesigning the electronics, redundant parts could be omitted and a more compact design could be achieved.

For the development of the camera orientation systems also custom–made parts were used, which were manufactured utilizing high precision CNC–machining. In addition, for the setup of the kinematics, fixtures and assembling jigs were utilized. Finally, the camera orientation devices were calibrated altogether with the eye–tracker. The applied procedure is described in [93]. However, by direct manipulator calibration, the entire system accuracy could be improved. Thus, approaches which require external measurement setups as well as approaches which utilize system mounted cameras should be investigated.

In addition the kinematic parameters could be varied, so that the manipulators can be used for other duties, such as wrist joints for robotic applications, tool holders in CNC machines, or orientation systems for bigger cameras. Based on our kinematic models, the workspace of the devices can be optimized, with respect to the overall size, potential singularities, and quantization errors. The expected actuator forces can be calculated using our dynamic models. Thus, for further applications the design optimization and comparison of different kinematic parameters as well as actuators can be effectively handled.

At present, a camera including the CCD chip, the lens, and the complete electronic unit is aligned with the human line of sight. Using so–called “remote camera heads”, see e.g. [85], where the CCD chip is separated from the electronics, the mass and the size of the movable parts can be reduced. Thus, a more compact camera orientation system can be achieved. Employing further e.g. HDTV chips could lead to images with a higher resolution.

Besides to these technical improvements it is also important to continue and enhance the collaboration with project partners. Thus, possible new application scenarios like the calibration and examination of eye–trackers as well as an eye movement simulator for oculist education should be investigated. In both cases dedicated setups based on the presented camera orientation systems which reproduce natural (and pathological) eye movements could be used. In doing so, it should be possible to improve the quality of the eye–trackers/education while reducing the arising expenses.

A. Derivation of Kinematic Solutions

The nonlinear relation between actuator positions and camera orientation is calculated to determine and optimize the workspace and also to set up the closed loop control architectures. According to [97] the direct kinematic solution of a serial robot is usually rather easy to calculate analytically, while an analytic solution of the inverse kinematics is not available in general. For parallel robots the situation is vice versa. Thus, first the inverse kinematic solution is solved analytically, followed by the calculation of the direct kinematic problem. The relations are described using a vector matrix notation. Accounting for the kinematic parameters, the derived models are adapted to different configurations.
In the first section of this chapter we present the calculations considering systems with two DoF. In the second section the calculations concerning the system with three DoF are introduced.

A.1. Camera Orientation Systems with two DoF

In this section a detailed derivation of the inverse kinematic solution is presented. The joint operating range limitations are considered, too. Furthermore, two direct kinematic solutions are introduced and compared with each other. As mentioned before, we use a vector matrix notation to derive the nonlinear relations between the camera orientation and the actuator positions. Accounting for the kinematic parameters, the derived models are adapted to different configurations. To adjust the mono camera system to the human head an elevation angle is introduced between the actuator unit and the camera's frame and considered in the calculations. Since the actuator unit and the camera frame are in line for the stereo camera system the angle is zero.
To determine the camera orientation from given actuator positions the direct kinematic solution is required. We introduce two different procedures: a fully and a semi numerical approach. A detailed derivation is illustrated and subsequently the two approaches are compared.

A.1.1. Inverse Kinematics

In Figure A.1 the kinematic scheme of the investigated camera orientation system with two DoF and the nomenclature used for the following calculations is presented. Both coordinate systems introduced have their origin in the gimbal joint center. $\boldsymbol{S}_0$ denotes the base coordinate system and $\boldsymbol{S}_{Cam}$ the camera fixed coordinate system.

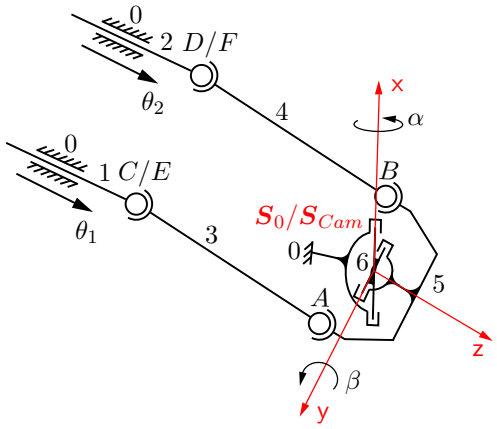

Figure A.1.: Kinematic scheme of the system with two DoF.

In Figure A.1 the mechanism is presented in its neutral position with all angles (α, β) and all positions (θ_1, θ_2) equal to zero. In this case the two coordinate systems correspond and the z–axes coincide with the cameras optical axis. All y–axes face to the right and the x–axes upwards.
With two constant vectors the spherical joint center points A and B can be described in the coordinate system $\boldsymbol{S}_{Cam}$ attached to the camera as follows:

$$ {}_{Cam}\boldsymbol{a} = [{}_{Cam}a_x,\ {}_{Cam}a_y,\ {}_{Cam}a_z]^T, \tag{A.1} $$

$$ {}_{Cam}\boldsymbol{b} = [{}_{Cam}b_x,\ {}_{Cam}b_y,\ {}_{Cam}b_z]^T. \tag{A.2} $$

The constant vectors can be transformed into the base coordinate system $\boldsymbol{S}_0$ using a homogeneous rotation matrix. Since for the gimbal joint a Fick configuration is chosen, the sequence of rotation is x–y(–z). Therefore, Kardan angels are used to describe the rotation matrix [108]:

$$ {}^0\boldsymbol{R}_{Cam} = \begin{bmatrix} \cos(\beta) & 0 & \sin(\beta) \\ \sin(\alpha)\sin(\beta) & \cos(\alpha) & -\sin(\alpha)\cos(\beta) \\ -\cos(\alpha)\sin(\beta) & \sin(\alpha) & \cos(\alpha)\cos(\beta) \end{bmatrix}, \tag{A.3} $$

where α denotes the rotation around the camera's vertical (pan) and β denotes the rotation around the camera's horizontal (tilt) axis. Note that for the chosen workspace the rotation matrix is free from singularities. After applying the transformation (A.1) and (A.2) can be written as:

$$ {}_0\boldsymbol{a} = {}^0\boldsymbol{R}_{Cam}\,{}_{Cam}\boldsymbol{a} = [{}_0a_x,\ {}_0a_y,\ {}_0a_z]^T, \tag{A.4} $$

$$ {}_0\boldsymbol{b} = {}^0\boldsymbol{R}_{Cam}\,{}_{Cam}\boldsymbol{b} = [{}_0b_x,\ {}_0b_y,\ {}_0b_z]^T. \tag{A.5} $$

The two spherical joint center points E and F attached to the prismatic joints can be described with the following vectors:

$$ {}_0\boldsymbol{e} = [{}_0c_x - \theta_1\sin(\xi),\ {}_0c_y,\ {}_0c_z + \theta_1\cos(\xi)]^T, \tag{A.6} $$

$$ {}_0\boldsymbol{f} = [{}_0d_x - \theta_2\sin(\xi),\ {}_0d_y,\ {}_0d_z + \theta_2\cos(\xi)]^T, \tag{A.7} $$

where ${}_0c_i$ and ${}_0d_i$ $(i = x, y, z)$ are the components of the constant vectors ${}_0\boldsymbol{c}$ and ${}_0\boldsymbol{d}$ describing the actuators' neutral position. The displacements are denoted with θ_1 for the first and with θ_2 for the second actuator. ξ denotes the constant elevation angle between the z–axis of the base coordinate system and the actuator unit, see Figure A.2. As mentioned in the case of the mono camera setup this inclination is necessary to fit the camera orientation system to a human head. For the stereo camera setup this angle is zero. To achieve a symmetrical design the push rods

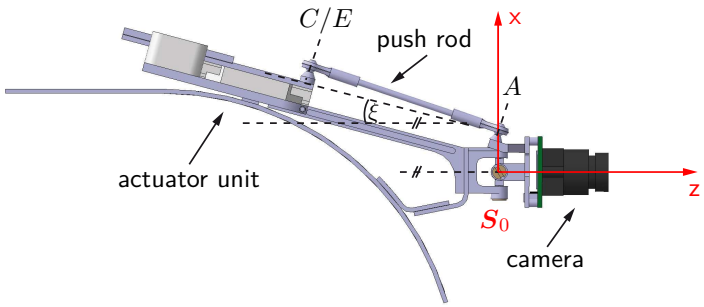

Figure A.2.: Side view of the mono camera orientation system.

connecting the points A and E as well as B and F respectively are equal. The constant length l of the first push rod is described as follows:

$$l^2 = |{}_0\boldsymbol{a} - {}_0\boldsymbol{e}|^2. \tag{A.8}$$

With the following abbreviations:

$$\begin{aligned} \Delta x_1 &= {}_0a_x - {}_0c_x, \\ \Delta y_1 &= {}_0a_y - {}_0c_y, \\ \Delta z_1 &= {}_0a_z - {}_0c_z, \\ \Delta l_1^2 &= l^2 - \Delta x_1^2 - \Delta y_1^2 - \Delta z_1^2, \end{aligned} \tag{A.9}$$

Equation (A.8) can be written as:

$$\begin{aligned} \Delta l_1^2 = {} & 2\Delta x_1 \theta_1 \sin(\xi) + \theta_1^2 \sin^2(\xi) \\ & - 2\Delta z_1 \theta_1 \cos(\xi) + \theta_1^2 \cos^2(\xi). \end{aligned} \tag{A.10}$$

After solving this quadratic equation θ_1 can be calculated as:

$$\begin{aligned} \theta_{1_{1,2}} = {} & \Delta z_1 \cos(\xi) - \Delta x_1 \sin(\xi) \\ & \overset{(+)}{-} \sqrt{(\Delta x_1 \sin(\xi) - \Delta z_1 \cos(\xi))^2 + \Delta l_1^2}. \end{aligned} \tag{A.11}$$

By simply replacing the vectors $\boldsymbol{a}$ with $\boldsymbol{b}$, $\boldsymbol{c}$ with $\boldsymbol{d}$ and $\boldsymbol{e}$ with $\boldsymbol{f}$ in (A.8) and (A.9) the solution for θ_2 can be written:

$$\begin{aligned} \theta_{2_{1,2}} = {} & \Delta z_2 \cos(\xi) - \Delta x_2 \sin(\xi) \\ & \overset{(+)}{-} \sqrt{(\Delta x_2 \sin(\xi) - \Delta z_2 \cos(\xi))^2 + \Delta l_2^2}. \end{aligned} \tag{A.12}$$

Due to the piezo–actuator travel range limitations

$$|\theta_1| \leq \theta_{max},$$
$$|\theta_2| \leq \theta_{max}, \tag{A.13}$$

where θ_{max} denotes the maximum piezo–actuator travel range, only one solution is possible. Considering the kinematic structure the "plus sign" in both (A.11) and (A.12) must be written in brackets, because it belongs to the assembly variation disregarded in this thesis.
Since the elevation angle ξ is zero for the stereo camera setup, (A.11) and (A.12) are simplified to:

$$\theta_{1_{stereo}} = \Delta z_1 - \sqrt{\Delta z_1^2 + \Delta l_1^2}, \tag{A.14}$$
$$\theta_{2_{stereo}} = \Delta z_2 - \sqrt{\Delta z_2^2 + \Delta l_2^2}. \tag{A.15}$$

With (A.11) and (A.12) for the mono camera system, as well as (A.14) and (A.15) for the stereo camera system respectively, the theoretically needed actuator set points can be calculated by given camera orientation angles. However, due to the mechanical constraints it is not possible to reach every desired orientation with the systems. Besides the limited actuator travel range also the used gimbal and spherical joints have a limited workspace. To determine the real camera orientation system workspace these limitations must be considered.

A.1.2. Joint Restrictions

In this section we present the influence of the joint limitations on the workspace. Considering the actuator travel range restrictions is quite simple. The required actuator positions must fulfill condition (A.13) otherwise the desired orientation angles are out of range.

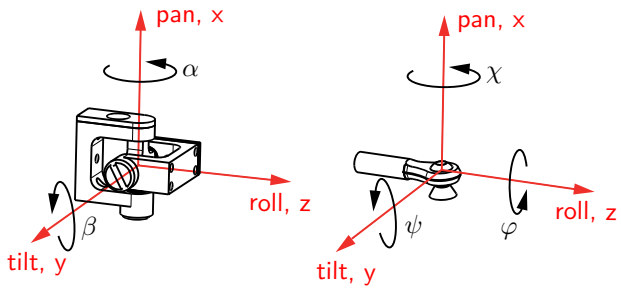

Figure A.3.: Gimbal joint (left), push rod spherical joint (right).

Furthermore, the limitation of the gimbal and spherical joints, used in the presented design, are taken into account. On the left side of Figure A.3 the gimbal joint is indicated. This custom made joint is mounted in the origin of the base coordinate system. Therefore, it will be oriented in the same direction as the camera. The

maximum deflection in both the pan and the tilt orientation can be achieved independently. These relations are described as follows:

$$|\alpha| \leq O_{GJmax},$$
$$|\beta| \leq O_{GJmax}, \tag{A.16}$$

where α describes orientations around the pan axis and β around the tilt axis. O_{GJmax} describes the maximum reachable orientation angle of the gimbal joint. The deflections (± 42 deg, see Table 3.6) provided by the joint are larger than the maximum desired ones (about ± 30 deg). Therefore, the achievable workspace is not restricted by the gimbal joint.
In Figure A.3 (right) the spherical joint attached to the push rods is introduced. The orientation around the vertical axis (pan) is described by the angle χ, around the diagonal axis (tilt) by the angle ψ and around the longitudinal axis (roll) by the angle φ.
Due to the elevation angle between the camera and the actor unit (for the mono camera), an initial spherical joint deflection arises. Thus, they are not in the middle of their operating range. Of course the initial deflection depends on the geometrical parameters, e.g. the push rods' length. To maximize the camera orientation workspace these deflections are calculated in the mechanism's neutral position and compensated in the first step. In the next step the spherical joint deflections are calculated over the entire workspace and their limitations are considered.
For this reason a set of new coordinate systems is introduced in the push rod spherical joint attachment points. E.g. in point A two such systems have their origin, see Figure A.4. The z–axis of the solid coordinate system $\boldsymbol{S}_A$ coincides with the vector connecting the points E and A. The y–axis points to the right and the x–axis coincides with the axis of the screw used to fix the spherical joint. Note that the screw axis lies in the camera's xz–plane. The second coordinate system in Figure A.4 is dashed and corresponds to $\boldsymbol{S}_{A'}$. To gain this system from the coordinate system $\boldsymbol{S}_{Cam}$ attached to the camera only a translation is required.

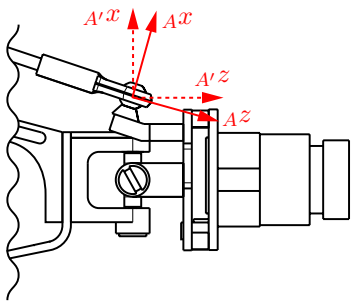

Figure A.4.: Introduced coordinate systems.

The vector from the point E to the point A of the first push rod ${}_{A'}\boldsymbol{l}_1$ is calculated as follows:

$${}_{A'}\boldsymbol{l}_1 = {}_{A'}\boldsymbol{a} - {}_{A'}\boldsymbol{e}. \tag{A.17}$$

Since the point A lies in the origin of the coordinate system the vector ${}_{A'}\boldsymbol{a}$ is zero. The vector ${}_{A'}\boldsymbol{e}$ to the point E is obtained by:

$$ {}_{A'}\boldsymbol{e} = {}^{Cam}\boldsymbol{R}_0 \, {}_0\boldsymbol{e} - {}_{Cam}\boldsymbol{a}, \tag{A.18} $$

where ${}_0\boldsymbol{e}$ is transformed from the base to the camera system with the rotation matrix ${}^{Cam}\boldsymbol{R}_0$, gained by transposing of (A.3). This vector is transformed into the system $\boldsymbol{S}_{A'}$ considering the translations ${}_{Cam}\boldsymbol{a}$, see (A.4). To obtain the initial tilt deflection ψ'_A the intersection angle between the vector of the first push rod ${}_{A'}\boldsymbol{l}_1$ and the unit vector of $\boldsymbol{S}_{A'}$ in x–axis is calculated:

$$ \psi'_A = \arccos\left(\frac{{}_{A'}\boldsymbol{l}_1 \, {}_{A'}\boldsymbol{e}_1}{|{}_{A'}\boldsymbol{l}_1| \, |{}_{A'}\boldsymbol{e}_1|}\right) - \frac{\pi}{2}. \tag{A.19} $$

By substitution of ${}_{A'}\boldsymbol{l}_1$ and ${}_{A'}\boldsymbol{e}_1$ in (A.19) the initial tilt deflections of the remaining spherical joints are calculated. Due to the selected design the initial pan and roll deflections of the spherical joints for both the mono and the stereo system are zero. Since in the case of the stereo camera system the actor unit and the camera frame are aligned in the home position, the initial tilt deflections are also zero.
With the calculations presented it is possible to determine the initial spherical joint deflection. To maximize the workspace the spherical joint attachment points are rotated, see Figure A.4.
While the pan operation range of the used joints is free of limitations the tilt and the roll orientation are restricted. Therefore, these two angles are considered in the workspace calculations. The tilt orientation ψ_A of the spherical joint in point A is described by the intersection angle between the x–axis ${}_A\boldsymbol{e}_1$ of the push rod spherical joint coordinate system $\boldsymbol{S}_A$ and the push rod itself.

$$ \psi_A = \arccos\left(\frac{{}_A\boldsymbol{l}_1 \, {}_A\boldsymbol{e}_1}{|{}_A\boldsymbol{l}_1| \, |{}_A\boldsymbol{e}_1|}\right) - \frac{\pi}{2}. \tag{A.20} $$

Note that the vector describing the first push rod ${}_A\boldsymbol{l}_1$ must be transformed from the system $\boldsymbol{S}_{A'}$ to $\boldsymbol{S}_A$ using the rotational matrix:

$$ {}^{A}\boldsymbol{R}_{A'} = \left(Rot({}_{A'}y, \psi'_A)\right)^T, \tag{A.21} $$

where ψ'_A describes a rotation around the y–axis of the system $\boldsymbol{S}_{A'}$.
As mentioned before the spherical joints provide only a limited working range around the roll axis. Hence, these orientations must be considered. The spherical joints are attached to the push rods. So calculating the roll deflection of the push rods yields the joints' roll orientation. This deflection corresponds to the intersection angles between the normal vectors on the yz–plane of the spherical joint coordinate systems. The following calculations are carried out for the first push rod. Thus, the normal vector on the yz–plane of the coordinate systems $\boldsymbol{S}_E$, ${}_E\boldsymbol{e}_1$, is transformed in the coordinate system $\boldsymbol{S}_A$ and then projected on the xy–plane.

$$ {}_A\boldsymbol{n}_E = {}^{A}\boldsymbol{R}_{A'} \, {}^{A'}\boldsymbol{R}_{Cam} \, {}^{Cam}\boldsymbol{R}_0 \, {}^{0}\boldsymbol{R}_E \, {}_E\boldsymbol{e}_1. \tag{A.22} $$

${}^{A}\boldsymbol{R}_{A'}$ describes the rotational matrix from the system $\boldsymbol{S}_{A'}$ to $\boldsymbol{S}_{A}$, see (A.21). Transposing (A.3) ${}^{Cam}\boldsymbol{R}_{0}$ is gained. Finally ${}^{0}\boldsymbol{R}_{E}$ is calculated:

$$ {}^{0}\boldsymbol{R}_{E} = Rot({}_{E'}y, \psi'_{E}), \tag{A.23} $$

where ψ'_E describes a rotation around the y–axis of the system $\boldsymbol{S}_{E'}$. The intersection angle between the two normal vectors φ_{AE} corresponds to the roll deflection of the push rod joints between the points A and E:

$$ \varphi_{AE} = \arccos\left(\frac{{}_{A}\boldsymbol{n}_{Exy}\,{}_{A}\boldsymbol{e}_{1}}{|{}_{A}\boldsymbol{n}_{Exy}|\,|{}_{A}\boldsymbol{e}_{1}|}\right). \tag{A.24} $$

Due to the kinematic structure the roll deflection of the push rods is distributed on two spherical joints. The roll deflection of the single joint can therefore be calculated by dividing (A.24) by two. The calculation of the roll deflection of the remaining push rod joints is done by substituting the normal vectors in (A.24).
Due to the design of the spherical joint, the achievable orientation around the tilt axis depends on the roll orientation (and vice versa). These relations are described as follows:

$$ \left|\sqrt{\psi_i^2 + \varphi_i^2}\right| \leq O_{PRmax}, \qquad i = A, B, E, F, \tag{A.25} $$

where ψ denotes orientations around the tilt and φ orientations around the roll axes. The maximum achievable orientation with the spherical joints attached to the push rod is denoted with O_{PRmax}.

To recapitulate: Using (A.11) and (A.12) the desired actuator set points can be calculated by given camera orientation angles. For these angles the limited operating range of the used joints is considered by (A.13), (A.16) and (A.25). If these conditions are not fulfilled, the desired orientation angles are out of range.

A.1.3. Direct Kinematics

As mentioned before, solving the direct kinematics of a parallel manipulator analytically can be difficult. Thus, in a first step a numeric solution, based on an iterative Newton–Raphson algorithm, has been derived. Hereby we used an approach according to [72].

Algorithm 1 Fully numerical direct kinematics.

1: Estimate the initial value of the orientation angles $\boldsymbol{w}_0$
2: **while** $|\boldsymbol{q} - \boldsymbol{q}_k| < \epsilon$ **do**
3: Calculate the corresponding joint values $\boldsymbol{q}_k$ using (3.2)
4: Determinate the new orientation values: $\boldsymbol{w}_{k+1} = \boldsymbol{J}(\boldsymbol{w}_k)(\boldsymbol{q} - \boldsymbol{q}_k) + \boldsymbol{w}_k$
5: $k = k + 1$
6: **end while**
7: $\boldsymbol{w} = \boldsymbol{w}_k$

Utilizing this iterative method orientation angles $\boldsymbol{w}$, in the presented case α and β, can be calculated by given joint values $\boldsymbol{q}$, here θ_1 and θ_2. k denotes the iterative step counter and ϵ denotes the abort criterion. For the required orientation angles the developed camera orientation system workspace is free of singularities. Thus, the Jacobian $\boldsymbol{J}(\boldsymbol{w})$ can be calculated as follows:

$$\boldsymbol{J}(\boldsymbol{w}) = \left(\frac{\partial \boldsymbol{q}}{\partial \boldsymbol{w}}\right)^{-1} = \left(\frac{\partial \boldsymbol{g}(\boldsymbol{w})}{\partial \boldsymbol{w}}\right)^{-1}, \tag{A.26}$$

where $\boldsymbol{g}$ denotes the inverse kinematic solution, $\boldsymbol{w}$ the orientation angles and $\boldsymbol{q}$ the joint values. The drawback of this method is that the implementation is not very fast which could cause problems in real–time applications.
To reduce the computational effort we investigated different approaches to gain an analytically direct kinematics. They are reported in [25]. However, no complete solution was found. Based on our observations, a semi numerical method is introduced in the following. We calculate only one of the angles β numerically. The remaining angle α is calculated analytically. Thus, the computational amount is reduced.
Without loss of generality two scalars K_1 and K_2 can be defined:

$$K_1 = {}_0\boldsymbol{a}^T {}_0\boldsymbol{e} = \frac{\|{}_0\boldsymbol{a}\|^2 + \|{}_0\boldsymbol{e}\|^2 - l^2}{2}, \tag{A.27}$$

$$K_2 = {}_0\boldsymbol{b}^T {}_0\boldsymbol{f} = \frac{\|{}_0\boldsymbol{b}\|^2 + \|{}_0\boldsymbol{f}\|^2 - l^2}{2}, \tag{A.28}$$

where ${}_0\boldsymbol{a}$ describes the vector to the spherical joint center point A in the base coordinate system $\boldsymbol{S}_0$. Vectors to the points B, E and F are specified in the same way. l describes the constant push rods length between the points A and E respectively B and F, see Figure A.1. Utilizing (A.3), (A.6) as well as (A.7), (A.27) and (A.28) can be written as follows:

$$\begin{aligned} K_1 = {}& {}_{Cam}a_x \cos(\beta)[{}_0c_x - \theta_1 \sin(\xi)] \\ & + [{}_{Cam}a_x \sin(\alpha)\sin(\beta) + {}_{Cam}a_y \cos(\alpha)]\, {}_0c_y \\ & - [{}_{Cam}a_x \cos(\alpha)\sin(\beta) - {}_{Cam}a_y \sin(\alpha)] \\ & \cdot [{}_0c_z + \theta_1 \cos(\xi)], \end{aligned} \tag{A.29}$$

$$\begin{aligned} K_2 = {}& {}_{Cam}b_x \cos(\beta)[{}_0d_x - \theta_2 \sin(\xi)] \\ & + [{}_{Cam}b_x \sin(\alpha)\sin(\beta) + {}_{Cam}b_y \cos(\alpha)]\, {}_0d_y \\ & - [{}_{Cam}b_x \cos(\alpha)\sin(\beta) - {}_{Cam}b_y \sin(\alpha)] \\ & \cdot [{}_0d_z + \theta_2 \cos(\xi)], \end{aligned} \tag{A.30}$$

where the known and constant vectors are denoted by ${}_{Cam}\boldsymbol{a}$, ${}_{Cam}\boldsymbol{b}$, ${}_0\boldsymbol{c}$, ${}_0\boldsymbol{d}$ and the known and constant elevation angle by ξ. The unknown camera orientation is defined by the angles α and β. θ_1 and θ_2 describe the linear actuator positions, which can be measured with the optical encoders.

With the following abbreviations:

$$
\begin{aligned}
P_1 &= {}_{Cam}a_x \cos(\beta)[{}_0c_x - \theta_1 \sin(\xi)] - K_1,\\
P_2 &= {}_{Cam}b_x \cos(\beta)[{}_0d_x - \theta_2 \sin(\xi)] - K_2,\\
P_3 &= {}_{Cam}a_x \sin(\beta){}_0c_y + {}_{Cam}a_y[{}_0c_z + \theta_1 \cos(\xi)],\\
P_4 &= {}_{Cam}b_x \sin(\beta){}_0d_y + {}_{Cam}b_y[{}_0d_z + \theta_2 \cos(\xi)],\\
P_5 &= {}_{Cam}a_y\,{}_0c_y - {}_{Cam}a_x \sin(\beta)[{}_0c_z + \theta_1 \cos(\xi)],\\
P_6 &= {}_{Cam}b_y\,{}_0d_y - {}_{Cam}b_x \sin(\beta)[{}_0d_z + \theta_2 \cos(\xi)],
\end{aligned}
\tag{A.31}
$$

and by dividing (A.29) and (A.30) by $\cos(\alpha)$ these equations can be written as:

$$\frac{1}{\cos(\alpha)}P_1 + \tan(\alpha)P_3 + P_5 = 0, \tag{A.32}$$

$$\frac{1}{\cos(\alpha)}P_2 + \tan(\alpha)P_4 - P_6 = 0. \tag{A.33}$$

The divisions are feasible because the workspace in the pan orientation is less than $\pm 90\,\text{deg}$ and therefore $\cos(\alpha) \neq 0$ over the entire workspace. Multiplying (A.33) with $-\frac{P_1}{P_2}$ and adding to (A.32) leads to:

$$\tan(\alpha)\left(P_3 - \frac{P_1P_4}{P_2}\right) + P_5 + \frac{P_1P_6}{P_2} = 0. \tag{A.34}$$

Introducing further

$$
\begin{aligned}
A_1 &= \frac{P_1P_6}{P_2} + P_5,\\
A_2 &= \frac{P_1P_4}{P_2} - P_3,
\end{aligned}
\tag{A.35}
$$

results in:

$$\alpha(\beta) = \arctan\left(\frac{A_1}{A_2}\right). \tag{A.36}$$

Since $A_1 \neq 0$ and $A_2 \neq 0$ can not be guaranteed in the entire workspace, a case differentiation must be made:

$$
\alpha(\beta) = \begin{cases}
\arctan\left(\frac{A_1}{A_2}\right), & A_2 \neq 0,\\
+\frac{\pi}{2}, & A_1 > 0 \wedge A_2 = 0,\\
-\frac{\pi}{2}, & A_1 < 0 \wedge A_2 = 0,\\
\text{not def.}, & A_1 = A_2 = 0.
\end{cases}
\tag{A.37}
$$

Using (A.37) the pan orientation α can be calculated analytically by given actuator positions (θ_1 and θ_2) and the tilt orientation β.
The unknown tilt orientation must be calculated numerically. Thus, we derived a function $f(\beta)$ which depends only on the actuator positions, on the tilt angle, and

on known constants. Inserting (A.36) in (A.33) results in

$$\frac{1}{\cos\left(\arctan\left(\frac{A_1}{A_2}\right)\right)}P_2 + \frac{A_1}{A_2}P_4 - P_6 = 0. \tag{A.38}$$

With the use of:

$$\frac{1}{\cos\left(\arctan\left(\frac{A_1}{A_2}\right)\right)} = \pm\sqrt{1+\left(\frac{A_1}{A_2}\right)^2} = \pm\frac{1}{|A_2|}\sqrt{A_1^2+A_2^2}, \tag{A.39}$$

and considering that the workspace in the pan orientation is less than ±90 deg, so that only positive roots of (A.39) must be considered, the roots of (A.38) can be calculated. Due to the $|A_2|$ term in (A.39) a case differentiation must be made here as well, which finally leads to:

$$f(\beta) = \begin{cases} +P_1\sqrt{A_1^2+A_2^2} + P_4A_1 - P_6A_2, & A_2 \geq 0, \\ -P_1\sqrt{A_1^2+A_2^2} + P_4A_1 - P_6A_2, & A_2 < 0. \end{cases} \tag{A.40}$$

By applying an iterative Newton–Raphson algorithm on (A.40), the tilt angle can be calculated numerically. Using this tilt value as input for (A.37), the pan angle can be calculated.

A.1.4. Comparison of Direct Kinematics

To determine the accuracy and the calculation time of the direct kinematic solutions presented the two introduced approaches are implemented using *Matlab/Simulink Real Time Workshop* from *The MathWorks* on a rapid prototyping real time processing board, *DS 1103 PPC* from *dSPACE*. In addition a user interface and a data acquisition tool are implemented based on this rapid prototyping environment. Since most of the developed controllers are running with a sampling rate of 1.0 kHz, also the experiments presented here are performed with this sampling rate.
Figure A.5 illustrates the architecture used for the evaluation. Camera orientation angles $\boldsymbol{w}$ are transformed to linear positions $\boldsymbol{q}$ with the analytical inverse kinematic solution. These linear positions are then re–transformed to camera orientations $\hat{\boldsymbol{w}}$ with one of the two direct kinematic solutions. The overall error is derived from the difference between the given and the calculated camera orientation using the $\mathcal{L}_2$–norm.

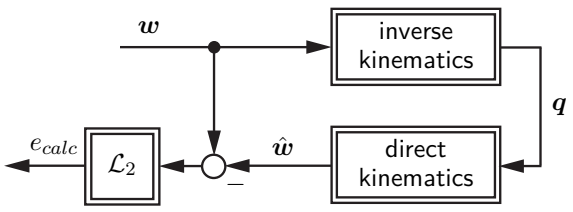

Figure A.5.: Calculation of the direct kinematic solution error.

During the experiments square pulse movements with a frequency of 2.0 Hz are used to imitate saccads. They can be considered as the fastest human eye movements. Sinusoidal movements with a frequency of 0.5 Hz are used to imitate smooth pursuit eye movements. Simulations reveal that simultaneous movements around both axes are the most challenging. Thus, further investigations concentrate on this motion pattern. To cover nearly the entire workspace movements with an amplitude of ± 29 deg are used. In Table A.1 the worst case calculation error e_{calc} and the worst case calculation time t_{calc} are reported for both the mono and the stereo camera system.

Table A.1.: Calculation error: direct kinematic solution.

Approach	Eye movements	Mono camera system		Stereo camera system	
		t_{calc} [s]	e_{calc} [deg]	t_{calc} [s]	e_{calc} [deg]
Fully	Saccads	$347 \cdot 10^{-6}$	$0.08 \cdot 10^{-12}$	$139 \cdot 10^{-6}$	$0.03 \cdot 10^{-12}$
numerical:	Smooth pursuit	$152 \cdot 10^{-6}$	$0.7 \cdot 10^{-12}$	$72 \cdot 10^{-6}$	$0.05 \cdot 10^{-12}$
Semi	Saccads	$29 \cdot 10^{-6}$	$0.1 \cdot 10^{-12}$	$23 \cdot 10^{-6}$	$0.006 \cdot 10^{-12}$
numerical:	Smooth pursuit	$24 \cdot 10^{-6}$	$9.4 \cdot 10^{-12}$	$20 \cdot 10^{-6}$	$22 \cdot 10^{-12}$

Applying the semi numerical approach, in the case of the mono camera system, yields a solution ten times faster compared to a fully numerical approach. However, the fully numerical solution is more then ten times more accurate. A similar behavior can be observed for the stereo camera system. In this case the semi numerical solution is faster but less accurate too. Note that the mean quantization error of the camera orientation devices presented is about 0.045 deg. The calculation errors of all direct kinematic solutions are much smaller. Thus, the calculations errors can be neglected. Due to the smaller calculation amount, the semi numerical direct kinematic solutions suit applications where high computational load must be avoided, e.g. when more cameras should be oriented contemporaneously.
Table A.1 suggests that the errors arising for the fully numerical approach in the case of the stereo camera system are smaller than they are for the mono camera system. In the latter design an elevation angle between the actuator unit and the camera frame is introduced. So the device is adapted to the human head. A possible explanation is that this supplementary angle implicates additional rounding errors. Furthermore, it can be observed, that if the semi numerical approach is applied to slow movements, higher errors emerge for the stereo camera configuration. Note that the semi numerical direct kinematic solution is developed and optimized for the mono camera system. By changing the kinematic parameters the algorithm is adapted, but not optimized, for the stereo camera system. This results in higher calculation errors. Since the absolute error is very small compared to the worst quantization error, this behavior is not further investigated.

A.2. Camera Orientation Systems with three DoF

In this section a detailed derivation of the inverse and direct kinematic solution for the three DoF camera orientation system is introduced. As for the two DoF devices, the operating range limitations of the joints are considered also for this system. A vector matrix notation is used to derive the nonlinear relations between the camera orientation and the actuator positions. So the models can be adapted to different configurations accounting for the kinematic parameters.

A.2.1. Inverse Kinematics

Figure A.6 reveals the kinematic scheme of the camera orientation system with three DoF and the nomenclature used for the following calculations. Note that for a better overview the tension springs are omitted.

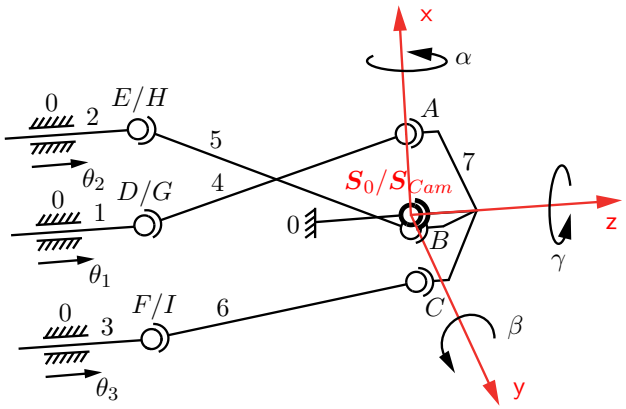

Figure A.6.: Kinematic scheme of the system with three DoF.

Both coordinate systems introduced have their origin in the main spherical joint center (bold in Figure A.6). $\boldsymbol{S}_0$ denotes the base coordinate system and $\boldsymbol{S}_{Cam}$ denotes the camera fixed coordinate system. Figure A.6 presents the mechanism in its neutral position with all camera angles and actuator positions equal to zero. In this case the two coordinate systems correspond and the z–axes coincide with the camera's optical axis. All y–axes face to the right and the x–axes upwards.
With three constant vectors the spherical joint center points A, B, and C can be described in the coordinate system $\boldsymbol{S}_{Cam}$ attached to the camera as follows:

$$ {}_{Cam}\boldsymbol{a} = [{}_{Cam}a_x,\ {}_{Cam}a_y,\ {}_{Cam}a_z]^T, \tag{A.41} $$

$$ {}_{Cam}\boldsymbol{b} = [{}_{Cam}b_x,\ {}_{Cam}b_y,\ {}_{Cam}b_z]^T, \tag{A.42} $$

$$ {}_{Cam}\boldsymbol{c} = [{}_{Cam}c_x,\ {}_{Cam}c_y,\ {}_{Cam}c_z]^T. \tag{A.43} $$

The constant vectors can be transformed into the base coordinate system $\boldsymbol{S}_0$ with the use of the homogeneous rotation matrix:

$$ {}^0\boldsymbol{R}_{Cam} = (Rot({}_{Cam}z, \gamma) Rot({}_{Cam}y, \beta) Rot({}_{Cam}x, \alpha))^T, \tag{A.44} $$

where α denotes the rotation around the camera's vertical axis (${}_{Cam}x$, pan), β denotes the rotation around the horizontal axis (${}_{Cam}y$, tilt) and γ denotes the rotation around the longitudinal axis (${}_{Cam}z$, roll). Since the sequence of rotation is x–y–z KARDAN angels are used to describe the rotation matrix [108]. After this transformation (A.41), (A.42), and (A.43) can be written as:

$$ {}_0\boldsymbol{a} = {}^0\boldsymbol{R}_{Cam\,Cam}\boldsymbol{a} = [{}_0a_x,\, {}_0a_y,\, {}_0a_z]^T, \tag{A.45} $$
$$ {}_0\boldsymbol{b} = {}^0\boldsymbol{R}_{Cam\,Cam}\boldsymbol{b} = [{}_0b_x,\, {}_0b_y,\, {}_0b_z]^T, \tag{A.46} $$
$$ {}_0\boldsymbol{c} = {}^0\boldsymbol{R}_{Cam\,Cam}\boldsymbol{c} = [{}_0c_x,\, {}_0c_y,\, {}_0c_z]^T. \tag{A.47} $$

The spherical joint center points G, H, and I attached to the prismatic joints can be described with the following vectors:

$$ {}_0\boldsymbol{g} = [{}_0d_x,\, {}_0d_y,\, {}_0d_z + \theta_1]^T, \tag{A.48} $$
$$ {}_0\boldsymbol{h} = [{}_0e_x,\, {}_0e_y,\, {}_0e_z + \theta_2]^T, \tag{A.49} $$
$$ {}_0\boldsymbol{i} = [{}_0f_x,\, {}_0f_y,\, {}_0f_z + \theta_3]^T, \tag{A.50} $$

where ${}_0d_i$, ${}_0e_i$, and ${}_0f_i$ ($i = x, y, z$) are the components of the constant vectors ${}_0\boldsymbol{d}$, ${}_0\boldsymbol{e}$, and ${}_0\boldsymbol{f}$ describing the actuators' neutral position. The displacements are denoted with θ_1 for the first, with θ_2 for the second actuator as well as with θ_3 for the third actuator. To afford a symmetrical design the length l of all three push rods is equal. For the first push rod, between the points A and G, this length can be described as follows:

$$ l = |{}_0\boldsymbol{a} - {}_0\boldsymbol{g}|, \tag{A.51} $$

where ${}_0\boldsymbol{a}$ describes the vector to the point A and ${}_0\boldsymbol{g}$ to the point G. With the following abbreviations:

$$ \begin{aligned} \Delta x_1 &= {}_0a_x - {}_0d_x, \\ \Delta y_1 &= {}_0a_y - {}_0d_y, \\ \Delta z_1 &= {}_0a_z - {}_0d_z, \\ \Delta l_1^2 &= l^2 - \Delta x_1^2 - \Delta y_1^2 - \Delta z_1^2, \end{aligned} \tag{A.52} $$

Equation (A.51) can be written as:

$$ \Delta l_1^2 = \theta_1^2 - 2\Delta z_1 \theta_1. \tag{A.53} $$

After solving this quadratic equation θ_1 can be calculated as:

$$ \theta_{1_{1,2}} = \Delta z_1 {}^{(}\pm{}^{)}\sqrt{\Delta z_1^2 + \Delta l_1^2}. \tag{A.54} $$

θ_2 and θ_3 can be calculated in the same way as θ_1 by simply replacing the vectors ${}_0\boldsymbol{a}$, ${}_0\boldsymbol{d}$, and ${}_0\boldsymbol{g}$ in (A.51) and (A.52). Thus, they are described as follows:

$$\theta_{2_{1,2}} = \Delta z_2 \, {}^{(}\pm{}^{)} \sqrt{\Delta z_2^2 + \Delta l_2^2}, \tag{A.55}$$

$$\theta_{3_{1,2}} = \Delta z_3 \, {}^{(}\pm{}^{)} \sqrt{\Delta z_3^2 + \Delta l_3^2}. \tag{A.56}$$

Accounting for the piezo–actuator travel range limitations

$$|\theta_i| \leq \theta_{max}, \qquad i = 1,2,3, \tag{A.57}$$

where θ_{max} denotes the maximum piezo–actuator travel range, confirms that only one solution is possible. Considering the kinematic structure the "plus sign" in (A.54)–(A.56) must be written in brackets, because it belongs to the assembly variation disregarded in this thesis.
Using (A.54)–(A.56) the theoretically needed actuator set points can be calculated by given camera orientation angles. However, due to the mechanical constraints it is not possible to reach every desired orientation with the system. Besides the limited actuator travel range also the spherical joints used have a limited workspace. To determine the real camera orientation system workspace these limitations must be considered.

A.2.2. Joint Restrictions

In this section the influence of the joint limitations on the workspace is presented. Considering the actuator travel range restrictions is quite simple. The required actuator positions must fulfill condition (A.57) otherwise the desired orientation angles are out of range.

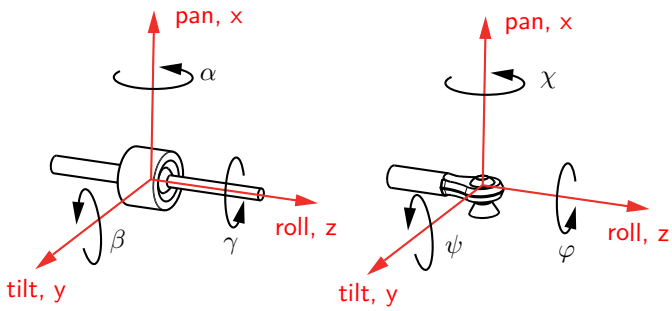

Figure A.7.: Main spherical joint (left), push rod spherical joint (right).

Furthermore, the limitation of the two different types of spherical joints used in the presented design is taken into account. On the left side of Figure A.7 the main spherical joint is shown. This joint is mounted in the origin of the base coordinate system. Thus, it will be oriented in the same direction as the camera. The maximum

deflection in both the pan and the tilt orientation can be achieved independently. The roll orientation has no restrictions. These relations are described as follows:

$$|\alpha| \leq O_{Mmax},$$
$$|\beta| \leq O_{Mmax}, \tag{A.58}$$

where α indicates the orientation around the pan axis and β around the tilt axis of the camera. O_{Mmax} denotes the maximum reachable orientation angle of the main spherical joint. The deflections provided by the joint ($\pm 35\,\text{deg}$, see Table 4.3) are greater than the maximum desired ones ($\pm 30\,\text{deg}$). Therefore, the achievable workspace is not restricted by the main spherical joint.
In Figure A.7 (right) a spherical joint attached to the push rods is illustrated. We denote the orientation around the vertical axis (pan) with χ, around the diagonal axis (tilt) with ψ, and around the longitudinal axis (roll) with φ. Depending on the parameter (e.g. the push rods length) chosen for the setup of the camera orientation system an initial spherical joint deflection arises. Thus, they are not in the in the middle of their operating range. To maximize the camera orientation workspace these initial deflections are calculated in the mechanism's neutral position and compensated in the first step. In the next step the spherical joint deflections are calculated over the entire workspace and their limitations are considered.
For this reason a set of new coordinate systems is introduced in the push rod spherical joint attachment points. E.g. in point A two such systems have their origin, see Figure A.8. The z–axis of the solid coordinate system $\boldsymbol{S}_A$ coincides with the vector connecting the points G and A. The y–axis points to the right and the x–axis coincides with the axis of the screw used to fix the spherical joint. To maximize the workspace the screw axis lies in the camera's xz–plane, see Section 4.4. The second coordinate system in Figure A.8 is dashed and corresponds to $\boldsymbol{S}_{A'}$. To gain this system from the camera attached coordinate system $\boldsymbol{S}_{Cam}$ besides a translation only a rotation around the camera's z–axis is required.

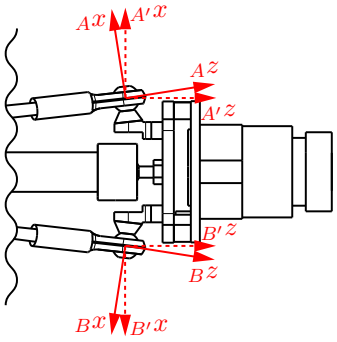

Figure A.8.: Introduced coordinate systems.

The vector from the point G to the point A of the first push rod ${}_{A'}\boldsymbol{l}_1$ is calculated as follows:

$${}_{A'}\boldsymbol{l}_1 = {}_{A'}\boldsymbol{a} - {}_{A'}\boldsymbol{g}. \tag{A.59}$$

Because the point A lies in the origin of the coordinate system the vector ${}_{A'}\boldsymbol{a}$ is zero. The vector ${}_{A'}\boldsymbol{g}$ to the point G is obtained by:

$$ {}_{A'}\boldsymbol{g} = {}^{A'}\boldsymbol{R}_{Cam} \left({}^{Cam}\boldsymbol{R}_{0\,0}\boldsymbol{g} - {}_{Cam}\boldsymbol{a} \right), \tag{A.60} $$

where ${}_0\boldsymbol{g}$ is transformed from the base to the camera system with the rotation matrix ${}^{Cam}\boldsymbol{R}_0$, gained from the transposing of (A.44). This vector is transformed into the system $\boldsymbol{S}_{A'}$ considering the translations ${}_{Cam}\boldsymbol{a}$ (A.45) and the rotations matrix ${}^{A'}\boldsymbol{R}_{Cam}$. The latter describes a rotation around the camera's z–axis by the angle $\upsilon_{A'}$, which describes the angle between the x–axis of the base coordinate system $\boldsymbol{S}_0$ and the x–axis of the coordinate system $\boldsymbol{S}_{A'}$ projected on the xy–plane. To obtain the initial pan deflection χ'_A the intersection angle between the vector of the first push rod projected on the yz–plane ${}_{A'}\boldsymbol{l}_{1yz}$ and the unit vector of $\boldsymbol{S}_{A'}$ in y–axis is calculated:

$$ \chi'_A = \arccos\left(\frac{{}_{A'}\boldsymbol{l}_{1yz}\,{}_{A'}\boldsymbol{e}_2}{|{}_{A'}\boldsymbol{l}_{1yz}|\,|{}_{A'}\boldsymbol{e}_2|} \right) - \frac{\pi}{2}. \tag{A.61} $$

By projecting the vector of the first push rod on the xz–plane ${}_{A'}\boldsymbol{l}_{1xz}$ the initial tilt deflection ψ'_A is calculated:

$$ \psi'_A = \arccos\left(\frac{{}_{A'}\boldsymbol{l}_{1xz}\,{}_{A'}\boldsymbol{e}_1}{|{}_{A'}\boldsymbol{l}_{1xz}|\,|{}_{A'}\boldsymbol{e}_1|} \right) - \frac{\pi}{2}. \tag{A.62} $$

By substitution of ${}_{A'}\boldsymbol{l}_{1yz}$ and ${}_{A'}\boldsymbol{e}_2$ as well as ${}_{A'}\boldsymbol{l}_{1xz}$ and ${}_{A'}\boldsymbol{e}_1$ in (A.61) and (A.62) the initial pan and tilt deflection of the remaining spherical joints is calculated.
To determine the initial roll deflection the intersection angle between the normal vectors on the yz–plane of the spherical joint coordinate systems is calculated. Hence, the following calculations are carried out for the first push rod, the normal vector on the yz–plane of the coordinate systems $\boldsymbol{S}_G$, ${}_G\boldsymbol{e}_1$, is transformed in the coordinate system $\boldsymbol{S}_A$ and then projected on the xy–plane.

$$ {}_A\boldsymbol{n}_G = {}^A\boldsymbol{R}_{A'}\,{}^{A'}\boldsymbol{R}_{Cam}\,{}^{Cam}\boldsymbol{R}_0\,{}^0\boldsymbol{R}_G\,{}_G\boldsymbol{e}_1, \tag{A.63} $$

where ${}^A\boldsymbol{R}_{A'}$ describes the rotational matrix from the system $\boldsymbol{S}_{A'}$ to $\boldsymbol{S}_A$ and is calculated as follows:

$$ {}^A\boldsymbol{R}_{A'} = \left(Rot({}_{A'}y, \psi'_A)\, Rot({}_Ax, \chi'_A) \right)^T. \tag{A.64} $$

χ'_A denotes a rotation around the x–axis of the coordinate system $\boldsymbol{S}_A$ and ψ'_A a rotation around the y–axis of the system $\boldsymbol{S}_{A'}$. ${}^{A'}\boldsymbol{R}_{Cam}$ describes a rotation around the camera's z–axis by the angle $\upsilon_{A'}$. Transposing (A.44) ${}^{Cam}\boldsymbol{R}_0$ is gained. Finally ${}^0\boldsymbol{R}_G$ is calculated:

$$ {}^0\boldsymbol{R}_G = Rot({}_0z, \upsilon_{G'})\, Rot({}_{G'}y, \psi'_G)\, Rot({}_Gx, \chi'_G), \tag{A.65} $$

where χ'_G describes a rotation around the x–axis of the system $\boldsymbol{S}_G$, ψ'_G a rotation around the y–axis of the system $\boldsymbol{S}_{G'}$ and $\upsilon_{G'}$ a rotation around the z–axis of the base

system. The latter describes the angle between the x–axis of the base coordinate system $\boldsymbol{S}_0$ and the x–axis of the coordinate system $\boldsymbol{S}_{G'}$ projected on the xy–plane. The intersection angle between the two normal vectors φ_{AG0} corresponds to the initial roll deflection of the push rod joints between the points A and G:

$$\varphi_{AG0} = \arccos\left(\frac{{}_A\boldsymbol{n}_{Gxy}\,{}_A\boldsymbol{e}_1}{|{}_A\boldsymbol{n}_{Gxy}|\,|{}_A\boldsymbol{e}_1|}\right). \tag{A.66}$$

The initial roll deflection calculation of the remaining push rod joints is done by substituting the normal vectors in (A.66).
With the presented calculations it is possible to determine the initial deflection of the spherical joints. To maximize the workspace they are arranged in an ideal home position. Therefore, all spherical joint attachment points are rotated, see Figure A.8, and the push rods are twisted respectively.
The selected spherical joints are free of limitations for rotations around the pan axis. However, deflections around the tilt and roll axes are bounded. Thus, these two angles are calculated over the entire workspace and considered in the calculations. The tilt orientation ψ_A of the spherical joint in point A is described by the intersection angle between the x–axis ${}_A\boldsymbol{e}_1$ of the push rod spherical joint coordinate system $\boldsymbol{S}_A$ and the push rod itself.

$$\psi_A = \arccos\left(\frac{{}_A\boldsymbol{l}_1\,{}_A\boldsymbol{e}_1}{|{}_A\boldsymbol{l}_1|\,|{}_A\boldsymbol{e}_1|}\right) - \frac{\pi}{2}. \tag{A.67}$$

The vector describing the first push rod ${}_A\boldsymbol{l}_1$ is transformed from the system $\boldsymbol{S}_{A'}$ to $\boldsymbol{S}_A$ using (A.64).
The current roll angle φ_{AG} of the first push rod is calculated by subtracting the initial deflection φ_{AG0} from (A.66) which leads to:

$$\varphi_{AG} = \arccos\left(\frac{{}_A\boldsymbol{n}_{Gxy}\,{}_A\boldsymbol{e}_1}{|{}_A\boldsymbol{n}_{Gxy}|\,|{}_A\boldsymbol{e}_1|}\right) - \varphi_{AG0}. \tag{A.68}$$

As mentioned before, each push rod is equipped with two spherical joints. Thus, the roll deflection of a single push rod is distributed onto these two joints. The orientation of a single joint is therefore gained dividing (A.68) by two. The calculation of the tilt and roll angles of the remaining spherical joints is straightforward.
However, not only the tilt and roll deflections are restricted, but their maximum working range depends on each other. This relation can be described as follows:

$$\begin{aligned}\left|\sqrt{\psi_i^2 + \varphi_i^2}\right| &\leq O_{CPRmax}, \qquad i = A,B,C,\\ \left|\sqrt{\psi_i^2 + \varphi_i^2}\right| &\leq O_{APRmax}, \qquad i = G,H,I,\end{aligned} \tag{A.69}$$

where ψ denotes orientations around the tilt and φ orientations around the roll axes. The maximum achievable orientation with the push rod attached spherical joints is denoted with O_{CPRmax} on the camera frame and with O_{APRmax} on the actuator side.

To recapitulate: Using (A.54)–(A.56) the desired actuator set points can be calculated from given camera orientation angles. The limited operating range of the used joints is considered by (A.57), (A.58), and (A.69). If these conditions are not fulfilled the desired orientation angles are out of range.

A.2.3. Direct Kinematics

For the camera orientation system with three DoF the direct kinematics is solved numerically. Hereby, we use the same algorithm as for the systems with two DoF, see Section A.1.3. The selected approach is based on an iterative Newton–Raphson algorithm [72] and is as follows:

Algorithm 2 Fully numerical direct kinematics.

1: Estimate the initial value of the orientation angles $\boldsymbol{w}_0$
2: **while** $|\boldsymbol{q} - \boldsymbol{q}_k| < \epsilon$ **do**
3: Calculate the corresponding joint values $\boldsymbol{q}_k$ using (4.2)
4: Determinate the new orientation values: $\boldsymbol{w}_{k+1} = \boldsymbol{J}(\boldsymbol{w}_k)(\boldsymbol{q} - \boldsymbol{q}_k) + \boldsymbol{w}_k$
5: $k = k + 1$
6: **end while**
7: $\boldsymbol{w} = \boldsymbol{w}_k$

Using this iterative method orientation angles $\boldsymbol{w}$, in the presented case α, β, and γ can be calculated by given joint values $\boldsymbol{q}$, here θ_1, θ_2, and θ_3. k denotes the iterative step counter and ϵ denotes the abort criterion. For the required orientation angles the developed camera orientation system workspace is free of singularities. Thus, the Jacobian $\boldsymbol{J}(\boldsymbol{w})$ can be calculated as follows:

$$\boldsymbol{J}(\boldsymbol{w}) = \left(\frac{\partial \boldsymbol{q}}{\partial \boldsymbol{w}}\right)^{-1} = \left(\frac{\partial \boldsymbol{g}(\boldsymbol{w})}{\partial \boldsymbol{w}}\right)^{-1}, \tag{A.70}$$

where $\boldsymbol{g}$ denotes the inverse kinematic solution, $\boldsymbol{w}$ the orientation angles and $\boldsymbol{q}$ the joint values.
Since the direct kinematics is calculated numerically the achieved results are not free of errors. However, as for the solutions introduced in Section A.1.3 in the case of the three DoF kinematics the errors are also very small. Thus, they are not further investigated.

B. Simplified Dynamic Model

To enable the development of model based controllers, the equations of motions are required. As illustrated in Chapter 3 and in Chapter 4 respectively multi–body models of the camera orientation devices are setup using *MBSim*. Based on the implemented description the tool is able to internally generate and evaluate the dynamic equations. However, due to the high computational cost the *MBSim* models can not be used for closed loop control. Thus, a simple analytical dynamic model is developed and verified exemplary for the mono camera orientation system in the following. The model is based on our observations reported in [2] which are also suitable for the other two camera orientation systems.
During modeling we considered the most important bodies of the mechanical system only. These are the camera (including the mounting frame) and the movable parts of the actuators. Other masses, e.g. the push rods connecting the actuators and the camera mounting frame are neglected. So the camera orientation system is approximated as a three mass system. For the following calculations we considered a fixed camera orientation system, which is not moved or tilted.

B.1. Derivation of Equations of Motion

We used the Lagrange formalism to determine the equation of motion. Figure B.1 introduces the kinematic scheme of the investigated camera orientation system and the nomenclature used for the calculations. The two coordinate systems, $\boldsymbol{S}_0$ and $\boldsymbol{S}_{Cam}$ have their origin in the gimbal joint center. Since the mechanism is in its neutral position, the two coordinate systems correspond and the z–axes coincide with the cameras optical axis. All y–axes face to the right and the x–axes upwards. The remaining two coordinate systems, $\boldsymbol{S}_{0_{A1}}$ and $\boldsymbol{S}_{0_{A2}}$, have their origin in the prismatic joints working range middle. The z–axes coincide with the joints free direction and as before the y–axes face to the right and the x–axes upwards.

The camera orientation systems' potential energy is as follows:

$$V = -m_C \, {}_0\boldsymbol{g}^T \, {}_0\boldsymbol{r}_{CoG} - m_{PJ} \, g \, \theta_1 \, \sin(\xi) - m_{PJ} \, g \, \theta_2 \, \sin(\xi), \tag{B.1}$$

where m_C depicts the mass of the camera and the camera mounting frame. The vector ${}_0\boldsymbol{g}$ describes the gravitational force direction. The camera (including the mounting frame) is a non uniform body. Therefore, the center–of–gravity (CoG) is determined using a CAD program. So the vector ${}_{Cam}\boldsymbol{r}_{CoG}$ from the origin of the camera attached coordinate system to the CoG is yield. While the camera can be oriented around two axes, the actuators can be moved only in one direction.

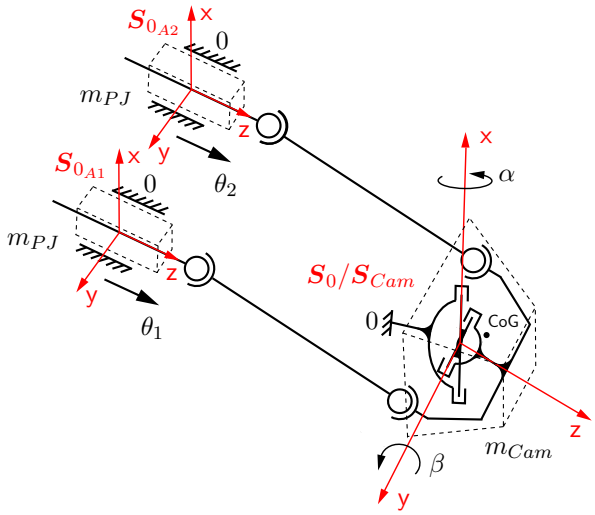

Figure B.1.: Three mass model, kinematic scheme.

Therefore, their contribution to the potential energy is calculated without using vectors. The mass of the movable parts of the actuators, the prismatic joint including the encoder stripes, is denoted with m_{PJ}. The actuators' displacement is denoted with θ_1 for the first and θ_2 for the second actuator. The angle ξ depicts the constant inclination between the z–axis of the base coordinate system and the actuator unit, see Figure A.2.
In the presented case the gravity operates in negative x–directions. Thus, the vector ${}_0\boldsymbol{g}$ is described as follows:

$$ {}_0\boldsymbol{g} = [-g\,0\,0]^T\,. \tag{B.2} $$

Using the homogeneous rotation matrix ${}^0\boldsymbol{R}_{Cam}$, see (A.3), the vector to the CoG can be transformed from the camera to the base coordinate system.

$$ {}_0\boldsymbol{r}_{CoG} = {}^0\boldsymbol{R}_{Cam}\,{}_{Cam}\boldsymbol{r}_{CoG} = \begin{bmatrix} x_{CoG}\,\cos(\beta) + z_{CoG}\,\sin(\beta) \\ x_{CoG}\,\sin(\alpha)\,\cos(\beta) - z_{CoG}\,\sin(\alpha)\,\cos\beta \\ -x_{CoG}\,\cos(\alpha)\,\sin\beta + z_{CoG}\,\cos(\alpha)\sin(\beta) \end{bmatrix}. \tag{B.3} $$

Due to the configuration of the camera the CoG is displaced along the x–axis, depicted with x_{CoG}, and along the z–axis, depicted with z_{CoG}. The displacement along the y–axis is so small that it can be neglected.
Using this information (B.1) is refined:

$$ V = m_{Cam}\,g\,(x_{CoG}\,\cos(\beta) + z_{CoG}\,\sin(\beta)) - m_{PJ}\,g\,\sin(\xi)\,(\theta_1 + \theta_2)\,. \tag{B.4} $$

Equation (B.4) reveals that the potential energy depends on the camera orientation, the linear actuator positions, and on known constants. Since we intend to setup a model based workspace control architecture, the joint space coordinates (θ_1 and θ_2) must be expressed by workspace coordinates (α and β). This can be done using the inverse kinematic solution (A.11) and (A.12). However, these analytical solutions

do not suit the application since they are nonlinear. To yield a linear relation we approximated the inverse kinematic with the following equations:

$$\theta_1 = c_{11}\alpha + c_{12}\beta,$$
$$\theta_2 = c_{21}\alpha + c_{22}\beta,$$

where c_{11} – c_{22} are constant values. Further information about the determination of the constants and the solution accuracy are presented in Section B.3.
Finally, the camera orientation systems' potential energy is given by:

$$V = m_{Cam}\, g\, (x_{CoG}\, \cos(\beta) + z_{CoG}\, \sin(\beta)) - m_{PJ}\, g\, \sin(\xi)\, (c_{11}\alpha + c_{12}\beta + c_{21}\alpha + c_{22}\beta)\,. \tag{B.5}$$

After that, the kinetic energy of the three mass system is determined.

$$T = \frac{1}{2}\, I_{Cam_{xx}}\, \dot{\alpha}^2 + \frac{1}{2}\, I_{Cam_{yy}}\, \dot{\beta}^2 + \frac{1}{2}\, m_{PJ} \left(\dot{\theta_1}^2 + \dot{\theta_2}^2 \right). \tag{B.6}$$

Using a CAD program the inertia tensor of the camera including the mounting frame is calculated. Because the moments of deviation are very small, compared to the principal moment of inertia, the former are neglected. Since the camera is oriented around two axes, only the first two principal moments of inertia $I_{Cam_{xx}}$ and $I_{Cam_{yy}}$ must be considered. For the kinetic energy the joint space coordinates are transformed to workspace coordinates too:

$$T = \frac{1}{2}\, I_{Cam_{xx}}\, \dot{\alpha}^2 + \frac{1}{2}\, I_{Cam_{yy}}\, \dot{\beta}^2 + \frac{1}{2}\, m_{PJ} \left(\left(c_{11}\, \dot{\alpha} + c_{12}\, \dot{\beta} \right)^2 + \left(c_{21}\, \dot{\alpha} + c_{22}\, \dot{\beta} \right)^2 \right). \tag{B.7}$$

In the next step the Lagrange equations are calculated:

$$\left[\frac{d}{dt} \left(\frac{\partial T}{\partial \dot{\boldsymbol{q}}} \right) \right]^T - \left[\frac{\partial T}{\partial \boldsymbol{q}} \right]^T + \left[\frac{\partial V}{\partial \boldsymbol{q}} \right]^T = \boldsymbol{Q}_{nc}, \tag{B.8}$$

with $\boldsymbol{q} = [\alpha, \beta]^T$ indicating the generalized coordinates and $\boldsymbol{Q}_{nc}$ the non conservative forces induced by the actuators. The single elements of the equation are as follows:

$$\frac{d}{dt} \left(\frac{\partial T}{\partial \dot{\alpha}} \right) = I_{Cam_{xx}}\, \ddot{\alpha} + m_{PJ}\, c_{11} \left(c_{11}\, \ddot{\alpha} + c_{12}\, \ddot{\beta} \right) + m_{PJ}\, c_{21} \left(c_{21}\, \ddot{\alpha} + c_{22}\, \ddot{\beta} \right), \tag{B.9}$$

$$\frac{d}{dt} \left(\frac{\partial T}{\partial \dot{\beta}} \right) = I_{Cam_{yy}}\, \ddot{\beta} + m_{PJ}\, c_{12} \left(c_{11}\, \ddot{\alpha} + c_{12}\, \ddot{\beta} \right) + m_{PJ}\, c_{22} \left(c_{21}\, \ddot{\alpha} + c_{22}\, \ddot{\beta} \right), \tag{B.10}$$

$$\frac{\partial T}{\partial \alpha} = 0, \qquad \frac{\partial T}{\partial \beta} = 0, \tag{B.11}$$

$$\frac{\partial V}{\partial \alpha} = -m_{PJ}\, g\, \sin(\xi)\, (c_{11} + c_{12})\,, \tag{B.12}$$

$$\frac{\partial V}{\partial \beta} = m_{Cam}\, g\, (-x_{CoG}\, \sin(\beta) + z_{CoG}\, \cos(\beta)) - m_{PJ}\, g\, \sin(\xi)\, (c_{12} + c_{22})\,. \tag{B.13}$$

The non conservative forces are exemplarily established for the first actuator.

$$\boldsymbol{Q}_{nc_1} = \left[\frac{\partial\, {}_{0_{A1}}\boldsymbol{v}_1}{\partial \dot{\boldsymbol{q}}}\right]^T {}_{0_{A1}}\boldsymbol{F}_{PJ_1}, \tag{B.14}$$

where the generalized coordinates are described with $\boldsymbol{q}$, the first actuator velocity is described with ${}_{0_{A1}}\boldsymbol{v}_1$, and the forces introduced in the mechanism with ${}_{0_{A1}}\boldsymbol{F}_{PJ_1}$. The actuator velocities and the forces are related to the first actuator's coordinate system $\boldsymbol{S}_{0_{A1}}$, see Figure B.1. Since the prismatic joint free direction coincides with the z–axes, the velocities and forces can be different from zero only in this direction.

$${}_{0_{A1}}\boldsymbol{v}_1 = \begin{bmatrix} 0 \\ 0 \\ \dot{\theta}_1 \end{bmatrix} = \begin{bmatrix} 0 \\ 0 \\ c_{11}\,\dot{\alpha} + c_{12}\,\dot{\beta} \end{bmatrix}, \tag{B.15}$$

$${}_{0_{A1}}\boldsymbol{F}_{PJ_1} = \begin{bmatrix} 0 \\ 0 \\ F_{A_1} - d\,\dot{\theta}_1 \end{bmatrix} = \begin{bmatrix} 0 \\ 0 \\ F_{A_1} - d\left(c_{11}\,\dot{\alpha} + c_{12}\,\dot{\beta}\right) \end{bmatrix}. \tag{B.16}$$

The forces induced in the first prismatic joint (and so in the mechanism) are denoted with $\boldsymbol{F}_{PJ_1}$ and the forces supplied by the actuators with F_{A_1}. Since the prismatic joint is not ideal, friction occurs which is considered by the damping coefficient d. Besides the friction of the joint this factor considers also the fact, that during higher velocities smaller forces can be provided by the actuators.
We use a sampling frequency of 1 kHz for the control architecture. As reported in Section 5.1 the power electronics is able to supply new desired actuator driving signals in about 0.7 ms even in the worst case. Due to the high dynamic response of the selected piezo–actuators it can be assumed that new desired forces are provided within one sampling interval. Thus, we neglected this short time delay and the non conservative forces are calculated as follows:

$$\boldsymbol{Q}_{nc_1} = \begin{bmatrix} c_{11}\,F_{A_1} - c_{11}\,d\,(c_{11}\,\dot{\alpha} + c_{12}\,\dot{\beta}) \\ c_{12}\,F_{A_1} - c_{12}\,d\,(c_{11}\,\dot{\alpha} + c_{12}\,\dot{\beta}) \end{bmatrix}, \tag{B.17}$$

$$\boldsymbol{Q}_{nc_2} = \begin{bmatrix} c_{21}\,F_{A_2} - c_{21}\,d\,(c_{21}\,\dot{\alpha} + c_{22}\,\dot{\beta}) \\ c_{22}\,F_{A_2} - c_{22}\,d\,(c_{21}\,\dot{\alpha} + c_{22}\,\dot{\beta}) \end{bmatrix}. \tag{B.18}$$

Introducing further the systems state vector:

$$[x_1\, x_2\, x_3\, x_4]^T = \left[\alpha\, \beta\, \dot{\alpha}\, \dot{\beta}\right]^T, \tag{B.19}$$

and by applying the small angle approximation to (B.13) the equation of motion can be formulated as:

$$\dot{x_1} = x_3, \tag{B.20}$$

$$\dot{x_2} = x_4, \tag{B.21}$$

$$
\begin{aligned}
\dot{x_3} = -(&c_{21}^2\, d\, x_3\, m_{pj}\, c_{12}^2 + c_{11}\, d\, c_{12}\, x_4\, I_{Cam_{yy}} - c_{21}\, F_{A_2}\, m_{pj}\, c_{12}^2 + c_{11}^2\, d\, x_3\, m_{pj}\, c_{22}^2 \\
&+ c_{21}\, d\, c_{22}\, x_4\, I_{Cam_{yy}} - c_{11}\, F_{A_1}\, m_{pj}\, c_{22}^2 + c_{11}^2\, d\, x_3\, I_{Cam_{yy}} + c_{21}^2\, d\, x_3\, I_{Cam_{yy}} \\
&+ m_{pj}\, c_{21}\, c_{22}\, c_{12}\, F_{A_1} - m_{pj}\, c_{21}\, c_{22}\, m_{Cam}\, g\, z_{CoG} + m_{pj}\, c_{21}\, c_{22}\, m_{Cam}\, g\, x_{CoG}\, x_2 \\
&+ m_{pj}\, c_{11}\, c_{12}\, m_{Cam}\, g\, x_{CoG}\, x_2 - m_{pj}\, c_{11}\, c_{12}\, m_{Cam}\, g\, z_{CoG} + m_{pj}\, c_{11}\, c_{12}\, c_{22}\, F_{A_2} \\
&- 2\, m_{pj}\, c_{11}\, c_{12}\, c_{22}\, d\, c_{21}\, x_3 - m_{pj}\, g\, \sin(\psi)\, c_{21}\, I_{Cam_{yy}} + m_{pj}^2\, c_{21}\, c_{12}\, g\, \sin(\psi)\, c_{22} \\
&+ m_{pj}^2\, c_{11}\, c_{12}\, g\, \sin(\psi)\, c_{22} - m_{pj}^2\, g \sin(\psi)\, c_{11}\, c_{22}^2 - m_{pj}\, g\, \sin(\psi)\, c_{11}\, I_{Cam_{yy}} \\
&- m_{pj}^2\, g\, \sin(\psi)\, c_{21}\, c_{12}^2 - c_{11}\, F_{A_1}\, I_{Cam_{yy}} - c_{21}\, F_{A_2}\, I_{Cam_{yy}}) \\
/(&- 2\, m_{pj}^2\, c_{11}\, c_{12}\, c_{22}\, c_{21} + I_{Cam_{xx}}\, m_{pj}\, c_{12}^2 + I_{Cam_{xx}}\, m_{pj}\, c_{22}^2 + m_{pj}\, c_{11}^2\, I_{Cam_{yy}} \\
&+ m_{pj}^2\, c_{11}^2\, c_{22}^2 + m_{pj}\, c_2 1^2\, I_{Cam_{yy}} + m_{pj}^2\, c_{21}^2\, c_{12}^2 + I_{Cam_{xx}}\, I_{Cam_{yy}}).
\end{aligned}
\tag{B.22}
$$

$$
\begin{aligned}
\dot{x_4} = -(&m_{pj}\, c_{12}\, c_{11}\, c_{21}\, F_{A_2} - 2\, m_{pj}\, c_{12}\, c_{11}\, c_{21}\, d\, c_{22}\, x_4 + m_{Cam}\, g z_{CoG}\, I_{Cam_{xx}} \\
&- c_{12}\, F_{A_1}\, m_{pj}\, c_{21}^2 + c_{12}^2\, d\, x_4\, I_{Cam_{xx}} - c_{22}\, F_{A_2}\, m_{pj}\, c_{11}^2 + c_{22}^2\, d\, x_4\, I_{Cam_{xx}} \\
&+ m_{pj}^2\, c_{22}\, c_{11}\, g\, \sin(\psi)\, c_{21} - m_{pj}\, g\, \sin(\psi)\, c_{12}\, I_{Cam_{xx}} - m_{pj}^2\, g\, \sin(\psi)\, c_{12}\, c_{21}^2 \\
&- m_{pj}\, g\, \sin(\psi)\, c_{22}\, I_{Cam_{xx}} - m_{pj}^2\, g\, \sin(\psi)\, c_{22}\, c_{11}^2 + m_{pj}^2\, c_{12}\, c_{11}\, g\, \sin(\psi)\, c_{21} \\
&+ c_{22}^2\, d\, x_4\, m_{pj}\, c_{11}^2 - m_{Cam}\, g\, x_{CoG}\, x_2\, I_{Cam_{xx}} - m_{Cam}\, g\, x_{CoG}\, x_2\, m_{pj}\, c_{11}^2 \\
&- m_{Cam}\, g\, x_{CoG}\, x_4\, m_{pj}\, c_{21}^2 + m_{Cam}\, g\, z_{CoG}\, m_{pj}\, c_{11}^2 \\
&+ m_{Cam}\, g\, z_{CoG}\, m_{pj}\, c_{21}^2\, c_{12}\, d\, c_{11}\, x_3\, I_{Cam_{xx}} + c_{12}^2\, d\, x_4\, m_{pj}\, c_{21}^2 + c_{22}\, d\, c_{21}\, x_3\, I_{Cam_{xx}} \\
&+ m_{pj}\, c_{22}\, c_{21}\, c_{11}\, F_{A_1} - c_{12}\, F_{A_1}\, I_{Cam_{xx}} - c_{22}\, F_{A_2}\, I_{Cam_{xx}}) \\
/(&- 2\, m_{pj}^2\, c_{12}\, c_{11}\, c_{21}\, c_{22} + m_{pj}^2\, c_{12}^2\, c_{21}^2 + m_{pj}\, c_{22}^2\, I_{Cam_{xx}} + m_{pj}^2\, c_{22}^2\, c_{11}^2\, I_{Cam_{yy}}\, m_{pj}\, c_{11}^2 \\
&+ I_{Cam_{yy}}\, m_{pj}\, c_{21}^2 + m_{pj}\, c_{12}^2\, I_{Cam_{xx}} + I_{Cam_{yy}}\, I_{Cam_{xx}}).
\end{aligned}
\tag{B.23}
$$

These equations can also be written in the state space matrix vector notation:

$$
\begin{aligned}
\dot{\boldsymbol{x}} &= \boldsymbol{A}\,\boldsymbol{x} + \boldsymbol{B}\,\boldsymbol{u} + \boldsymbol{z}, \\
\boldsymbol{y} &= \boldsymbol{C}\,\boldsymbol{x} + \boldsymbol{D}\,\boldsymbol{u}.
\end{aligned}
\tag{B.24}
$$

The input vector $\boldsymbol{u}$ corresponds to the forces applied to the prismatic joints and the output vector $\boldsymbol{y}$ to the camera orientation. The four system states are described with the vector $\boldsymbol{x}$. In Table B.1 the constant system parameters are introduced. They are used to determine the values of the state matrix $\boldsymbol{A}$, of the input matrix $\boldsymbol{B}$, of the output matrix $\boldsymbol{C}$, of the disturbance vector $\boldsymbol{z}$, and of the feed through matrix $\boldsymbol{D}$. For the investigated system the latter is equal to zero.

$$
\begin{aligned}
\boldsymbol{A} &= \begin{bmatrix} 0 & 0 & 1 & 0 \\ 0 & 0 & 0 & 1 \\ 0 & 0 & -133.67 & 0 \\ 0 & 11.42 & 0 & -127.22 \end{bmatrix}, \qquad \boldsymbol{B} = \begin{bmatrix} 0 & 0 \\ 0 & 0 \\ 1146.1 & -1146.1 \\ -1164.9 & -1164.9 \end{bmatrix}, \\
\boldsymbol{C} &= \begin{bmatrix} 1 & 0 & 0 & 0 \\ 0 & 1 & 0 & 0 \end{bmatrix}, \qquad \boldsymbol{z} = \begin{bmatrix} 0 & 0 & 0 & -316.18 \end{bmatrix}^T.
\end{aligned}
\tag{B.25}
$$

Table B.1.: System parameters.

Parameter	Symbol	Value
Angle approximation constant	c_{11}	13.5078 $\cdot 10^{-3}$ m/rad
Angle approximation constant	c_{12}	-12.6491 $\cdot 10^{-3}$ m/rad
Angle approximation constant	c_{21}	-13.5078 $\cdot 10^{-3}$ m/rad
Angle approximation constant	c_{11}	-12.6491 $\cdot 10^{-3}$ m/rad
Damping coefficient	d	4.317 Ns/m
Displacement CoG	x_{CoG}	0.79 $\cdot 10^{-3}$ m
Displacement CoG	z_{CoG}	15.8 $\cdot 10^{-3}$ m
Gravity	g	9.81 m/s^2
Inclination angle	ξ	0.259 rad
Inertia tensor camera	$I_{Cam_{xx}}$	6.312 $\cdot 10^{-6}$ kgm^2
Inertia tensor camera	$I_{Cam_{yy}}$	6.059 $\cdot 10^{-6}$ kgm^2
Mass camera	m_{Cam}	16 $\cdot 10^{-3}$ kg
Mass prismatic joint	m_{PJ}	15 $\cdot 10^{-3}$ kg

The matrices suggest that the camera orientation around the pan axis (angle α) is influenced by the camera velocity around this axis and by both actuator forces. The orientation around the tilt axis (angle β) is influenced by the camera velocity around this axis, by both actuator forces, by the camera orientation around the tilt axis, and by a disturbance factor. The last two parameters (angle around the tilt axis and the disturbance factor) reflect the gravity influence onto the camera orientation.

B.2. Model Validation

To determine whether the simplified dynamic model, based on a three mass system, is capable of representing the system dynamics, the model is validated. One possibility is to verify the model with measured data from the camera orientation system. However, the device allows one to only measure positions. The forces applied by the piezo–actuators can not be measured or controlled directly. Therefore, we used the formally developed *MBSim* model to verify the simplified dynamic model.
In a first step the static force to hold the camera in the neutral position (both orientation angels are zero) is determined. With the *MBSim* model the actuator forces can be determined directly to -0.13 N per each actuator. The state space representation of the three mass model (B.24) confirms that the input signal to the model are actuator forces and the output is the camera orientation. Thus, we used a closed loop control architecture to hold the camera orientation to zero. After that the position is adjusted -0.136 N must be supplied by both actuators. Thus, it can be stated that in case of a static camera orientation both models correspond very well.

In a second step the dynamic behavior of both models is compared. As mentioned before the orientation around the tilt axis depends on the actuator forces and is further influenced by the gravitational force. Therefore, we examine angle changes around the tilt axis, while the pan axis is held to zero. To cover the entire workspace we changed the camera orientation from 30 deg to -30 deg. The thereby required actuator forces are estimated with the *MBSim* model. Afterwards these forces are passed to the three mass model and with it the camera orientation is re–calculated. The estimated forces are directly passed to the model, without any closed loop control.

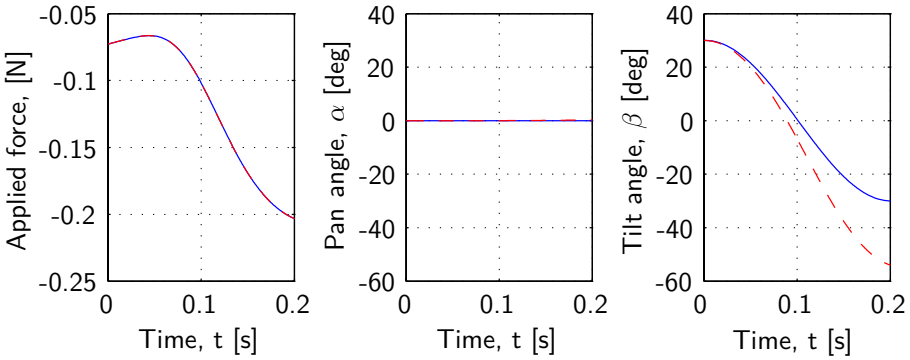

Figure B.2.: Results model validation: applied force (left); camera orientation around the pan axis (middle) and tilt axis (right), *MBSim* model [—] and three mass model [– –].

Since orientation changes are carried out only around the tilt axis and the pan orientation is held to zero, both piezo–actuators must always supply the same forces. Thus, the graphs relating to the single actuator forces are superposed and can not be distinguished in Figure B.2 (left). Figure B.2 (middle) reveals the angle around the pan axis, while on the right side of Figure B.2 the angle around the tilt axis is presented. The plots suggest that orientation changes calculated with the reduced model have a similar behavior than the input angles for the *MBSim* model. The plots indicate also that the longer the simulation time, the higher the discrepancy. These errors occur due to the high model simplifications. As mentioned before the selected control architecture is running with a sampling frequency of 1 kHz and thus, the reduced model is used to predict only a small time period of 1 ms. Afterwards the model is re–initialized (in doing so the discrepancy is set to zero) and the model is used to predict another short time period. Thus, it can be stated that the reduced dynamic model, based on a three mass system, suits the application.

B.3. Approximation of Inverse Kinematics

In Section A.1.1 an analytical inverse kinematic solution is introduced for the systems with two DoF. Due to the mechanical design of the camera orientation device

nonlinear terms occur and thus the solution can not be used for the linear state space model. Therefore we approximate these relations with two linear equations.

$$\begin{aligned}\theta_1 &= c_{11}\alpha + c_{12}\beta,\\ \theta_2 &= c_{21}\alpha + c_{22}\beta,\end{aligned} \tag{B.26}$$

where the piezo–actuator positions are denoted with θ_1 and θ_2, while the camera orientation is described with α and β. c_{11} – c_{22} are constant transformation factors. They are estimated using a least squares algorithm over the entire camera orientation device workspace. In Figure B.3 the absolute error between the real actuator positions (calculated with the inverse kinematic solution) and the approximate positions are introduced.

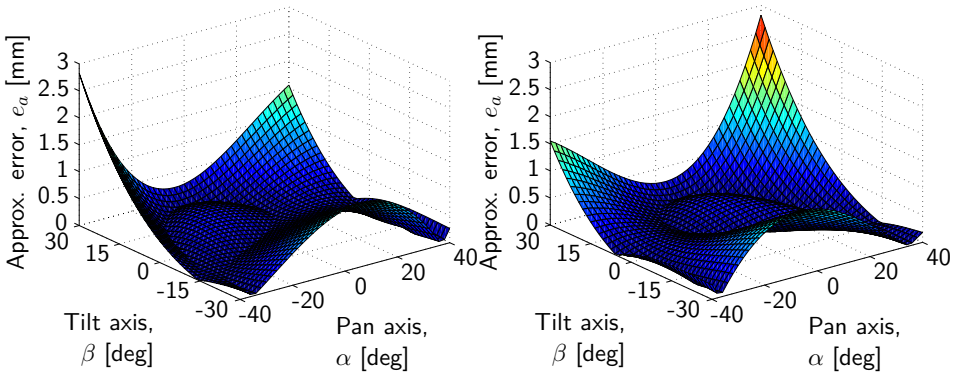

Figure B.3.: Approximation error: first actuator position θ_1 (left), second actuator position θ_2 (right).

The approximation error is maximal in the extreme workspace positions. There, errors of about 3 mm arise. Since normally users do not orient their eyes to such uncomfortable positions very long the mean error over the entire workspace is calculated to 0.36 mm for both axes. A possibility of reducing these relatively high errors is to replace the two linear equations (B.26) with piecewise linear functions. However, as reported in Section B.2 the reduced dynamic model suits the application using the linear equations.

C. Additional Results

C.1. Additional Simulation Results

While in Section 3.5 the kinematic simulation results are presented for both the mono and the stereo camera system, the outcomes of the dynamic simulation are illustrated for the mono system only. Therefore, the results concerning the stereo camera system are introduced here.

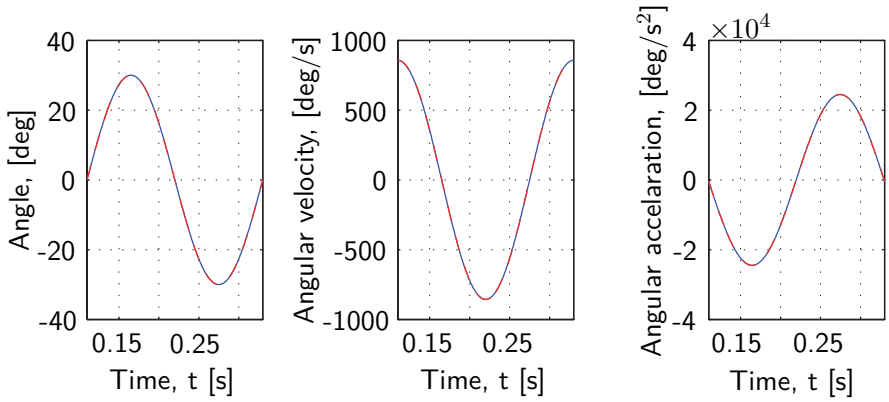

Figure C.1.: Desired angles, angle velocities, and angle accelerations around the pan [—] and the tilt axis [– –].

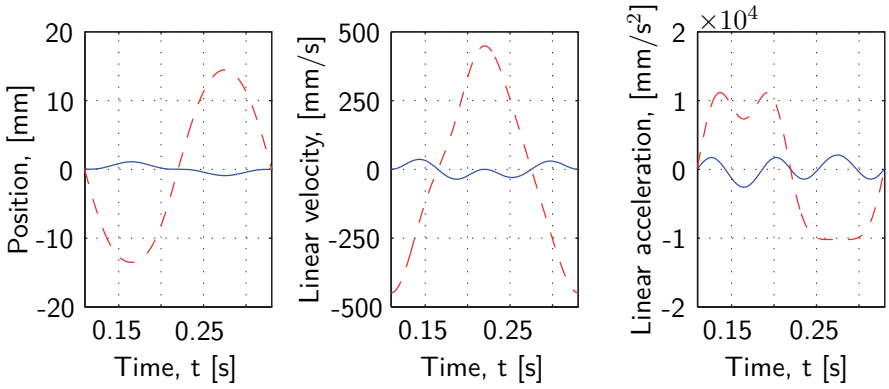

Figure C.2.: Desired positions, linear velocities, and linear accelerations of actuator one [—] and two [– –].

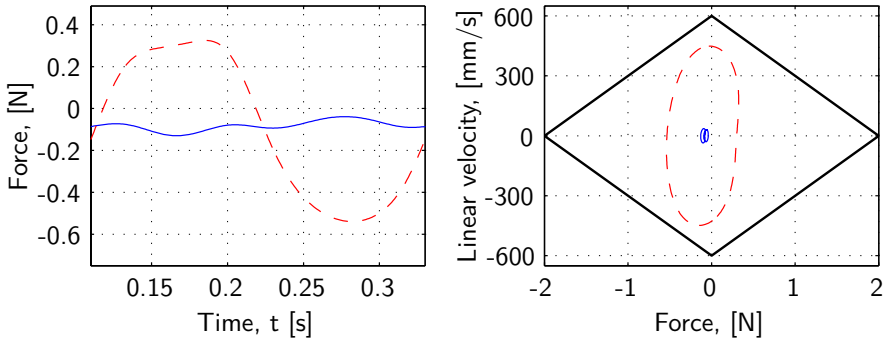

Figure C.3.: Desired forces (left), force/velocity diagram (right) of actuator one [—] and two [– –].

C.2. Additional Control Results

Section 5.2.1 reports the results obtained with the PID joint space controller with the mono camera system. The experimental results related to the stereo camera system are depicted in the following.

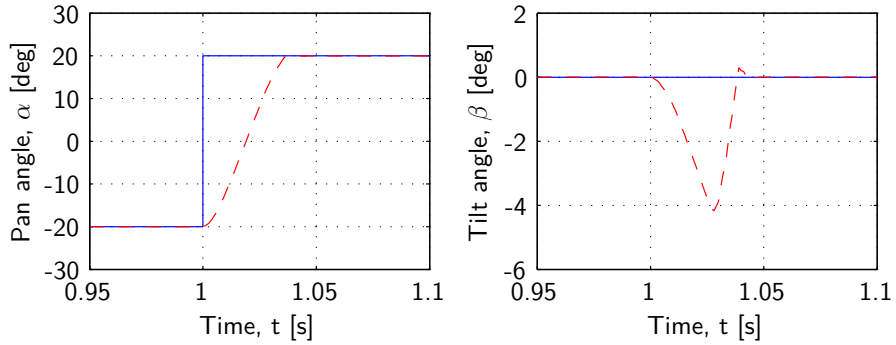

Figure C.4.: Desired [—] and measured [– –] orientation during step response, PID joint space controller, stereo camera orientation system.

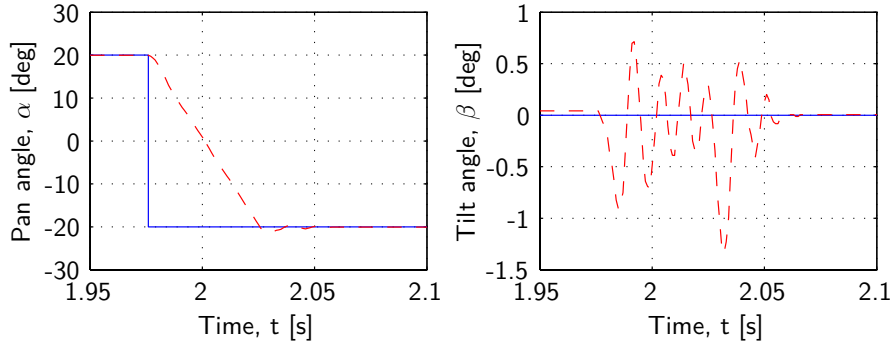

Figure C.5.: Desired [—] and measured [– –] orientation during step response, PID joint space controller, angular velocities limited to 800 deg/s, stereo camera orientation system.

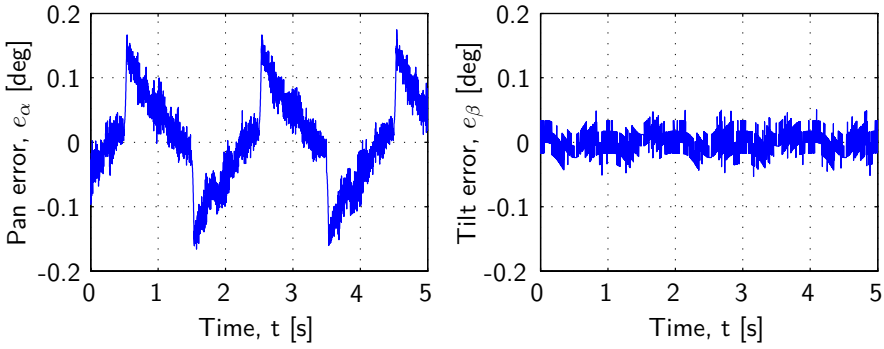

Figure C.6.: Angular error during sinusoidal movements, PID joint space controller, stereo camera orientation system.

C.3. Additional Frequency Response Results

In Section 5.4.1 only the results of the frequency response measurements for the mono camera system are introduced. In this section the results associated to the stereo camera system and to the three DoF system are indicated respectively.

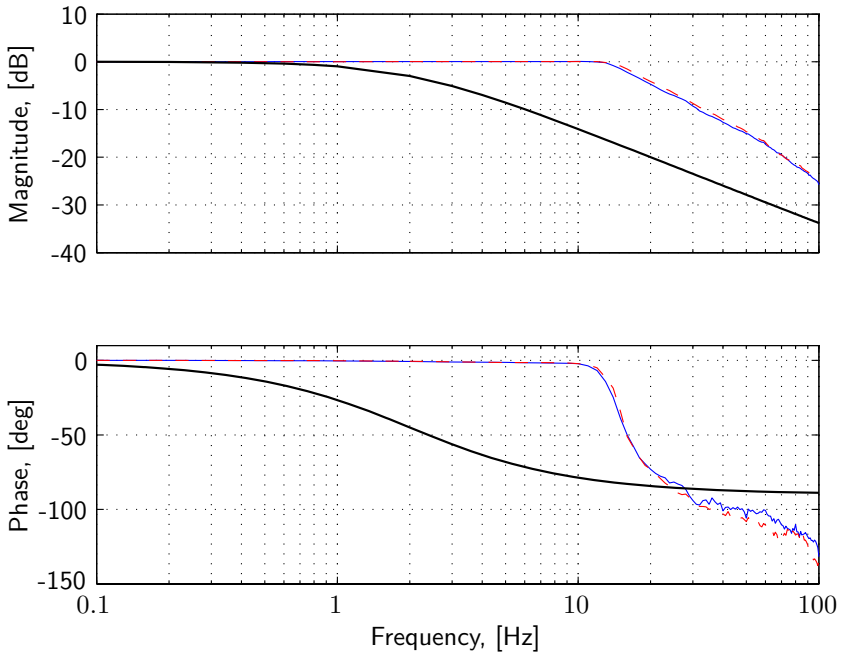

Figure C.7.: Frequency response of the stereo camera orientation system around the pan [—] and the tilt axis [– –] as well as a first–order low–pass system [—] with a cut–off frequency of 2 Hz.

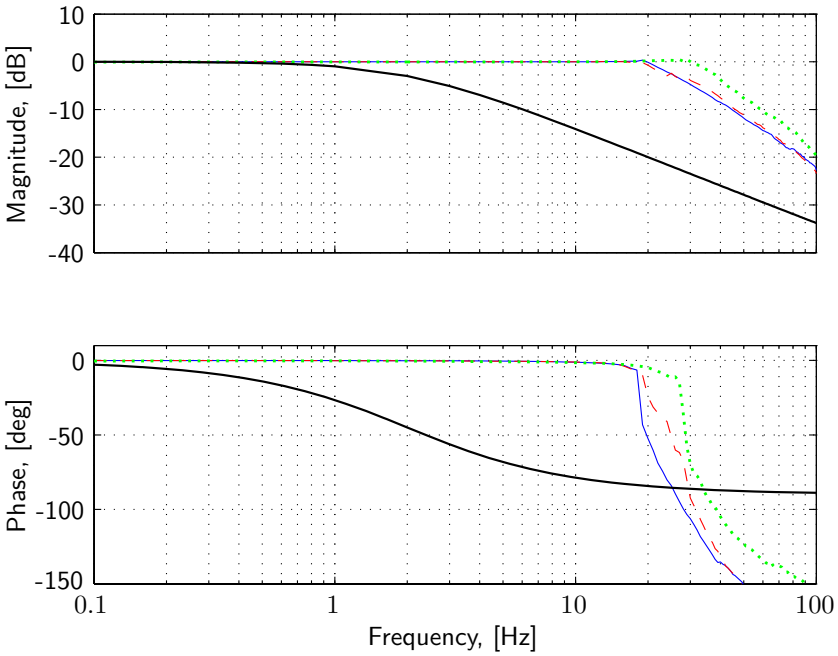

Figure C.8.: Frequency response of the three DoF camera orientation system around the pan [—], tilt [– –], and roll axis [· · ·] as well as a first–order low–pass system [**—**] with a cut–off frequency of 2 Hz.

D. Drawings

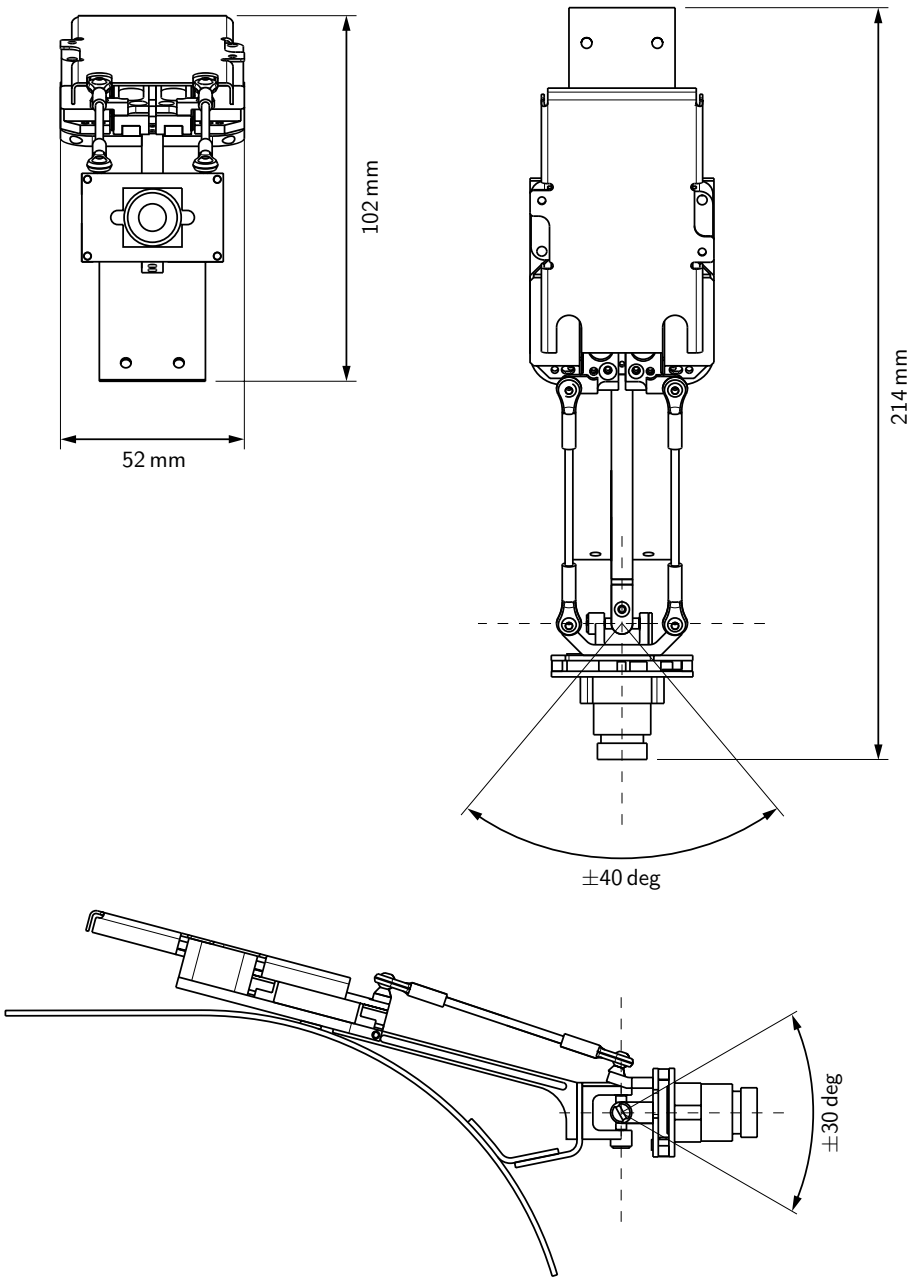

Figure D.1.: Mono camera orientation system, see Chapter 3.

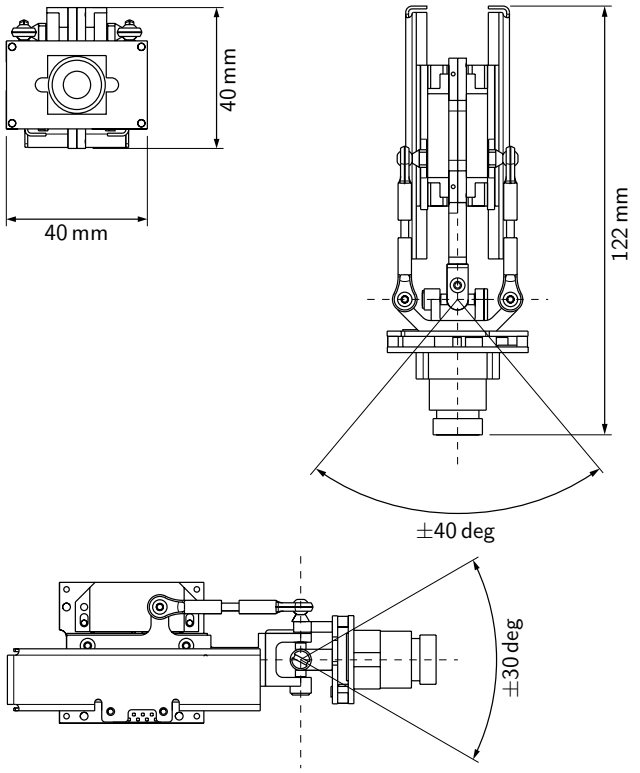

Figure D.2.: Stereo camera orientation system, see Chapter 3.

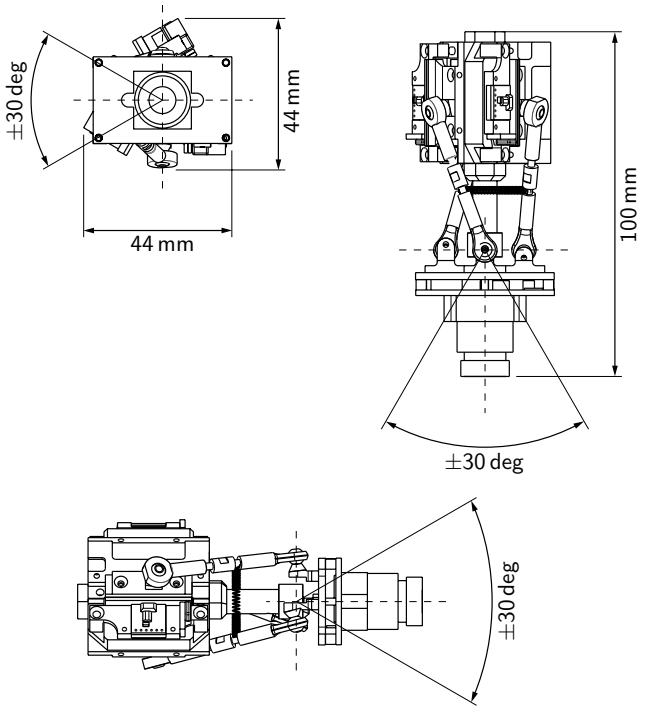

Figure D.3.: Camera orientation system with three DoF, see Chapter 4.

Bibliography

[1] Agrawal, S. K. ; Desmier, G. ; Li, S.: Fabrication and Analysis of a Novel 3 DOF Parallel Wrist Mechanism. In: *ASME Journal of Mechanical Design* 117 (1995), June, nr. 2A, pp. 343–345. – DOI 10.1115/1.2826145

[2] Andersch, P.: *Regelung einer durch lineare Piezomotoren angetriebenen Parallelkinematik*, Institute of Applied Mechanics, Technische Universität München, master thesis, 2009, in german

[3] Asfour, T. ; Welke, K. ; Azad, P. ; Ude, A. ; Dillmann, R.: The Karlsruhe Humanoid Head. In: *8th IEEE-RAS International Conference on Humanoid Robots, 2008. Humanoids 2008.* Daejeon, Korea, Dec. 2008, pp. 447–453

[4] austriamicrosystems AG: AS*5311High Resolution Magnetic Linear Encoder Data Sheet*. http://www.austriamicrosystems.com, Apr. 2010

[5] Avago Technologies: AEDR*–8400 Reflective Surface Mount Optical Encoder Data Sheet*. http://www.avagotech.com, Mar. 2010

[6] Bang, Y.-B. ; Paik, J. K. ; Shin, B.-H. ; Lee, C.: A Three-Degree-of-Freedom Anthropomorphic Oculomotor Simulator. In: *International Journal of Control Automation and Systems* 4 (2006), pp. 227–235

[7] Bar-Cohen, Y.: *Electroactive Polymer (EAP) Actuators as Artificial Muscles: Reality, Potential, and Challenges, Second Edition (SPIE Press Monograph Vol. PM136)*. 2. SPIE Publications, 2004. – ISBN 9780819452979

[8] Bassett, K. ; Hammond, M. ; Smoot, L.: A fluid-suspension, electromagnetically driven eye with video capability for animatronic applications. In: *9th IEEE-RAS International Conference on Humanoid Robots, 2009. Humanoids 2009.* Paris, France, Dec. 2009, pp. 40–46

[9] Bederson, B.B. ; Wallace, R.S. ; Schwartz, E.L.: Control and design of the spherical pointing motor. In: *Proceedings of the 1993 IEEE International Conference on Robotics and Automation, 1993.* Atlanta, GA USA, May 1993, pp. 630–636 vol.2

[10] Beetz, M. ; Buss, M. ; Wollherr, D.: Cognitive Technical Systems – What Is the Role of Artificial Intelligence? In: *Proceedings of the 30th annual German conference on Advances in Artificial Intelligence*. Osnabrück, Germany : Springer-Verlag, Sept. 2007, pp. 19–42

[11] Boldea, I. ; Nasar, S.A.: *Linear Electric Actuators and Generators*. Cambridge University Press, 2005. – ISBN 9780521020329

[12] Bosco, A. ; Bruna, A. ; Battiato, S. ; Bella, G. ; Puglisi, G.: Digital video stabilization through curve warping techniques. In: *IEEE Transactions on Consumer Electronics* 54 (2008), nr. 2, pp. 220–224. – DOI 10.1109/TCE.2008.4560078. – ISSN 0098–3063

[13] Breazeal, C. ; Scassellati, B.: How to build robots that make friends and influence people. In: *Proceedings of the IEEE/RSJ International Conference on Intelligent Robots and Systems, 1999. IROS '99.* vol. 2. Kyongju, Korea, Oct. 1999, pp. 858–863 vol.2

[14] Brunstetter, T. J. ; Mitchell, G. L. ; Fogt, N.: Magnetic field coil measurements of the accuracy of extreme gaze ocular fixation. In: *Optometry and Vision Science* 81 (2004), Aug, nr. 8, pp. 606–615. – DOI 10.1097/01.opx.0000141797.03222.72

[15] Buschmann, T. ; Lohmeier, S. ; Schwienbacher, M. ; Favot, V. ; Ulbrich, H. ; von Hundelshausen, F. ; Rohe, G. ; Wuensche, H.-J.: Walking in Unkown Environments – a Step Towards More Autonomy. In: *10th IEEE–RAS International Conference on Humanoid Robots, 2010. Humanoids 2010.* Nashville, TN, USA, Dec. 2010, pp. 1–8

[16] Cannata, G. ; Maggiali, M.: Design of a Humanoid Robot Eye. In: de Pina, F. (ed.) ; Armando, C. (ed.): *Humanoid Robots – New Developments*. Vienna, Austria : Advanced Robotic Systems International, I–Tech, 2007. – ISBN 978–3–902613–02–8, ch. 8, pp. 137–156

[17] Cannata, G. ; Maggiali, M.: Models for the Design of Bioinspired Robot Eyes. In: *IEEE Transactions on Robotics* 24 (2008), Feb., nr. 1, pp. 27–44. – DOI 10.1109/TRO.2007.906270. – ISSN 1552–3098

[18] Cárdenas Miranda, A.: *Konzeption eines kompakten 3-DOF Kameraorientierungssystems*, Institute of Applied Mechanics, Technische Universität München, Semester thesis, Apr. 2008, in german

[19] Carpenter, R. H. S.: *Movements of the Eyes*. 2. London : Pion Ltd, 1998. – 593 S. – ISBN 9780850861099

[20] Clarke, A.H. ; Haslwanter, T.: The orientation of Listing's Plane in microgravity. In: *Journal of Vision Research* 47 (2007), Nov, nr. 25, pp. 3132–3140. – DOI 10.1016/j.visres.2007.09.001

[21] Classen, M. ; Tytgat, G.N.J. ; Lightdale, C.J.: *Gastroenterological Endoscopy*. 2. Thieme Medical Publishers, 2010. – ISBN 3131258527

[22] Colestock, H.: *Industrial Robotics*. 1. McGraw-Hill/TAB Electronics, 2005. – 212 S. – ISBN 9780071440523

[23] Daerden, F. ; Lefeber, D.: Pneumatic artificial muscles: actuators for robotics and automation. In: *European Journal of Mechanical and Environmental Engineering* 47 (2002), nr. 1, pp. 10–21

[24] Dankers, A. ; Zelinsky, A.: CeDAR: A real-world vision system: Mechanism, control and visual processing. In: *Machine Vision and Applications* 16 (2004), nr. 1, 47–58. http://www.springerlink.com/index/10.1007/s00138-004-0156-3

[25] Delgado Londono, S.: *Berechnung der Vorwärtslösung für eine 2 DoF Parallel–Kinmematik*, Institute of Applied Mechanics, Technische Universität München, Semester thesis, Okt. 2008, in german

[26] Dera, T. ; Boning, G. ; Bardins, S. ; Schneider, E.: Low-latency video tracking of horizontal, vertical, and torsional eye movements as a basis for 3dof realtime motion control of a head-mounted camera. In: *IEEE International Conference on Systems, Man and Cybernetics, 2006. SMC '06* vol. 6. Taipei, Taiwan, Oct. 2006, pp. 5191–5196

[27] Dickmanns, E.D.: An advanced vision system for ground vehicles. In: *First International Workshop on In–Vehicle Cognitive Computer Vision Systems (IVCCVS)*. Graz, Austria, Apr 2003, pp. 1–12

[28] Dodge, R.: Visual perception during eye movement. In: *Psychological Review* 7 (1900), nr. 5, pp. 454–465

[29] Duchowski, A.: *Eye Tracking Methodology: Theory and Practice*. 2. Springer, 2007. – ISBN 9781846286087

[30] Duerig, T.W. ; Melton, K.N. ; Stöckel, D. ; Wayman, C.M.: *Engineering Aspects of Shape Memory Alloys*. Butterworth-Heinemann, 1990. – ISBN 9780408040655

[31] EDO Ceramics: *High Speed Piezoelectric Micropositioning Motor Model PDA130 Data Sheet*. http://edocorp.com, Feb. 2002

[32] Eggert, T.: Eye movement recordings: methods. In: *Dev Ophthalmol* 40 (2007), pp. 15–34. – DOI 10.1159/0000100347

[33] Elliptec AG: *X15G Data Sheet*. http://www.elliptec.com, Apr. 2008

[34] Encoder Technology LLC: *LM 720CPI Data Sheet*. http://www.encodertech.com, Oct. 2006

[35] Enright, J.T.: Ocular translation and cyclotorsion due to changes in fixation distance. In: *Journal of Vision Research* 20 (1980), nr. 7, pp. 595–601. – DOI 10.1016/0042–6989(80)90116–9. – ISSN 0042–6989

[36] Falb, P. ; Wolovich, W.: Decoupling in the design and synthesis of multivariable control systems. In: *IEEE Transactions on Automatic Control* 12 (1967), nr. 6, pp. 651–659. – ISSN 0018–9286

[37] Faraz, A. ; Payandeh, S.: Towards approximate models of Coulomb frictional moments in: (I) revolute pin joints and (II) spherical-socket ball joints. In: *Journal of Engineering Mathematics* 40 (2001), pp. 283–296(14)

[38] Föllinger, O.: *Regelungstechnik. Einführung in die Methoden und ihre Anwendung*. 8. Hüthig, 1994, in german. – ISBN 9783778523360

[39] Förg, M.: *Mehrkörpersysteme mit mengenwertigen Kraftgesetzen – Theorie und Numerik*, Technische Universität München, VDI Fortschritt-Berichte, Reihe 20, Nr. 411, 2007, in german

[40] Furman, J.M. ; Schor, R.H.: Orientation of Listing's plane during static tilt in young and older human subjects. In: *Journal of Vision Research* 43 (2003), nr. 1, pp. 67–76. – DOI 10.1016/S0042–6989(02)00385–1. – ISSN 0042–6989

[41] Gilmore, P. ; Kelley, C.T.: An Implicit Filtering Algorithm For Optimization Of Functions With Many Local Minima. In: *Journal of Optimisation (SIAM)* 5 (1995), pp. 269–285

[42] Glasauer, S.: Current models of the ocular motor system. In: *Developments in ophthalmology* 40 (2007), pp. 158–174. – ISSN 0250–3751

[43] Godkin, M.: Closed–Ended Linear Voice Coil Actuator with Improved Force Characteristic. In: *9th International Conference on New Actuators, Actuator 2004*. Bremen, Germany, Jun 2004, pp. 677–680

[44] Gosselin, C.M. ; Hamel, J.-F.: The agile eye: a high-performance three-degree-of-freedom camera-orienting device. In: *Proc. IEEE International Conference on Robotics and Automation, 1994.*, 1994, 781–786 vol.1

[45] Gu, J. ; Meng, M. ; Cook, A. ; Faulkner, M. G.: A study on natural movement of artificial eye implant. In: *Robotics and Autonomous Systems* 32 (2000), nr. 2-3, pp. 153 – 161. – DOI 10.1016/S0921–8890(99)00116–5. – ISSN 0921–8890

[46] Guenter, F. ; Roos, L. ; Guignard, A. ; Billard, A.G.: Design of a biomimetic upper body for the humanoid robot Robota. In: *5th IEEE-RAS International Conference on Humanoid Robots, 2005. Humanoids 2005,.* Tsukuba, Japan, Dec. 2005, pp. 56–61

[47] Guitton, D. ; Volle, M.: Gaze control in humans: eye-head coordination during orienting movements to targets within and beyond the oculomotor range. In: *J Neurophysiol* 58 (1987), nr. 3, 427-459. `http://jn.physiology.org/cgi/content/abstract/58/3/427`

[48] Hamrock, B.J. ; Jacobson, B. ; Schmid, S.R.: *Fundamentals of Machine Elements*. 2. McGraw–Hill, New York, 2005. – 928 S. – ISBN 9780072976823

[49] Haslwanter, T.: Mathematics of three–dimensional eye rotations. In: *Journal of Vision Research* 35 (1995), nr. 12, pp. 1727–1739. – DOI 10.1016/0042–6989(94)00257–M. – ISSN 0042–6989

[50] Hemsel, T. ; Mracek, M. ; Twiefel, J. ; Vasiljev, P.: Piezoelectric linear motor concepts based on coupling of longitudinal vibrations. In: *Ultrasonics* 44 (2006), nr. Supplement 1, pp. e591–e596. – DOI 10.1016/j.ultras.2006.05.056. – ISSN 0041–624X. – Proceedings of Ultrasonics International (UI'05) and World Congress on Ultrasonics (WCU)

[51] Honeywell Inc.: *Solid State Sensors, Digital Magnetoresistive Sensors, 2SS52M Series Data Sheet*. www.honeywell.com/sensing, Mar. 2010

[52] Hoshina, M. ; Mashimo, T. ; Toyama, S.: Development of spherical ultrasonic motor as a camera actuator for pipe inspection robot. In: *IEEE/RSJ International Conference on Intelligent Robots and Systems, 2009. IROS 2009.* St. Louis, MO, USA, Oct. 2009, pp. 2379–2384

[53] Jin, HZ. ; Lu, H. ; Cho, SK. ; Lee, JM.: Nonlinear Compensation of a New Noncontact Joystick Using the Universal Joint Mechanism. In: *IEEE/ASME Transactions on Mechatronics* 12 (2007), nr. 5, pp. 549–556. – ISSN 1083–4435

[54] Kandel, E.R. ; Schwartz, J.H. ; Jessell, T.M.: *Essentials of Neural Science and Behavior*. 1. McGraw–Hill/Appleton & Lange, 1996. – ISBN 9780838522455

[55] Kelley, J. F.: An empirical methodology for writing user–friendly natural language computer applications. In: *Proceedings of the SIGCHI conference on Human Factors in Computing Systems, CHI '83*. New York, NY, USA : ACM, Jan. 1983. – ISBN 0–89791–121–0, pp. 193–196

[56] Kurata, T. ; Sakata, N. ; Kourogi, M. ; Kuzuoka, H. ; Billinghurst, M.: Remote collaboration using a shoulder-worn active camera/laser. In: *Eighth IEEE International Symposium on Wearable Computers, 2004. ISWC 2004.* vol. 1. Arlington, VA, USA, 2004. – ISSN 1530–0811, pp. 62–69

[57] Land, M. F.: Eye movements and the control of actions in everyday life. In: *Progress in Retinal and Eye Research* 25 (2006), May, nr. 3, pp. 296–324. – DOI 10.1016/j.preteyeres.2006.01.002. – ISSN 1350–9462

[58] Lee, D.V. ; Velinsky, S.A.: Analysis and Experimental Verification of a Three-Dimensional Noncontacting Angular Motion Sensor. In: *IEEE/ASME Transactions on Mechatronics* 12 (2007), nr. 6, pp. 612–622. – DOI 10.1109/TMECH.2007.910057. – ISSN 1083–4435

[59] Lee, K.-M. ; Zhou, D.: A real-time optical sensor for simultaneous measurement of three–DOF motions. In: *IEEE/ASME Transactions on Mechatronics* 9 (2004), nr. 3, pp. 499–507. – ISSN 1083–4435

[60] Leigh, J. R. ; Zee, D. S.: *Contemporary neurology series*. vol. 70: *The neurology of eye movements*. 4. Oxford University Press, Inc. New York, 2006. – 776 S. – ISBN 9780195300901

[61] Lenz, A. ; Anderson, S.R. ; Pipe, A.G. ; Melhuish, C. ; Dean, P. ; Porrill, J.: Cerebellar–Inspired Adaptive Control of a Robot Eye Actuated by Pneumatic Artificial Muscles. In: *IEEE Transactions on Systems, Man, and Cybernetics, Part B: Cybernetics,* 39 (2009), nr. 6, pp. 1420–1433. – DOI 10.1109/TSMCB.2009.2018138. – ISSN 1083–4419

[62] Liversedge, S. P. ; Findlay, J. M.: Saccadic eye movements and cognition. In: *Trends in Cognitive Sciences* 4 (2000), Jan., nr. 1, pp. 6–14. – DOI 10.1016/S1364–6613(99)01418–7.

[63] Lohmann, B.: Vollständige und teilweise Führungsentkopplung dynamischer Systeme durch konstante Zustandszurückführung. In: *at–Automatisierungstechnik* 39 (1991), pp. 329–334 and 376–378, in german

[64] Lohmeier, S. ; Buschmann, T. ; Ulbrich, H.: System Design and Control of Anthropomorphic Walking Robot *LOLA*. In: *IEEE/ASME Transactions on Mechatronics* 14 (2009), nr. 6, pp. 658–666. – DOI 10.1109/TMECH.2009.2032079. – ISSN 1083–4435

[65] Lowe, D.G.: Object recognition from local scale–invariant features. In: *The Proceedings of the Seventh IEEE International Conference on Computer Vision* vol. 2, 1999, pp. 1150–1157

[66] Lucas, B.D. ; Kanade, T.: An Iterative Image Registration Technique with an Application to Stereo Vision (DARPA). In: *Proceedings of the 1981 DARPA Image Understanding Workshop*, 1981, pp. 121–130

[67] Lynch, P.J.: *Medical Illustrations*. http://patricklynch.net, Apr. 2010. – Creative Commons Attribution 2.5 License 2006; Creative Credits: Patrick J. Lynch, medical illustrator; C. Carl Jaffe, MD, cardiologist

[68] Manusov, Valerie ; Patterson, Miles L.: *The SAGE Handbook of Nonverbal Communication*. 1. Sage Publications, Inc, 2006. – ISBN 9781412904049

[69] Mayol, W. W. ; Tordoff, B. J. ; Murray, D. W.: Wearable visual robots. In: *Proc. Fourth International Symposium on Wearable Computers*, 2000, pp. 95–102

[70] Mayol, W. W. ; Tordoff, B. J. ; Murray, D. W.: Designing a miniature wearable visual robot. In: *Proc. IEEE International Conference on Robotics and Automation ICRA '02* vol. 4, 2002, pp. 3725–3730

[71] Mayol-Cuevas, W.W. ; Tordoff, B.J. ; Murray, D.W.: On the Choice and Placement of Wearable Vision Sensors. In: *IEEE Transactions on Systems, Man and Cybernetics, Part A: Systems and Humans* 39 (2009), nr. 2, pp. 414–425. – ISSN 1083–4427

[72] Merlet, J.P. ; Gladwell, G.M.L. (ed.): *Solid Mechanics and Its Applications*. vol. 74: *Parallel Robots*. Kluwer Academic Publishers, 2000. – 384 S. – ISBN 9780792363088

[73] Murray, D.W. ; Du, F. ; McLauchlan, P. F. ; Reid, I.D. ; Sharkey, P.M. ; Brady, M.: Design of Stereo Heads. In: Blake, A. (ed.) ; Yuille, A.L. (ed.): *Active Vision*, MIT Press, 1992, 155–172

[74] Nanomotion Ltd.: *ST Motor Data Sheet*. http://www.nanomotion.com, Mar. 2010

[75] Numeric Jena GmbH: *Encoder Kit L4 Data Sheet*. http://www.numerikjena.de, Mar. 2010

[76] Pan, Z. ; Ngo, C.-W.: Selective object stabilization for home video consumers. In: *IEEE Transactions on Consumer Electronics* 51 (2005), Nov., nr. 4, pp. 1074–1084. – DOI 10.1109/TCE.2005.1561827. – ISSN 0098–3063

[77] Park, K.R.: Gaze Detection System by Wide and Auto Pan/Tilt Narrow View Camera. In: Michaelis, B. (ed.) ; Krell, G. (ed.): *DAGM–Symposium* vol. 2781, Springer, 2003 (Lecture Notes in Computer Science), 76–83. – Pattern Recognition, 25th DAGM Symposium, Magdeburg, Germany, September 10–12, 2003, Proceedings

[78] Paynter, H.M. ; Juarez, Jr. J.M.: Thermodynamic analysis of a mechatronic pneumatically driven spherical joint. In: *IEEE/ASME Transactions on Mechatronics,* 5 (2000), nr. 2, pp. 153–157. – DOI 10.1109/3516.847088. – ISSN 1083–4435

[79] Pfeiffer, F. ; Löffler, K. ; Gienger, M. ; Ulbrich, H.: Sensor and Control Aspects of Biped Robot 'Johnnie'. In: *Int. J. Humanoid Robot.* 1 (2004), nr. 3, pp. 481–96. – DOI 10.1142/S0219843604000228

[80] Physik Instrumente (PI) GmbH & Co. KG: *MS 144E User Manual, C–180 Pulse–Mode OEM Drive Electronics for PILine®P–661Piezo Linear Motors*. 1.0.0, June. 2005

[81] Physik Instrumente (PI) GmbH & Co. KG: *MP 76E User Manual, P–661, PILine®OEM Piezo Linear Motors*. 1.0.0, Feb. 2006

[82] Physik Instrumente (PI) GmbH & Co. KG: *MP 76E User Manual, P–661/P–664, PILine®OEM Piezo Linear Motors*. 1.1.1, May 2007

[83] Physik Instrumente (PI) GmbH & Co. KG: *MS 143E User Manual, C–184 PILine®Analog OEM Drive Electronics*. 1.1.1, Oct. 2007

[84] Pinckney, N.: Pulse-width modulation for microcontroller servo control. In: *IEEE Potentials.* 25 (2006), nr. 1, pp. 27–29. – ISSN 0278–6648

[85] Point Grey Research Inc.: *Dragonfly 2 Data Sheet*. http://www.ptgrey.com, Sept. 2009

[86] Point Grey Research Inc.: *Firefly MV Data Sheet*. http://www.ptgrey.com, Sept. 2009

[87] Polpitiya, A. D. ; Dayawansa, W. P. ; Martin, C. F. ; Ghosh, B. K.: Geometry and Control of Human Eye Movements. In: *IEEE Transactions on Automatic Control* 52 (2007), nr. 2, pp. 170–180. – DOI 10.1109/TAC.2006.887902. – ISSN 0018–9286

[88] Ragulskis, K. ; Bansevičius, R. ; Barauskas, R. ; Kulvietis, G.: *Vibromotors For Precision Microrobots (Applications of Vibration Series)*. 1. Taylor & Francis, 1988. – ISBN 9780891165491

[89] Riebe, S. ; Ulbrich, H.: Modelling and online computation of the dynamics of a parallel kinematic with six degrees-of-freedom. In: *Archive of Applied Mechanics (Ingenieur Archiv)* 72 (2003), Jun, nr. 11, pp. 817–829. – DOI 10.1007/s00419–002–0262–5

[90] Ryu, Y.G. ; Roh, H.C. ; Kim, S.J. ; An, K.H. ; Chung, M.J.: Digital Image Stabilization for humanoid eyes inspired by human VOR system. In: *IEEE International Conference on Robotics and Biomimetics (ROBIO 2009)*, 2009, pp. 2301–2306

[91] Sapporo Precision Bearing Inc.: *High Precision Minature Bearings*, 2008. – Cat.No.908-2004-3

[92] Sashida, T. ; Kenjo, T.: *An Introduction to Ultrasonic Motors (Monographs in Electrical and Electronic Engineering)*. Oxford University Press, USA, 1994. – ISBN 9780198563952

[93] Schneider, E. ; Dera, T. ; Bard, K. ; Bardins, S. ; Boening, G. ; Brand, T.: Eye movement driven head-mounted camera: it looks where the eyes look. In: *IEEE International Conference on Systems, Man and Cybernetics, 2005* vol. 3, 2005, pp. 2437–2442 Vol. 3

[94] Schneider, E. ; Kohlbecher, S. ; Bartl, K. ; Wallhoff, F. ; Brandt, T.: Experimental platform for Wizard–of–Oz evaluations of biomimetic active vision in robots. In: *IEEE International Conference on Robotics and Biomimetics (ROBIO 2009)*, 2009, pp. 1484–1489

[95] Schröder, D.: *Elektrische Antriebe – Regelung von Antriebssystemen*. 2. Springer Verlag Berlin Heidelberg New York, 2001, in german. – ISBN 3–540–41994–2

[96] Schrüfer, E.: *Elektrische Meßtechnik. Messung elektrischer und nichtelektrischer Größen.* Fachbuchverlag Leipzig, 2003, in german. – ISBN 9783446218093

[97] Sciavicco, L. ; Siciliano, B.: *Modelling and Control of Robot Manipulators*. 2. Springer-Verlag New York, Inc., 2000. – 378 S. – ISBN 9781852332211

[98] Sensitec GmbH: *ELS29–nl–SST03–01 Incremental Sensor Module Data Sheet*. http://www.sensitec.com, Jan. 2009

[99] Shimizu, S.: Wide–Angle Foveation for All–Purpose Use. In: *IEEE/ASME Transactions on Mechatronics,* 13 (2008), nr. 5, pp. 587–597. – ISSN 1083–4435

[100] Siciliano, B. ; Khatib, O.: *Springer Handbook of Robotics*. 1. Springer, 2008. – ISBN 9783540239574

[101] Sosnowski, S. ; Bittermann, A. ; Kuhnlenz, K. ; Buss, M.: Design and Evaluation of Emotion–Display EDDIE. In: *Proceedings of the IEEE/RSJ International Conference on Intelligent Robots and Systems, 2006. IROS 2006.* Beijing, China, Oct. 2006, pp. 3113 –3118

[102] Stein, D. ; Scheinerman, E.R. ; Chirikjian, G.S.: Mathematical models of binary spherical–motion encoders. In: *IEEE/ASME Transactions on Mechatronics* 8 (2003), nr. 2, pp. 234–244. – DOI 10.1109/TMECH.2003.812824. – ISSN 1083–4435

[103] Straumann, D. ; Zee, D.S. ; Solomon, D. ; Kramer, P.D.: Validity of Listing's law during fixations, saccades, smooth pursuit eye movements, and blinks. In: *Journal of Experimental Brain Research* 112 (1996), Nov, nr. 1, pp. 135–146. – DOI 10.1007/BF00227187

[104] Szeliski, R.: *Image Alignment and Stitching: A Tutorial*. Technical Report: MSR–TR–2004–92, 2004

[105] 't Hart, M. B. ; Vockeroth, J. ; Schumann, F. ; Bartl, K. ; Schneider, E. ; König, P. ; Einhäuser, W.: Gaze allocation in natural stimuli: Comparing free exploration to head–fixed viewing conditions. In: *Journal of Visual Cognition* 17 (2009), nr. 6, pp. 1132–1158. – DOI 10.1080/13506280902812304

[106] Takemura, K. ; Ohno, Y. ; Maeno, T.: Design of a plate type multi-DOF ultrasonic motor and its self-oscillation driving circuit. In: *IEEE/ASME Transactions on Mechatronics* 9 (2004), nr. 3, pp. 474–480. – ISSN 1083–4435

[107] Tsujita, T. ; Konno, A. ; Uchiyama, M.: Design and Development of a High Speed Binocular Camera Head. In: *Proceedings of the 2005 IEEE International Conference on Robotics and Automation 2005, ICRA 2005.*, 2005, pp. 785–792

[108] Ulbrich, H.: *Maschinendynamik*. Teubner–Verlag, 1996, in german (Teubner Studienbücher Mechanik). – ISBN 9783519032335

[109] US Digital: EM*1 Transmissive Optical Encoder Module Data Sheet*. http://www.usdigital.com, Apr. 2010

[110] Vernon, D. ; Metta, G. ; Sandini, G.: A Survey of Artificial Cognitive Systems: Implications for the Autonomous Development of Mental Capabilities in Computational Agents. In: *IEEE Transactions on Evolutionary Computation* 11 (2007), nr. 2, pp. 151–180. – DOI 10.1109/TEVC.2006.890274. – ISSN 1089–778X

[111] Vockeroth, J. ; Dera, T. ; Boening, G. ; Bartl, K. ; Bardins, S. ; Schneider, E.: The combination of a mobile gaze-driven and a head-mounted camera in a Hybrid perspective setup. In: *IEEE International Conference on*

Proc. ISIC Systems, Man and Cybernetics. Montréal, USA, 7–10 Oct. 2007, pp. 2576–2581

[112] von Helmholtz, H.: *Handbuch der physiologischen Optik. Allgeneine Encyklopädie der Physik, IX. Band.* Voss, L., 1867, in german

[113] Wagner, P. ; Bartl, B. ; Günthner, W. ; Schneider, E. ; Brandt, T. ; Ulbrich, H.: A pivotable head mounted camera system that is aligned by three-dimensional eye movements. In: *ETRA '06: Proceedings of the 2006 symposium on Eye tracking research & applications*. New York, NY, USA : ACM Press, 2006, pp. 117–124

[114] Wagner, P. ; Günthner, W. ; Ulbrich, H.: Design and Implementation of a Parallel Three-Degree-of-Freedom Camera Motion Device. In: *Proceedings of Joint Conference of the 37th International Symposium on Robotics ISR 2006 and the German Conference on Robotics*. Munich, Germany, May 2006, pp. 1–12

[115] Wagner, P. ; Günthner, W. ; Ulbrich, H.: Gaze Control Devices for Driver Assistance Systems. In: *Proceedings of The 8th International Conference on Motion and Vibration Control MOVIC*. Daejeon, Korea, Aug 2006, pp. 658–663

[116] Waldron, K.J. ; Kinzel, G.L.: *Kinematics, Dynamics, and Design of Machinery*. 2. John Wiley & Sons, Inc., 2003. – 680 S. – ISBN 9780471244172

[117] Wang, X. ; Zhang, Y. ; Fu, X. ; Xiang, G.: Design and Kinematic Analysis of a Novel Humanoid Robot Eye Using Pneumatic Artificial Muscles. In: *Journal of Bionic Engineering* 5 (2008), nr. 3, pp. 264 – 270. – DOI 10.1016/S1672–6529(08)60034–7. – ISSN 1672–6529

[118] Wischneswskiy, W. ; Kovalev, S. ; Vyshnevskyy, O.: New Ultrasonic Piezoelectric Actuator for Nanopositioning. In: *9th International Conference on New Actuators, Actuator 2004*. Bremen, Germany, Jun 2004, pp. 118–122

[119] Wolfe (née Bunton), T.B. ; Faulkner, M. G. ; Wolfaardt, J.: Development of a shape memory alloy actuator for a robotic eye prosthesis. In: *Smart Materials and Structures* 14 (2005), nr. 4, pp. 759–768. – DOI 10.1088/0964–1726/14/4/035

[120] Yan, L. ; Chen, I.-M. ; Lim, C.K. ; Yang, G. ; Lin, W. ; Lee, K.-M.: Design and Analysis of a Permanent Magnet Spherical Actuator. In: *IEEE/ASME Transactions on Mechatronics* 13 (2008), nr. 2, pp. 239–248. – ISSN 1083–4435

Own related Publications

[121] Schneider, E. ; Kohlbecher, S. ; Villgrattner, T. ; Bartl, K. ; Bardins, S. ; Poitschke, T. ; Ulbrich, H. ; Brandt, T.: Vision system for wearable and robotic uses. In: *The 17th IEEE International Symposium on*

Robot and Human Interactive Communication, 2008. RO-MAN 2008., 2008, pp. 53–58

[122] Schneider, E. ; Villgrattner, T. ; Vockeroth, J. ; Bartl, K. ; Kohlbecher, S. ; Bardins, S. ; Ulbrich, H. ; Brandt, T.: EyeSeeCam: An Eye Movement-Driven Head Camera for the Examination of Natural Visual Exploration. In: *Annals of the New York Academy of Sciences* 1164 (2009), nr. Basic and Clinical Aspects of Vertigo and Dizziness, pp. 461–467. – DOI 10.1111/j.1749–6632.2009.03858.x

[123] Schneider, E. ; Vockeroth, J. ; Bartl, K. ; Dera, T. ; Bardins, S. ; Villgrattner, T. ; Brandt, T.: Blickgesteuerte Kopfkamera zur Video-Dokumentation offener chirurgischer Eingriffe mit hybrider Anzeige von Blick- und kopffestem Szenenfilm. In: *AUTOMED*. Munich, Germany, Oct. 2007, in german

[124] Villgrattner, T. ; Schneider, E. ; Andersch, P. ; Ulbrich, H.: Compact High Dynamic 3 DoF Camera Orientation System: Development and Control. In: *Proceedings of The 10th International Conference on Motion and Vibration Control (MOVIC 2010)*. Tokyo, Japan, Aug. 2010, pp. 1–10

[125] Villgrattner, T. ; Thümmel, T. ; Ulbrich, H.: Light-Weight High Dynamic Camera Orientation System. In: Kecskeméthy, A. (ed.) ; Müller, A. (ed.): *Proceedings of the 5th International Workshop on Computational Kinematics*. Springer, Jun. 2009, pp. 307–314

[126] Villgrattner, T. ; Ulbrich, H.: Control of a Piezo-Actuated Pan / Tilt Camera Motion Device. In: *11th International Conference on New Actuators, Actuator 2008*. Bremen, Germany, Jun. 2008, pp. 129–132

[127] Villgrattner, T. ; Ulbrich, H.: Piezo-Driven Two-Degree-of-Freedom Camera Orientation System. In: *IEEE International Conference on Industrial Technology, ICIT 2008*. Chengdu, China, Apr. 2008, pp. 1–6

[128] Villgrattner, T. ; Ulbrich, H.: Hochdynamisches kompaktes paralleles Kameraorientierungssystem. In: *Robotik 2008, VDI-Berichte 2012, ISBN 978-3-18-092012-2*. Munich, Germany, Jun. 2008, in german, pp. 55–58

[129] Villgrattner, T. ; Ulbrich, H.: Design and Control of a Compact High-Dynamic Camera-Orientation System. In: *IEEE/ASME Transactions on Mechatronics* in press (2010), nr. 99, pp. 1–11. – DOI 10.1109/TMECH.2009.2039223. – ISSN 1083–4435

[130] Villgrattner, T. ; Ulbrich, H.: Optimization and Dynamic Simulation of a Parallel Three Degree-of-Freedom Camera Orientation System. In: *IEEE/RSJ International Conference on Intelligent Robots and Systems (IROS), 2010*. Taipei, Taiwan, Oct. 2010. – ISSN 2153–0858, pp. 2829–2836

[131] Villgrattner, T. ; Zander, R. ; Ulbrich, H.: Modeling and simulation of a piezo-driven camera orientation system. In: *IEEE International Conference on Mechatronics, 2009. ICM 2009.* Málaga, Spain, Apr. 2009, pp. 1–6